Order 2015-ISAL-0075 Year 2015

PhD. THESIS

Damage mechanisms in silicon nitride materials under contact loading

Presented at
l'Institut National des Sciences Appliquées de Lyon

to obtain
the TITLE OF DOCTOR

Doctoral formation
MATÉRIAUX DE LYON

Speciality :
Matériaux

by

Nacer AZEGGAGH

Defended on september 10^{th} 2015 on examination Commision

Jury

Pr Koshi ADACHI	Tohoku University	President
Pr Rouxel TANGUY	Rennes 1 University	Reviewer
Pr Tatsuya KAWADA	Tohoku University	Reviewer
Pr Jérôme CHEVALIER	INSA LYON	Supervisor
Pr Daniel NÉLIAS	INSA LYON	Co-supervisor
Pr Toshiyuki HASHIDA	Tohoku University	Co-supervisor
Dr Lucile JOLY-POTTUZ	INSA LYON	Co-supervisor
Mr Bruno DRUEZ	SNECMA	Invited

LaMCoS - MATEIS - INSA de Lyon
20, avenue Albert Einstein, 69621 Villeurbanne Cedex (FRANCE)

INSA Direction de la Recherche - Ecoles Doctorales – Quinquennal 2011-2015

SIGLE	ECOLE DOCTORALE	NOM ET COORDONNEES DU RESPONSABLE
CHIMIE	**CHIMIE DE LYON** **http://www.edchimie-lyon.fr** Insa : R. GOURDON	M. Jean Marc LANCELIN Université de Lyon – Collège Doctoral Bât ESCPE 43 bd du 11 novembre 1918 69622 VILLEURBANNE Cedex Tél : 04.72.43 13 95 directeur@edchimie-lyon.fr
E.E.A.	**ELECTRONIQUE, ELECTROTECHNIQUE, AUTOMATIQUE** **http://edeea.ec-lyon.fr** Secrétariat : M.C. HAVGOUDOUKIAN eea@ec-lyon.fr	M. Gérard SCORLETTI Ecole Centrale de Lyon 36 avenue Guy de Collongue 69134 ECULLY Tél : 04.72.18 65 55 Fax : 04 78 43 37 17 Gerard.scorletti@ec-lyon.fr
E2M2	**EVOLUTION, ECOSYSTEME, MICROBIOLOGIE, MODELISATION** **http://e2m2.universite-lyon.fr** Insa : H. CHARLES	Mme Gudrun BORNETTE CNRS UMR 5023 LEHNA Université Claude Bernard Lyon 1 Bât Forel 43 bd du 11 novembre 1918 69622 VILLEURBANNE Cédex Tél : 06.07.53.89.13 e2m2@ univ-lyon1.fr
EDISS	**INTERDISCIPLINAIRE SCIENCES-SANTE** **http://www.ediss-lyon.fr** Sec : Samia VUILLERMOZ Insa : M. LAGARDE	M. Didier REVEL Hôpital Louis Pradel Bâtiment Central 28 Avenue Doyen Lépine 69677 BRON Tél : 04.72.68.49.09 Fax :04 72 68 49 16 Didier.revel@creatis.uni-lyon1.fr
INFOMATHS	**INFORMATIQUE ET MATHEMATIQUES** **http://infomaths.univ-lyon1.fr** Sec :Renée EL MELHEM	Mme Sylvie CALABRETTO Université Claude Bernard Lyon 1 INFOMATHS Bâtiment Braconnier 43 bd du 11 novembre 1918 69622 VILLEURBANNE Cedex Tél : 04.72. 44.82.94 Fax 04 72 43 16 87 infomaths@univ-lyon1.fr
Matériaux	**MATERIAUX DE LYON** **http://ed34.universite-lyon.fr** Secrétariat : M. LABOUNE PM : 71.70 –Fax : 87.12 Bat. Saint Exupéry Ed.materiaux@insa-lyon.fr	M. Jean-Yves BUFFIERE INSA de Lyon MATEIS Bâtiment Saint Exupéry 7 avenue Jean Capelle 69621 VILLEURBANNE Cedex Tél : 04.72.43 83 18 Fax 04 72 43 85 28 Jean-yves.buffiere@insa-lyon.fr
MEGA	**MECANIQUE, ENERGETIQUE, GENIE CIVIL, ACOUSTIQUE** **http://mega.ec-lyon.fr** Secrétariat : M. LABOUNE PM : 71.70 –Fax : 87.12 Bat. Saint Exupéry mega@insa-lyon.fr	M. Philippe BOISSE INSA de Lyon Laboratoire LAMCOS Bâtiment Jacquard 25 bis avenue Jean Capelle 69621 VILLEURBANNE Cedex Tél :04.72 .43.71.70 Fax : 04 72 43 72 37 Philippe.boisse@insa-lyon.fr
ScSo	**ScSo*** **http://recherche.univ-lyon2.fr/scso/** Sec : Viviane POLSINELLI Brigitte DUBOIS Insa : J.Y. TOUSSAINT	M. OBADIA Lionel Université Lyon 2 86 rue Pasteur 69365 LYON Cedex 07 Tél : 04.78.77.23.86 Fax : 04.37.28.04.48 Lionel.Obadia@univ-lyon2.fr

*ScSo : Histoire, Géographie, Aménagement, Urbanisme, Archéologie, Science politique, Sociologie, Anthropologie

Abstract

This work deals with the mechanical properties and damage mechanisms under contact loading of dense and porous silicon nitrides materials. These technical ceramics exhibit a very interesting combination of mechanical properties : low density, high hardness and strength, good corrosion resistance and a low thermal coefficient. They are used in many applications including ball bearings for the automotive and aerospace industries. The characterization of the local behaviour under contact loading is then a crucial issue.

Spark plasma sintering technique is used to process silicon nitride ceramics with addition of different amount of yttrium oxide as sintering aid. Controlling the sintering temperature and the applied pressure has permitted to obtain materials with fine, medium and coarse microstructures. In addition, materials with different porosity contents have been obtained. First, we have investigated the influence of processing conditions (temperature, pressure, amount of yttria on the microstructure and mechanical properties at the macroscopic scale (elastic parameters, Vickers hardness, flexural resistance ...).

Hertzian contact tests were then performed to identify the damage mechanisms at the surface and subsurface of the sintered materials. The use of indenting spheres of different radii permitted to observe a significant size effect. Brittle mode consisting of surface ring cracks were observed at large scale (macroscopic scale) while localized plastic deformation with microcracks randomly distributed was observed at small scale (mesoscopic scale). Transmission electron microscopy observations of thin foils machined by ion milling were performed to investigate the subsurface damage. Numerical simulations with a code developed internally in LaMCoS laboratory enabled to follow the evolution of the plastic zone under pure rolling conditions.

In these simulations, the nonlinear behaviour of ceramics was modelled using a bilinear law where σ_y is the yield stress and K a hardening parameter of the ceramic specimen. Instrumented indentation tests were performed using a diamond spherical tip of radius 42 μm. Experimental load versus displacement curves were used as input data for an inverse identification purpose. Levemberg-Marquart algorithm was used to minimize the gap in the least squares sense.

The work revealed a strong relationship between the damage mechanisms under contact loading (brittle vs quasi-ductile modes) and the grain sizes. The presence of higher porosity volume content led to precursor damage initiation. In addition, the obtained nonlinear parameters from inverse analysis, i.e σ_y and K, decrease with increasing the microstructure coarseness. This result is consistent with the literature and the Hall-Petch model. On the other hand, a significant influence of the porosity on the identified parameters was demonstrated. Finally, the comparison of experimental and numerical indent profiles clearly show the limitations of bilinear law, a more advanced model is then needed to consider all the damage mechanisms.

KEYWORDS: Silicon nitride, microstructure, porosity, contact damage, inverse identification

Résumé

Ces travaux de thèse portent sur la détermination des propriétés mécaniques à différentes échelles ainsi que les mécanismes d'endommagement des nitrures de silicium denses ou avec différents taux de porosités. Ces céramiques techniques présentent des propriétés mécaniques forte intéressantes : une faible densité, une dureté élevée, une bonne résistance à la corrosion et un faible coefficient de dilatation thermique. Elles sont notamment utilisées dans la fabrication des billes de roulement pour des applications dans les industries automobiles et aéronautiques. La caractérisation du comportement local sous un chargement de contact est donc un enjeu majeur.

Les matériaux étudiés ont été obtenus par frittage flash d'une poudre de Nitrure de Silicium avec différents pourcentages d'oxide d'yttrium comme additif. Le contrôle de la température et de la pression de frittage a permis d'obtenir des matériaux denses avec différentes tailles de grain mais aussi avec une porosité résiduelle variable.

La première partie de ce travail consistait à caractériser l'influence des conditions d'élaboration (température, pression, pourcentage d'additif) sur la microstructure (taille des grains, compositions ...) et les propriétés mécaniques à l'échelle macroscopique (module élastique, dureté Vickers, résistance à la flexion ...) des matériaux frittés. Des essais de contact de Hertz ont été ensuite réalisés afin d'identifier les mécanismes d'endommagement. L'utilisation de sphères de différents rayons a mis en évidence un important effet d'échelle : des fissures circonférentielles à échelle macroscopique (mode fragile) et des déformations plastique localisées à l'échelle mesoscopique avec des micro fissures distribuées aléatoirement (mode quasi-ductile).

Les tests de nanoindentation permettent de solliciter localement les échantillons pour obtenir les propriétés élastiques des courbes force-déplacement. Des méthodes d'identification inverses permettent aussi d'extraire les paramètres d'écoulement.

Le comportement non linéaire des céramiques a été modélisé en utilisant une loi bilinéaire où σ_y est la limite d'élasticité et K un paramètre d'écrouissage. Afin d'identifier ces deux paramètres, un modèle éléments finis axisymétrique avec une pointe sphérique déformable a été construit sous Abaqus. Le modèle a été couplé à un module d'identification inverse fondé sur l'algorithme de Levemberg-Marquart pour minimiser l'écart (au sens des moindres carrés) entre les courbes expérimentales et numériques. Les simulations avec le code Isaac développé au sein du laboratoire LaMCoS ont permis de suivre d'évolution de la zone plastique lors d'un chargement de roulement.

L'étude a révélé une relation majeure entre les mécanismes d'endommagement sous chargement de contact et la taille des grains. En outre, la limite d'élasticité σ_y calculée par analyse inverse diminue avec l'augmentation de cette taille des grains. Ce résultat est en accord avec la littérature et le modèle de Hall-Petch. Les valeurs élevées pour K confirment la dominance d'une réponse élastique des matériaux frittés. D'autre part, une influence significative de la porosité sur la nature de la réponse et les paramètres identifiés a été observée. Enfin, la comparaison des profils expérimentaux et numériques des indents a montré les limites de la loi bilinéaire, un modèle plus avancé est donc nécessaire afin de décrire tous les phénomènes.

MOTS CLÉS : Nitrure de Silicium, microstructure, porosité, contact, identification inverse

Contents

List of Figures

List of Tables

publications

Journal papers

– Azeggagh, N., Joly-Pottuz, L., Nélias, D., Chevalier, J., Omori, M., and Hashida, T. (2015). Hertzian contact damage in silicon nitride ceramics with different porosity contents. Journal of the European Ceramic Society, 35(8), 2269-2276 *(link)*

– Azeggagh, N., Joly-Pottuz, L., Chevalier, J., Omori, M., and Hashida, T., Nélias, D. (2015). Indentation strength of silicon nitride ceramics processed by spark plasma sintering technique. Materials Science and Engineering : A *(link)*

Conference papers

– 2015
Azeggagh, N. et *al*. Hertzian contact damage in dense and porous silicon nitride. 14th International Conference European Ceramic Society. June 21-25, 2015 in Toledo, Spain *(link)*

Azeggagh, N. et *al*. Indentation strength of silicon nitride ceramics. 7^{th} annual ELyT Workshop. February 19-21, 2015 in Matsushima, Japan *(link)*

– 2014
Azeggagh, N. et *al*. Hertzian contact damage in Silicon Nitride ceramics elaborated by Spark Plasma Sintering technique. 14^{th} European Inter-Regional Conference on Ceramics. September 8-10, 2014 in Stuttgart, Germany *(link)*

Azeggagh, N. et *al*. Détermination des paramètres rhéologiques des nitrures de silicium par méthode inverse, Colloque du groupe indentation multiéchelle. 10 -12 décembre 2014 à Strasbourg, France *(link)*

General introduction

In order to satisfy growing needs in terms of energy efficiency and to face increasing competition, vehicle manufacturers and aerospace equipment makers in particular are continuously looking for materials characterized by a density as low as possible. The suitable materials should also present good mechanical and thermal properties. The applications intended are in severe environments (high temperatures, corrosive media ...). Technical ceramics and especially silicon nitride based materials are considered as an ideal candidate thanks to a satisfactory toughness, high hardness, good wear and corrosion resistance. However, when subjected to tribological solicitations where high pressure and shear stress fields apply, various contact damage modes may initiate on the surface or subsurface. Accordingly, the lifetime of critical components is sharply reduced which may generate additional maintenance costs in the best cases and a catastrophic failure in the worst circumstances.

The main objective of this work is threefold :
(i) investigate the contact damage mechanisms on silicon nitride materials with different microstructures, (ii) observe the contact damage and the macroscopic and mesoscopic scale in fully dense and porous materials and (iii) derive the local nonlinear mechanical properties from the load versus displacement curves (*P-h* curves) obtained by instrumented indentation technique (ITT). In fact, we will experimentally demonstrate that brittle materials can undergo a permanent deformation at the mesoscopic (small) scale.

Silicon nitride is synthesized through several different chemical reaction methods, conventional or non-conventional one. The materials considered in the following work were processed by spark plasma sintering (SPS) technique with addition of small amount of yttrium oxide as sintering aid. This step was performed within the framework of ElyT Lab, a join French-Japanese research laboratory. Silicon nitride specimens with fine, medium and large grain sizes and various porosity volume contents were successfully obtained by optimising the processing conditions (additive amount, temperature and applied pressure).

The manuscript is structured around four main parts :

I- The first chapter is devoted to a general literature review of different issues : we recall some generalities (mechanical properties, microstructure, phase composition ...) about technical ceramics and their application domains. Next, the different contact damage mechanisms in case of brittle materials are recalled and their effects on the lifetime are highlighted. Finally, the weaknesses of the existing approaches used to derive the stress-strain of hard brittle materials are pointed up.

II- The second chapter of this manuscript shortly describes the numerical methods and experimental procedures considered in this work. The experimental side consists of focused ion

beam (FIB) sectioning technique in addition to transmission electron microscopy (TEM) observation of subsurface damage mechanisms. On the other hand, the numerical work deals with the inverse identification to get true stress-strain curves from the instrumented indentations tests. Once the plastic parameters obtained, these curves are used as input data to simulate the evolution of the plastic zone under vertical loading and pure rolling load using internally developed semi-analytical code.

III- The third chapter is about dense silicon nitride materials. The microstructure and mechanical properties are first characterized and analysed. Inverse identification is performed with MiC2M, an algorithm developed by Dr F. Richard from Franche-Comté University, will be coupled with commercial Abaqus software to perform inverse identification. Then, the effect of grain sizes on the non-linear parameters is presented and discussed. Once uniaxial $\sigma - \varepsilon$ relation obtained, the curves are used as input data in order to simulate the evolution of the plastic zone under vertical and pure rolling loadings.

IV- The last chapter is dedicated to the specific case of silicon nitride materials presenting some residual randomly distributed pores. This case is to simulate the event of an unexpected porosity resulting from not optimized processing conditions. The microstructure and mechanical properties are introduced and discussed, then the surface and subsurface damage phenomena are analysed. Finally, the effect of porosity content on the non-linear mechanical parameters is discussed.

The manuscript ends with a summary of the main results obtained and an overview of some possible perspectives.

Chapter 1

State of the art

In this first chapter, we address a brief bibliographic review regarding the various fields considered in this work. First, the main mechanical properties and domains of application of the technical ceramics are recalled. Then, conventional and non-conventional processing techniques are introduced and compared to spark plasma sintering considered to process our materials. Main developments of silicon nitride is presented. The different surface and subsurface contact damage mechanisms for dense and porous silicon nitride under vertical loading are shortly recalled. Finally, the principles of the inverse identification procedure are presented and its application to the special case of brittle materials is discussed.

Contents

1.1 Advanced structural ceramics

1.1.1 Generalities

Ceramics are inorganic and non-metallic materials. Their microstructure can be of crystalline or amorphous nature (in the case of glass for example). Etymologically speaking, the origins of appellation "ceramic" as we know it today is traced back to the Greek term keramos, meaning potter's clay or pottery. Keramos in turn is related to an older Sanskrit root meaning to burn [ACerS, 2014]. This proves that our ancestors were immediately aware of the close relationship between the processing of this class of materials and heating. Over the centuries, the history of humanity has been intimately linked to development of ceramic based materials. Figure 1.1 shows the evolution of ceramic manufacturing and discoveries according to the American Ceramic Society [ACerS, 2014]. The first ceramic objects made by mixing water, clay and other raw materials, were in the form of simple small animal, human figurines and balls. They tells us and reveal religious beliefs, cultural and other aspects of human life through the ages. For reference, the oldest ceramic production is the Venus of Dolni Vestonice found in a palaeolithic site located in the south of Czech Republic [Vandiver et al., 1989]. According to the archaeologists, this small figurine date back to at least 25000 BC making ceramic firing one of the oldest and most widespread of human arts and activities.

Year	Development
24,000 B.C.	Ceramic figurines used for ceremonial purposes
14,000 B.C.	First tiles made in Mesopotamia and India
9000-10,000 B.C.	Pottery making begins
5000-8000 B.C.	Glazes discovered in Egypt
1500 B.C.	Glass objects first made
1550 A.D.	Synthetic refractories (temperature resistant) for furnaces used to make steel, glass, ceramics, cement
Mid 1800's	Porcelain electrical insulation Incandescent light bulb
1920's	High-strength quartz-enriched porcelain for insulators Alumina spark plugs Glass windows for automobiles
1940's	Capacitors and magnetic ferrites
1960's	Alumina insulators for voltages over 220 kV Application of carbides and nitrides
1970's	Introduction of high-performance cellular ceramic substrates for catalytic converters and particulate filters for diesel engines
1980's	High temperature superconductors

FIGURE 1.1: Evolution of Ceramic and Glass Developments [ACerS, 2014]

Ceramic materials have been considered for a long time as traditional because of their domain of applications and production ways. However, over the last decades of 20^{th} century a generation of technical ceramics also refereed to as engineering or advanced ceramics, has been developed. The contributions in the development of this new class of ceramic based materials came in large part from the research programs initiated in the United States, Europe and Japan. According to the American of Testing and Materials (ASTM), technical ceramic is defined as a highly engineered, high performance, predominantly non-metallic, inorganic ceramic material having specific functional attributes.

There are various classification of ceramic materials which may depend on the application or composition. The technical ceramics are organized around three main families : oxide, non-oxide and composite materials. We will not go into detail regarding the characteristics of each family, but just give some examples for illustration purpose :

1. Oxide ceramics : They are inorganic compounds of metallic (e.g., Al, Zr, Ti, Mg) or metalloid (Si) elements with oxygen. As example, one can mention aluminium oxide (Al_2O_3), zirconium oxide (ZrO_2) and aluminium titanate (Al_2TiO_5).
2. Non-oxide ceramics : they are based on carbon, nitrogen and silicon. This family includes nitrides (Si_3N_4 for example) and carbides. This group of materials generally requires quite high temperatures of sintering.
3. Composite ceramics : This family is rapidly developing and it is most often a combination of two oxides or two non-oxide but also combinations between members of the two families. Composite ceramics also include polymers and metals in particulate or matrix form. Cermets composed of ceramic (cer) and metallic (met) materials are the leading elements of this class. They are mainly produced by casting and powder metallurgy methods [Kaczmar et al., 2000].

1.1.2 Mechanical properties

It is well established that the mechanical properties of materials is intimately related to nature of basic constituents and their bonding at the atomic scale. In the case of ceramic materials, two types of atomistic bonding are dominant : ionic and covalent. These strong bondings are what make the specific features of this material class. In fact, technical ceramics exhibit a remarkable combination of mechanical, electrical, thermal and biochemical properties. Some of them have good wear, oxidation and corrosive resistance in addition to an excellent thermal shock resistance [Riley, 2000, Hampshire, 2007]. Furthermore, ceramics are also lightweight when compared to most metals, which is suitable to reduce the energy consumption and thus the cost in many applications. In addition, ceramics are also characterized by high melting points, enabling them to maintain interesting mechanical properties at high temperatures.

The Achilles' heel of ceramic materials is their low tolerance to the presence of surface or bulk flaws which can be produced during the processing of the specimens or parts. If a critical flaw is found in the material volume solicited during loading, it generates stress concentration high enough to cause cracking and then failure. Fracture occurs instantaneously after small range of elastic deformation. However, the resistance to crack propagation may be significantly improved by taking advantage of several possible toughening mechanisms : phase transformation in zirconia

for example [Heuer, 1987, De Aza et al., 2002], crack bridging and deflection [Steinbrech, 1992, Hutchinson, 1989] for silicon nitride and others. Considerable efforts were made to control the microstructure by the optimization of the processing conditions of already existed manufacturing technique or with introducing new ones.

These improvements permitted for example to process ceramics with a high toughness up to 20 MPa $m^{1/2}$ and elevated strength [Bouville et al., 2014]. As previously mentioned, it was also found that ceramic materials can also be combined either as a matrix or reinforcements with other materials to form composites [Christman et al., 1989]. The materials may then exhibit improved mechanical and electrical properties thereby offering new perspectives [Kaczmar et al., 2000, Yamamoto et al., 2008].

1.1.3 Application domains

As presented in the previous section, technical ceramics present an interesting wide range of mechanical properties at room and high temperature. This makes possible the use of these materials in numerous industrial domains. One can cite for example aeronautic and automotive industry, electronics, medical technology and energy. In addition, the materials are expected to operate in severe environment. We give thereafter a non-exhaustive list of examples of technical ceramic products to highlight the importance of this material class. Zirconium oxide for example finds several application in materials for crowns and bridges in the dental industry. Alumina-zirconia composites are extensively used for hip joint replacements [Chevalier, 2006].

Silicon carbide (SiC) is another attractive ceramic materials. It is widely used in high temperature pressure sensors [Wu et al., 2006], room temperature light-emitting diodes [Fuchs et al., 2013], high microwaves devices [Willander et al., 2006], heat exchangers, fixed and moving turbine components.

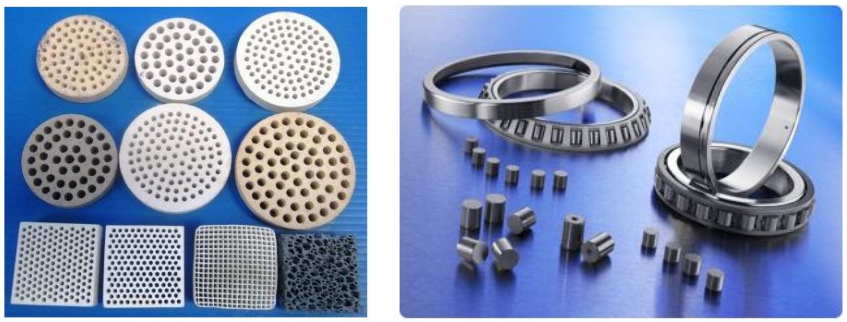

(a) Ceramic filters (b) Rolling elements

FIGURE 1.2: Some applications of technical ceramics

Silicon nitride based materials, which will be the subject of our study, have been widely used in various industrial domains since 1950s. For example, Kristic [Krstic and Krstic, 2012] mentioned applications in nuclear fusion reactors, construction of thermal conductors and gas turbines. Hampshire [Hampshire, 2007] cited structural application at high temperatures in turbocharger rotors while Bal and Rahaman [Bal and Rahaman, 2012] reported recent clinical use of silicon

nitride to promote bone fusion in spinal surgery and current developments as femoral heads for hip joints. Today, rolling bearing manufacturing companies are increasingly turning to Si_3N_4 with a growth of about 40% per year. High-pressure turbo-pumps on NASA space shuttles are a representative example [Nasa, 2000]. In addition, porous silicon nitride is used for hot gas filtration to reduce emission of corrosive and toxic particle [Yang et al., 2003].

Finally, the composites based on ceramic materials are used to reduce the weight and thus fuel consumption. As application, one can mention cylinder sleeves in engines, piston-recess walls, brake discs and bearings [Ceramtec, 2015]. More particularly, cermets are used for cutting, drilling tools and electrical components [Humenik and Parikh, 1956].

1.2 Processing techniques

Sintering is an irreversible thermodynamic process which is used to form different components and parts of simple or complex geometry from the material starting raw powder. The technology has its origins in the prehistoric age with the pottery firing. In the ideal case, it is possible to control the grain sizes of microstructures by optimizing the experimental processing conditions (temperature and pressure). The size of particle is also of paramount importance on the final microstructure grain size. It is accepted by scientific community that the driving force behind the sintering process is the reduction of total free energy of the system $\Delta(\gamma A)$ [Kang, 2004] :

$$\Delta(\gamma A) = \Delta\gamma A + \gamma\Delta A \tag{1.1}$$

Where γ is the specific energy of powder particle and A the total area of the particles. Densification and grain growth are the main phenomena behind the sintering as schematically presented in FIG.1.3. It is clear that if a fine microstructure is needed, densification has be promoted over grain growth. Sintering stops when $\Delta(\gamma A)$ tends to zero.

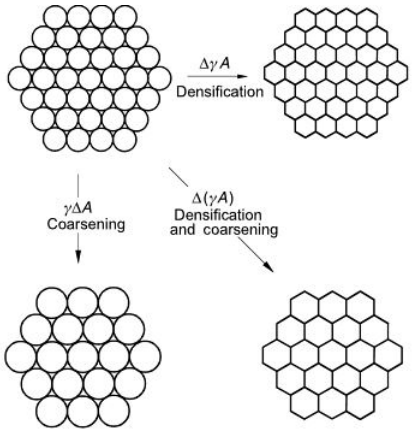

FIGURE 1.3: Mechanisms during sintering [Kang, 2004]

Two kinds of sintering may occur : solid state sintering and liquid phase sintering. This latter one occurs when more than one component is contained in the powder compacts (addition of sintering additive for example) [Kang, 2004]. The sintering mechanisms are complex and include several physical phenomena such as surface diffusion of atoms, vapour transport and grain boun-

dary transport. These mechanisms and others are schematically represented in FIG.1.4 [Somiya, 2013].

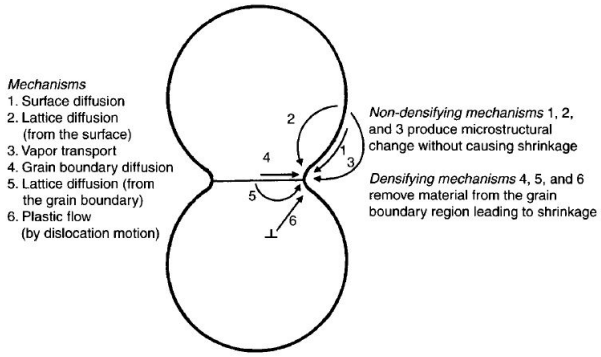

FIGURE 1.4: Mass transport mechanisms during sintering process [Kang, 2004]

1.2.1 Conventional sintering techniques

Over the last century, several techniques have been developed to process ceramic based materials from the starting powders. All the techniques final aim is to compact the material green powder to partially or fully dense specimens and parts. It was also found that addition of small amounts of sintering elements may lead to a higher density [Somiya, 2013]. We present below three techniques widely used in the of research and industrial fields for the preparation of ceramic materials.

1.2.1.1 Natural sintering

This technique, also referred to as pressureless sintering, emerged as the easiest approach. It is widely used in the industry to process ceramic materials for economic considerations as the component can be formed to near-net shape. Pressureless sintering, as its name suggests, doesn't require application of an external mechanical force and it is particularly appropriate for materials difficult to be sintered. However, fully densification is not often obtained even with addition of substantial amount of additives [Terwilliger and Lange, 1975] and high sintering temperatures, up to 2100 °C [Chamberlain et al., 2006].

1.2.1.2 Hot pressing HP

The hot pressing is achieved by the simultaneous application of heat and unidirectional mechanical pressure, a schematic presentation of the system is presented in FIG.1.5a. Sintering is conducted by positioning the material powder or mixture into a suitable die. Graphite dies are usually used because of their excellent creep resistance at high temperature. An uniaxial pressure is applied while the entire system is held at an elevated temperature. Hot Pressing is only suited to relatively simple shapes, with the components usually requiring diamond grinding to achieve the finished tolerances.

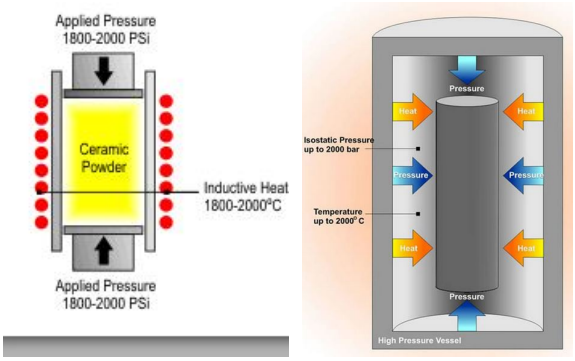

(a) Hot pressing (b) Hot isostatic pressing

FIGURE 1.5: HP and HIP systems

1.2.1.3 Hot isostatic pressing HIP

It has been reported that hot isostatic pressing technique can lead to fully dense specimens at lowest temperature in the conventional technique family [Bowles and Witkin, 1979]. This technique is able to remove both micro and macro porosities. In contrast to the technique described previously, here the pressure is uniformly applied (isostatic pressure) by an inert gas, see FIG.1.5b. Argon (Ar) or nitrogen (N) are often used. The most attractive thing about isostatic pressing in the fact that the powder is compacted with the same pressure in all directions, more homogeneous microstructures are then obtained. The process is generally used in the production of billets of superalloys, high-speed steels, titanium and ceramics. Finally, HIP can also performed after natural sintering to enhance the densification without additional grain growth.

1.2.2 Non-conventional techniques : SPS

1.2.2.1 Description

The spark plasma sintering technique (SPS), also known by the acronym FAST (Field Activated Sintering Technique) belongs to what is referred to as Electric Current Activated Sintering (ECAS) techniques [Belmonte et al., 2010]. The origins of ECAS go back to the beginning of the 20^{th} century in the Unites States where the first system was patented by G. Taylor in 1933 [Taylor, 1933]. The objective was sintering of cemented carbide and the challenge was to obtain heating rates as high as possible. A breakthrough in the development of this technique was made in the early of 1960^{th} in Japan by Inoue [Inoue, 1966] who patented the first SPS apparatus for application on low melting point metals. The first commercial spark plasma machine was proposed much later, in early 1990^{th}, by Sumitomo Heavy Industries Ltd. (Japan) after expiration of Inoue's patent [Suarez et al., 2013]. The technique offers many several advantages over the cited conventional systems. Figure 1.6a is a schematic representation of the SPS system. The starting powder mixtures are first enclosed in graphite die with appropriate geometry between two hard punches. The assembly is then placed inside the machine vacuum chamber. A water circuit serves to cool the whole system, additional cooling can be performed by introducing a gas. The measurement of the temperature is performed using thermocouples or optical pyrometers which position (axial or

radial) depend on the system manufacturer.

It is demonstrated that the SPS technique has the capability to compact the ceramic powders in a drastically shorter time and at temperatures lower by 200 to 500 °C than the other processing techniques. In fact, complete sintering may take place in few minutes in contrast with conventional techniques requiring several hours. These advantages result from the simultaneous application of a pulsed (on-off) low voltage direct current of a few thousand amperes on the die and a uniaxial mechanical pressure on the upper and lower punches during the sintering process. Depending on the system and powder properties, heating rates as high as 1000 °/min can be obtained. The high current generates highly localized Joule heating at the contact between the powder particles, see FIG.1.6b. In addition, it is often proposed that pulsed direct current leads to surface cleaning and activation of powders which in turn enhance the densification [Belmonte et al., 2010]. Thermal and electrical field evolutions during sintering were simulated based on finite element models[Vanmeensel et al., 2005, Tiwari et al., 2009, Mondalek et al., 2011]. Depending of the die and powder electrical properties, different current paths were obtained. During sintering, heating lead to the evaporation and melting of particle surface and necks are then formed. The applied pressure takes advantage of this mechanism and permits to rapidly suppress the pores and achieve full densification with limited grain growth in polycrystalline materials. Therefore, materials with nano-sized microstructure can be obtained. The short processing time also limits the degradation of the original characteristics of the compacts. Finally, SPS do not require pre-compaction for the green powders.

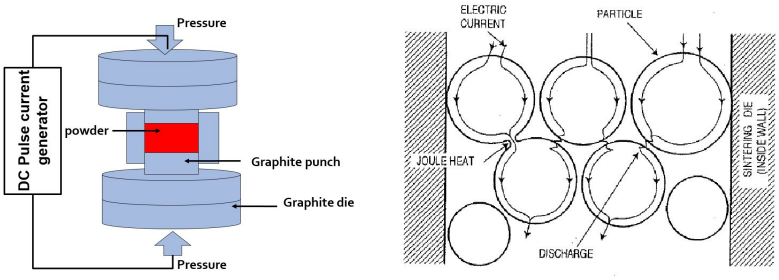

(a) Schematic representation of an SPS system

(b) Current path during sintering

FIGURE 1.6: SPS system and current path through material powder particles [Suarez et al., 2013]

The number of peer review publications related to material processing using SPS technique is found to be higher than 500 in 2011 with more than 5000 citations [Suarez et al., 2013]. This provides evidence of the prominent position of this technique in the material processing field. However, despite this achievement spark plasma sintering technique present several weak points. The first one concern the mechanisms behind the densification which are still under investigation. In fact, regardless of the numerous investigations and initial speculations, plasma generation was not experimentally demonstrated yet at least in ceramics [Hulbert et al., 2008]. It is argued that the voltage concentration is not high enough to create sparks. Secondly, because the most applications of this technique are dedicated to material development in the research field, several adjustments are necessary to adapt SPS systems to the industrial applications where more reproducible, sustained

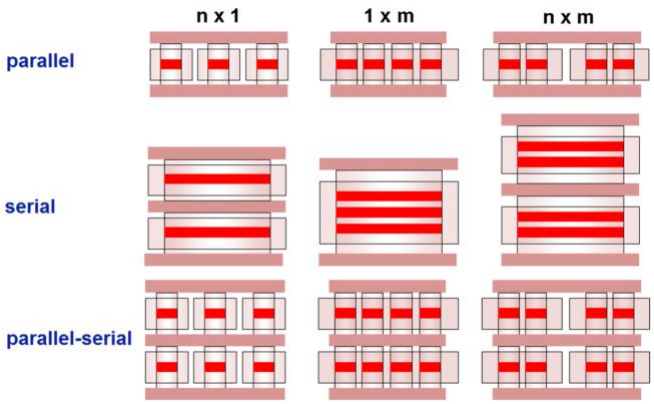

FIGURE 1.7: Production of multiple parts using SPS [Guillon et al., 2014]

production and near shape processing are necessary. This impediment is currently gradually being overcome and innovative designs for continuous production by parallel, serial or parallel-serial alignments were presented as shown for illustration in FIG.1.7.

1.2.2.2 Related materials

Good knowledge of the flash sintering technique by the scientific community and its flexible power supply make possible processing of wide range of conductive or not conductive materials from the starting powders. The researchers quickly realized that the system set up is versatile, various adjustments giving rise to large number of patents were proposed. Example of symmetric configuration of heating elements (a), asymmetric location of the graphite die (b) and asymmetric graphite die are shown in FIG.1.8 [Guillon et al., 2014].

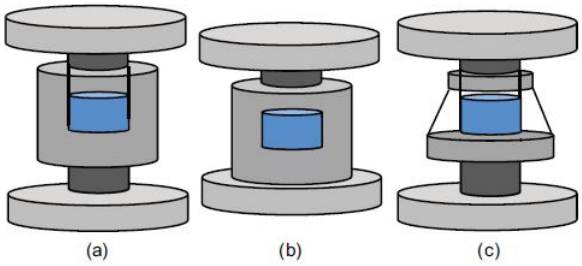

FIGURE 1.8: Different configuration of the SPS system

There is a long list of materials obtained by standard or optimized spark plasma sintering systems. One cite for example transparent ceramic obtained from high purity powders an appropriate sintering conditions. In fact, The technique made it possible to limit grain growth [Bonnefont et al., 2012], see FIG.1.9a Functionally graded or layered material structures (FGM) are innovative materials with gradual change in the phase composition, grain size or porosity as shown in FIG.1.9b. This therefore generates mechanical properties gradients over the volume of the specimen. Application of FGM in various fields : cutting tools and machine parts. Composite materials with ceramic or polymer materials as matrix and carbon nanotube as reinforcements were also successfully sintered [Hu et al., 2008, Wang et al., 2015]. The technique was also successfully used

to sinter non-equilibrium materials, nanostructured materials in addition to ultra-high temperature ceramics (UHTC).

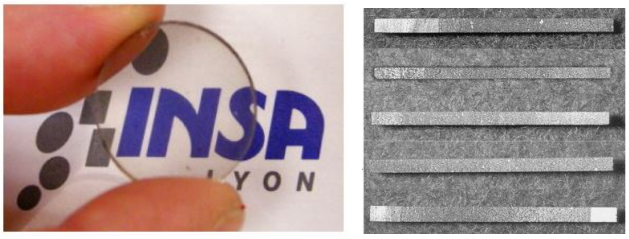

(a) Transparent ceramics [Bonnefont et al., 2012]

(b) Functionally graded materials [Watari et al., 2004]

FIGURE 1.9: Materials related to SPS technique

1.3 Hertzian contact damage

1.3.1 Stress field

It is obvious that the material response under Hertzian contact is related to the associated applied load and thus to the resulting stress field. Let's consider the fundamental problem of a contact of spherical indenter of radius R which mechanical behaviour is described by its elastic modulus E_i and Poisson's ratio ν_i on a elastic isotropic flat half space characterized by an elastic modulus E_s and Poisson's ratio ν_s, see FIG.1.10a. Thereafter, the indices i and s will refer to the indenter and specimen, respectively. The objective here is to recall only the essential relations obtained by Hertz [Hertz, 1881]. For more details about the derivation of the equations represented thereafter, the reader is kindly asked to refer to [Johnson, 1987].

Hertz established in 1886 that the contact region is circular with a radius a given by :

$$a = [\frac{3PR}{4E_r}]^{1/3} \tag{1.2}$$

Where P is applied normal load and E_r the reduced elastic modulus defined as follows :

$$E_r = [\frac{1-\nu_s^2}{E_s} + \frac{1-\nu_i^2}{E_i}]^{-1} \tag{1.3}$$

In contact mechanics, the pressure is one of most important parameter of the problem. This parameter allows to define equivalent loadings when the other geometrical parameters are different. The resulting pressure is of a parabolic profile (FIG.1.10b) and may be calculated as a function of the radial distance from the axis of contact r , the radius a and P_{hertz}

$$\begin{cases} P_{hertz}[1-(\frac{r}{a})^2]^{-1/2} & \text{if } r \leq a \\ 0 & \text{if } r > a \end{cases} \tag{1.4}$$

Where P_{hertz} is the maximum value of the pressure at the center of contact zone ($z = 0$, $r = 0$) ,

$$P_{hertz} = [\frac{6PE_r^2}{\pi^3 R^2}]^{1/3} \tag{1.5}$$

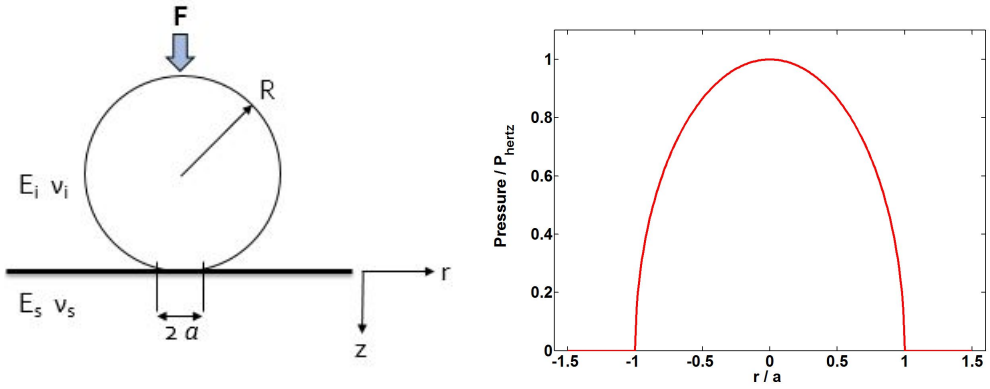

(a) Hertzian contact of a sphere on a flat specimen (b) Hertzian surface pressure profile

FIGURE 1.10: Schematic representation of a flat surface - sphere contact (a) and resulting pressure distribution (b)

One must be aware that the equations introduced before are effective only under some restrictive hypothesis regarding principally the mechanical behaviour of the two solid in contact, i.e $a \ll R$. In fact, the theory is only valid in the elastic domain which is often the case for the brittle materials of this study. The second hypothesis concerns the size of the contact area which must remain small when compared to size of the two bodies in contact. Finally, no friction is taken into account in the derivation of the theory.

Concerning the stress field, the radial component is compressive at the subsurface level and tensile on the surface of the specimen ($z = 0$, $r \geq 0$) :

$$\sigma_{rr} = \frac{1-2\nu_s}{2}\frac{P}{\pi a^2}(\frac{a}{r})^2 \tag{1.6}$$

The maximum of σ_{rr} is then reached at the circumference of the contact zone, ($r = a$). The value is given by :

$$\sigma_{rr}^{max} = \frac{1-2\nu_s}{2}\frac{P}{\pi a^2} \tag{1.7}$$

For $\nu_s = 0.3$ which is a typical value engineering ceramics, $\sigma_{rr}^{max} \approx 0.2\ P\ /\ \pi a^2$

On the other hand, the shear stress field is defined as follows :

$$\tau = \frac{1}{2}\mid \sigma_1 - \sigma_3 \mid \tag{1.8}$$

The maximum of the shear stress is calculated as follows,

$$\tau_m = 0.47\frac{P}{\pi a^2} \tag{1.9}$$

This value is reached at subsurface location equal to one half the contact radius, $z \approx 0.5\ a$. An illustration example of tensile and radial stress contours is given in FIG.1.11.

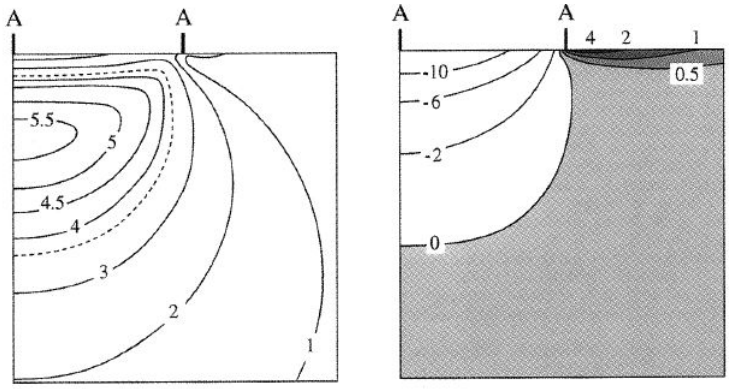

(a) Shear stress field (GPa) (b) Tension stress field (GPa)

FIGURE 1.11: Elastic stress contours from Tungsten sphere of radius 1.98 mm under peak load P = 3000 N [Lawn et al., 1994]

1.3.2 Case study : Silicon nitride

The history of silicon nitrides goes back to second half of the 19^{th} century. The ceramic was first developed by Deville and Wöhler in 1859 but remained merely a chemical curiosity for decades. The starting powder may be obtained by means of nitridation of silicon, chemical vapour deposition and carbon thermal reduction of silica [Hampshire, 2009]. Starting from the second half of the 20^{th} century, Si_3N_4 attracted broad interest. Several ambitious projects have emerged particularly in the United States in order to use this ceramic in commercial applications [Riley, 2000].

Silicon nitride is chemically Si_3N_4, it is available in two main types : reaction bonded and sintered. Both types are non-oxide ceramic which exist in two major crystalline modifications : α-Si_3N_4 and β-Si_3N_4 (a third phase, cubic Si_3N_4 was synthesised under high conditions of temperature and pressure [Zerr et al., 1999]). The most common phases are a trigonal α metastable form at low temperatures and hexagonal thermodynamically more stable β form, see FIG.1.12. Idealised α and β forms have unit cells consisting of $Si_{12}N_{16}$ and S_6N_8, respectively. α-Si_3N_4 is assigned to space group P31c and β-Si_3N_4 to space group $P6_3/m$ [Riley, 2000]. The lattice parameters and intrinsic mechanical properties of the α-Si_3N_4 and β-Si_3N_4 are reported in TAB.1.1. The two phases exhibit a marked difference in cristallography and thus dissimilar mechanical properties. In fact, it was experimentally demonstrated that the phase β itself is highly anisotropic. Different elastic modulus and yield stress were reported for the basal and prismatic orientations [Csanádi et al., 2015]. In light of these values, it can be argued that the phase composition, ratio α / β is generally used, will be a critical parameter on the mechanical properties of the final product. At temperature higher than 1880 °C, silicon nitride does not melt but dissociate into silicon and nitrogen [Riley, 2000]

$$Si_3N_4 = 3Si(g,l) + 2N_2(g) \tag{1.10}$$

Because of its high boundary energy and low diffusivity coefficient, sintering of fully dense Si_3N_4 by means of conventional or unconventional techniques requires addition of small amounts

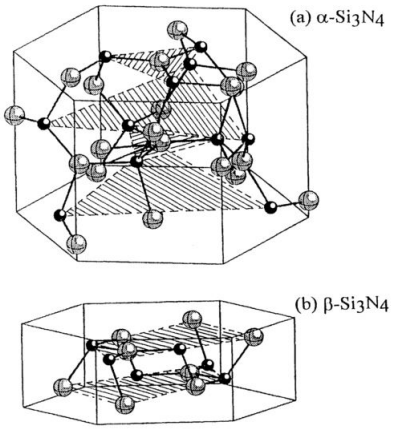

FIGURE 1.12: Structure of α and β silicon nitride phases

of various additives (MgO, Al_2O_3,Yb_2O_3, La_2O_3...) [Wang et al., 2014, Goto and Thomas, 1995, Hirosaki et al., 1988]. During the sintering process, the additives react with the silicon nitride and the silica present at surface of each single powder to form an intergranular glassy film. This phase is few nanometres thick, it enhances precipitation and rearrangement mechanisms needed to achieve full densification but strongly impacts the mechanical and thermal behaviour of silicon nitride materials at room and elevated temperatures [Tsuge et al., 1975, Kitayama et al., 2001, Satet and Hoffmann, 2005]. One can here make an important addition about the input from using spark plasma sintering technique. Indded, by sintering at lower temperatures, the intrinsic characteristics of silicon nitride are minimally deteriorated.

1.3.3 Damage in dense Si_3N_4 ceramics

As mentioned previously, because of its high hardness and wear resistance, one of the major application of silicon nitride is rolling element bearings. They have four components : an inner race, an outer race, rolling elements and a cage to support and guide them. The various components such as rolling balls and raceways are subjected to high contact pressures in normal operating

TABLE 1.1: Properties of silicon nitride polycrystalline phases [Riedel and Chen, 2011]

property	α-Si_3N_4	β-Si_3N_4
Lattice parameter a[nm]	0.7748	0.7608
Lattice parameter c[nm]	0.5617	0.2911
Density [g.cm^{-3}]	3.184	3.18 7
Elastic modulus E [GPa]	340	310
Poisson's ratio ν	0.3	0.27
Hardness Hv [GPa]	21	16
Toughness K_c [MPa m$^{1/2}$]	2-3	6.8

conditions. Under some circumstances, higher pressures can result from the presence of inclusions or impurities issued from lubricant pollution for example. For these reasons, the damage in dense silicon nitride under contact conditions has been the subject of numerous studies over the last two decades. One can mention the work of Lee *et al.*[Lee et al., 1997] who processed materials with different grain sizes using hot pressing technique. By optimizing the applied temperature, fine, medium and coarse microstructures were obtained. The specimens were then indented using large tungsten spherical balls. The resulting surface and subsurface damage in the three materials is shown in FIG.1.13a. The fracture mode was observed under optical microscopy after gold coating. This mode is controlled by tensile part of the stress field and surface flaws which act as stress concentrators. The second mode was considered by means of bounded interface sectioning technique, we will detail this technique in the next chapter. The results for fine Si_3N_4, classical cone cracks were observed (FIG.1.13a). Several analytical attempts and finite element models have been proposed to simulate the downward propagation of such cracks and the influence of material parameters [Lawn, 1998].

With increasing the microstructure coarseness through the sequence fine $\rightarrow$ medium $\rightarrow$ coarse, surface cone cracks were gradually suppressed. In parallel, subsurface damage accumulation was clearly noticed. Indeed, it is well-known that large grains enhance the brittle materials resistance to long crack propagation because of several toughening mechanisms such as crack bridging and grain pull-outs [Hutchinson, 1989]. However, the resistance to short cracks significantly diminished. The second mode is controlled by the deviatoric shear component of the stress field hence the shape of the damaged area. Optical and scanning electron microscopy observation of the damaged area revealed the source of shear faults. They mainly consist of the weak points in the microstructure : grain twining and interphase boundary. Other studies have demonstrated the effect of the sintering aid used to process the material on the contact resistance of silicon nitride materials. In fact, it is experimentally observed that the damage accumulation strongly depend on the processing ways and boundary grain chemistry [Lee et al., 2005].

Based on semi-empirical calculation, Rhee *et al.*[Rhee et al., 2001] measured the critical loads for surface crack and subsurface damage initiation for a large set of brittle materials using tungsten indenters of different radii. The authors introduced the concept of transition radius r^*. As mentioned in their paper, the authors made strong assumption in their approach to derive the required relations which led to the overestimation of the r^* value especially in case of silicon nitride as it will be discussed in chapter 3.

Several models to account for strength degradation in silicon nitride because of contact damage were also proposed [Lawn et al., 1998]. It was demonstrated that in case of specimen with fine microstructure, the failure occurs from the surface ring cracks. However, in case of coarse microstructure the fracture had as origin the residual surface indent. Therefore, the bending strength is related to the subsurface damage because of microcracks coalescence, see FIG.1.13b. The damage modes were also investigated on silicon nitride when subjected to cyclic loading as shown in FIG.1.14. It is found that brittle modes (cracks) occurred for low number of cycles while quasi-plastic mode dominated for large number of cycle. This later mode led to initiation of radial cracks [Kim et al., 1999]. The authors also reported a significant influence of the number of cycles on the material strength. A model was also proposed afterwards to characterise the evolution of this property in brittle materials [Lee and Lawn, 1999].

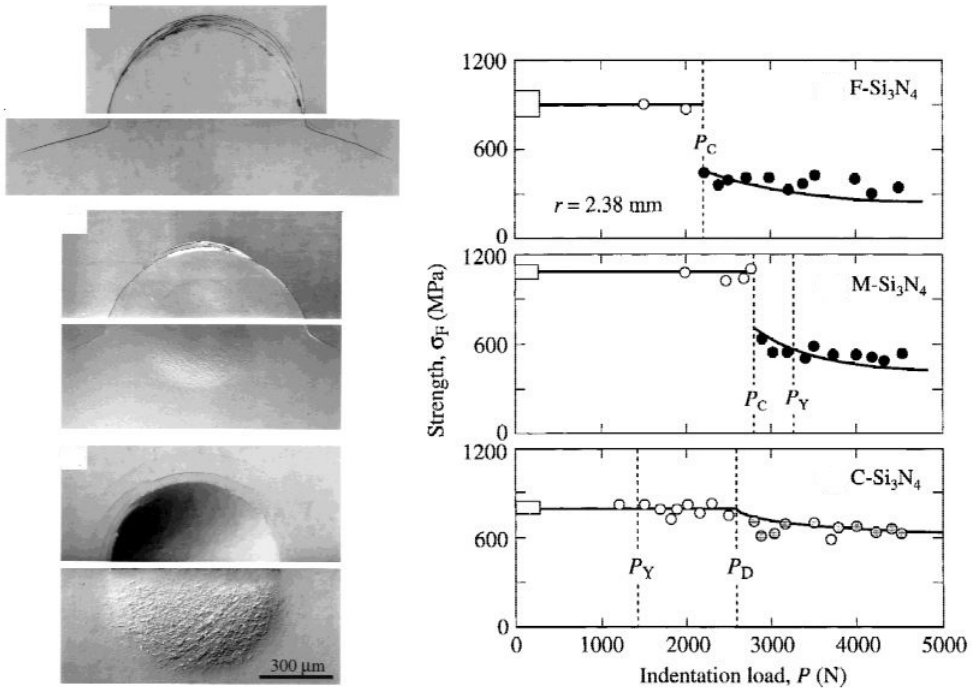

(a) Optical micrographs showing surface (top) and subsurface (bottom) damage dense silicon nitride after indentation with a 1.98 mm radius WC sphere at load P =5000 N

(b) Effect of contact damage on Si_3N_4 strength. Boxes are reference specimens, black symbols for failure of cone cracks while grey symbols represent failure from subsurface damage

FIGURE 1.13: Contact damage (a) and strength degradation in silicon nitride with different grain sizes (b) [Lawn, 1998]

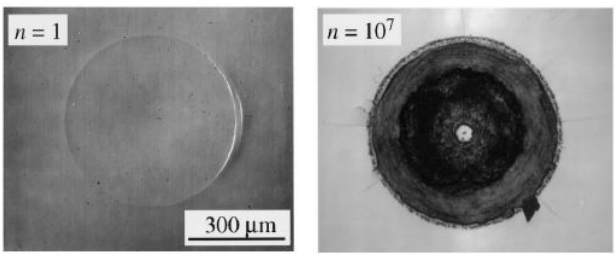

(a) single loading test (b) high number of loading tests

FIGURE 1.14: Contact damage in silicon nitride vertical loading (a) under cyclic loading under peak load P = 2200 N on WC sphere of 1.98 mm radius (b) [Lee and Lawn, 1999]

1.3.4 Damage in porous Si_3N_4 ceramics

The porosity is an integral part of ceramic components. In fact, most of the brittle materials including silicon nitride may contain two kinds of pores : (i) well−controlled and voluntarily introduced into the specimens by addition of a pore−forming agent to the starting powder or by decreasing the amount of sintering aid for applications such as catalyst supports, gas filters, thermal barrier coatings and biomaterials [Diaz and Hampshire, 2004, Yang et al., 2003], or (ii) uncontrolled and undesirable with random size distribution and morphology as shown in FIG.1.15a for commercial specimen and in FIG.1.15b for laboratory made one. The second type of porosity is mainly due to the materials processing conditions and can considerably impact the mechanical properties of the components [Rice, 1998], which in turns significantly reduces their lifetime [Hadfield, 1998].

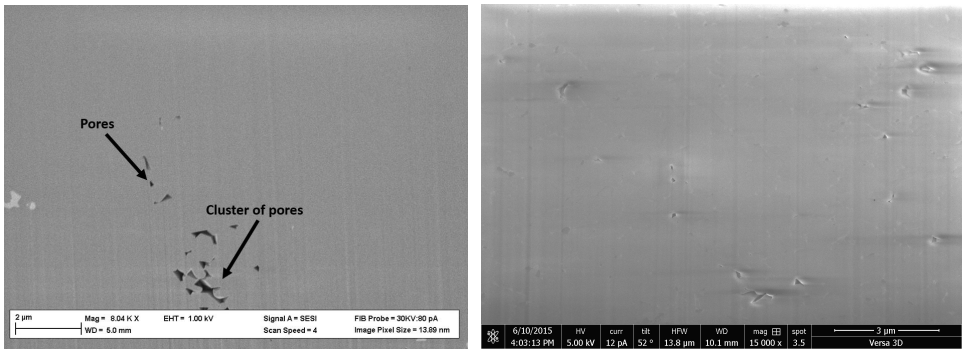

(a) Commercial silicon nitride (b) Processed silicon nitride

FIGURE 1.15: Subsurface porosities in commercial (a) and lab-scale silicon nitride observed on cross-sections performed by Focused Ion Beam (b)

Most of previous studies were interested only on the prediction of the porosity effect on the mechanical properties and specifically the Young's modulus and hardness. Several fitting models were proposed to take into account the porosity volume content in prediction of ceramic properties [Rice, 1998]. Nevertheless, contrary to alumina [Latella et al., 1997] and zirconia [Chintapalli et al., 2012] ceramics for example, it is surprising to find that only few works investigated the damage in porous silicon nitride. We can report here the work of She *et al.*[She et al., 2003] on highly porous silicon nitride, i.e. porosity volume content up to 37%. Using bounded interface sectioning technique, the authors observed the damage resulting from a dry contact of Tungsten ball of radius 1.67 mm over flat polished Si_3N_4 specimen, the results are shown in FIG.1.16. It was found that the porosity has a significant effect on the material response. Indeed, the surface cracks were suppressed and well defined half hemispherical damaged zone was noticed. This later mode is mainly due to pore collapse and grain microfracture under high compressive and shear stress fields. The damage intensified with increasing the applied load but still no evident crack was observed at the surface. The observations confirmed a transition from brittle to quasi-plastic behaviour of the porous specimens. This transition was evident on the indentation stress-strain curve that we will discuss in detail in Chapter 4. In addition, the authors performed 3-point bending tests on pre-indented specimens and found that the damage accumulation gradually decreases the fracture strength of Si_3N_4, see FIG.1.17.

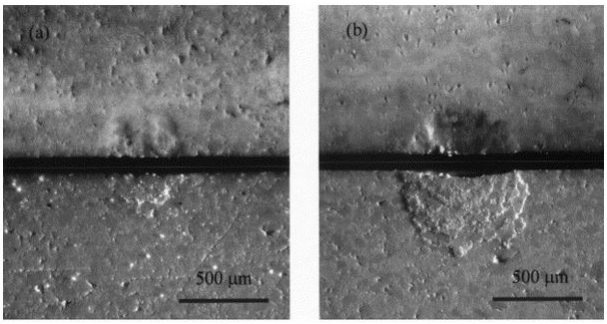

FIGURE 1.16: Surface damage (top) and subsurface damage (bottom) in highly porous silicon nitride (a) P = 250 N and (b) P = 500 N [She et al., 2003]

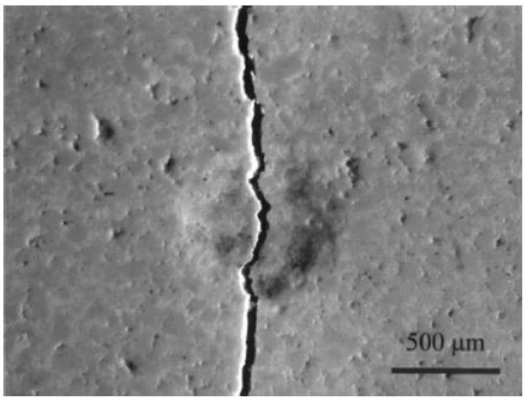

FIGURE 1.17: Fracture from residual surface impressions in highly porous silicon nitride under bending testing [She et al., 2003]

Figure 1.15a shows example of residual pores and cluster of pores in commercial rolling bearings while FIG.1.15b reveals pores in laboratory processed specimen. It should be noted that these porosities were observed at the subsurface level. In fact, it is interesting to highlight that no porosity was evident on the surface and a cross section had to be made. The industrial manufacturers rely on the surface observation before the validation of a component based on silicon nitride, therefore the initial microscopic damage can be missed. This damage may develop under high loading rate leading to premature catastrophic failure and then increasing the maintenance costs. To the best of the author's knowledge, contact damage mechanisms in silicon nitride with low porosity ($\leq$ 20 %) was not investigated in the literature, it is therefore necessary to devote a part of our work to this porosity range.

1.4 Inverse identification methods

1.4.1 Introduction

The fragile nature of ceramic materials characterized by a low tolerance to surface or bulk flaws acts as a hindrance to tensile-testing. We have mentioned that specimens with coarse microstructure are likely to exhibit quasi-ductile behaviour. Therefore, in case of brittle materials

alternative testing methods have to be used to model this mechanical behaviour. In other words, true stress-strain curves have to be determined. The first alternative consists of reducing the size of the requested volume, so the probability to meet a critical flaw which can cause an early failure is drastically decreased. In this sense, *in-situ* compression of pillars machined by ion beam was recently considered. In this technique, the specimens are of cylindrical shape 2-3 μm in diameter and 4-6 μm hight, FIG.1.18. These tests provide interesting insights regarding the local behaviour of the materials. However, as the sample size is still very small compared to the size of the grains, a representative elementary volume is not obtained. Thus, the values obtained are not representative of the macroscopic mechanical behaviour of the ceramic matyerial as shown for example in TAB.1.2 in case of silicon nitride. In addition, most of the machined the pillars inside the grains neglecting any effect from the boundary phase. Thus, the derivation of the mechanical behaviour at larger scale, imperative to predict the mechanical response of macroscopic products is not fully addressed yet.

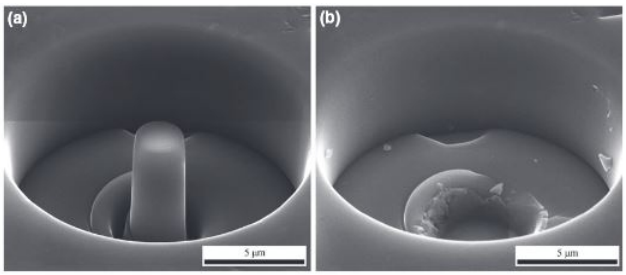

FIGURE 1.18: Micropillar compression in β-Si_3N_4 grains [Csanádi et al., 2015]

TABLE 1.2: Elastic modulus and yield stress of β Si_3N_4 grains [Csanádi et al., 2015]

Orientation	Elastic modulus (GPa)	Yield stress (GPa)
Prismatic	424 ±38	11.2 ± 0.1
Basal	664 ± 57	2.0 ± 0.2

The second possibility consists of taking advantage of a particular stress distribution that allows to test this class of materials without causing a premature rupture of the specimens. It turns out that a contact loading perfectly meets this condition. As previously reported, the stress is compressive under the contact site thereby allowing to observe different damage phenomena. In addition, except the specific case of so called "mystical materials", i.e. materials with different stress-strain curves but showing same indentation curve for different sharp indenters [Chen et al., 2007], two different materials have clearly distinct indentation curves. The approach requires to consider the problem in a inverse manner : from the effects one has to identify the causes, see FIG.1.19.

Indeed, the procedure requires to know well the geometrical aspects of the problem, to set the boundary conditions, apply the experimental loading path to the numerical model in order to be as close as possible to the experimental conditions. Most importantly, one must select a mechanical law that can best describe the response of materials to take into account the maximum of phenomena, while having the minimum of unknown parameters. Indeed, as the procedure requires finite

element calculations or iterative computations, it is better to minimize the number of searched coefficients.

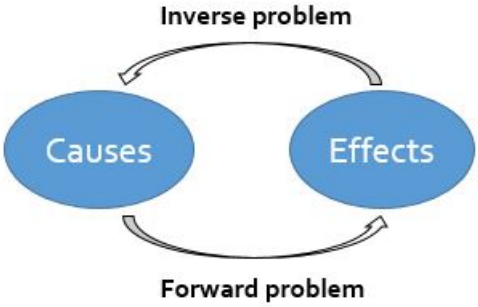

FIGURE 1.19: Forward problem and inverse problem [Buljak and Maier, 2011]

The described approach has been applied to a wide range of materials. One can mention here the work of Gu *et al.*for elastic-plastic graded materials [Gu et al., 2003], Constantinescu and Tardieu for viscoplastic [Constantinescu and Tardieu, 2001] materials. The human skin was also successfully characterised by Delalleau *et al.*[Delalleau et al., 2006, Delalleau et al., 2008].

1.4.2 Dimensional analysis

Dimensional analysis is based on the concept of representative strain, also called characteristic strain, introduced in early work for metals by Atkins and Tabor [Atkins and Tabor, 1965]. Because the strain field around a contact between an indenter and the surface is heteregenous, the cited authors introduced ε_r. In the general case, the value of the representative strain depends the tip geometry and loading conditions. In case of Vickers indenter, Tabor proposed a value of ε_r = 8% . This value is independent of the applied load because of the geometrical self-similarity characterizing sharp indenters.

The concept of representative strain was later extended by Dao *et al.*[Dao et al., 2001] who proposed a universal value of ε_r = 3.3%. The concept of representative strain makes independent the indentation loading curvature, the reduced modulus on the strain hardening in the power law model. In fact, this description of the material plastic behaviour reduces the number of unknown parameter to two : the plastic yield stress σ_y and strain hardening n.

$$\begin{cases} \sigma = E\varepsilon, & \text{if } \sigma \leq \sigma_y \\ \sigma = \sigma_y \, (1 + \dfrac{E}{\sigma_y}\varepsilon_p)^n & \text{if } \sigma \geq \sigma_y \end{cases} \tag{1.11}$$

For an elasotplastic material, the loading can be given as a function of the indenter elastic modulus E_i and Poisson's ratio ν_i of the indenter in addition the specimen elastic (E_s, ν_s) and plastic parameters (σ_y, n) :

$$P = P(h, E_s, \nu_s, E_i, \nu_i, \sigma_r, n) \tag{1.12}$$

Which can be rewritten in equivalent form using the reduced modulus E^* and representative stress σ_r :

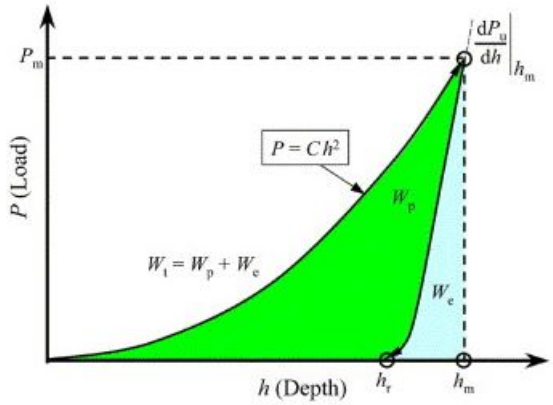

FIGURE 1.20: Typical load versus displacement curve for an elastoplastic material [Dao et al., 2001]

$$P = P(h, E^*, \sigma_r, n) \tag{1.13}$$

The objective is to derive the unknown parameters from the load versus displacement curve (FIG.1.20) obtained using instrumented indentation technique. The loading part of the curve is described using a power law with C the curvature coefficient. :

$$P = Ch^2 \tag{1.14}$$

All needed elements were introduced, the necessary mathematical tool is the Π-theorem which is based on the work of the French mathematician A. Vaschy and English physicist E. Buckingham [Buckingham, 1914]. Dimensionless variables are then introduced to reduce the number of unknown parameters.

Applying successively the Π-theorem allows finally to derive the following equations :

$$C = \frac{P}{h^2} = \sigma_r \Pi_1 \left(\frac{E^*}{\sigma_r}, n \right) \tag{1.15}$$

$$\left.\frac{dP}{dh}\right|_{h=h_m} = E^* h_m \Pi_2 \left(\frac{E^*}{\sigma_r}, n \right) \tag{1.16}$$

$$\frac{h}{h_m} = \Pi_3 \left(\frac{\sigma_r}{E^*}, n \right) \tag{1.17}$$

The values on the left-hand side of the equals sign in Eq.1.15, Eq.1.16 and Eq.1.17 can be experimentally measured. However for more precision, Dao and co-workers [Dao et al., 2001] performed finite element calculations for a large set of the elastic modulus E^*, yield σ_y and hardening parameter n, data fitting was then performed and formula for Π_1, Π_2 and Π_3 obtained.

This set of presented dimensional functions was afterwards extended by Chollacoop *et al.*[Chollacoop et al., 2003] to other indenter tip geometries (50°, 60°, 80° cones) and Bucaille *et al.*[Bucaille et al., 2003] to take into account the friction coefficient in the determination of the material parameters.

1.4.3 Uniqueness of the solution

We have seen that mechanically speaking, the set of unknown parameters is unique once the study material selected. Even in the case of reported mystical materials, identification procedure combined with measurement of the residual imprint allows to remove the doubt regarding the material considered. From a mathematical point of view, things are more complicated than they appear. Figure 1.21a shows the result of identification procedure from single conical indenter (fixed apex angle θ) using Eq.1.11 for highly elastic and highly plastic materials [Cheng and Cheng, 2004]. With fixed Young's modulus E and Poisson's ratio ν, one can observe that different sets of material parameters, the yield stress here Y and hardening coefficient n, lead to exactly the same load versus displacement curve.

Different approaches have been proposed to overcome this problem : combining inverse analysis on indentation curves with residual indent profile measurements [Tunvisut et al., 2002], or Vickers hardness and the amount of pile-up and sinking-in around sharp indenters [Mata and Alcala, 2003] and finally use of dual sharp indenters [Chollacoop et al., 2003].

According to Cheng and Cheng [Cheng and Cheng, 2004], the problem of uniqueness of the solution is not an issue in the specific case of spherical indenters. This advantage over the other indenters is due to the fact that the representative strain ε_r characterizing the indenter geometry and introduced in the previous section, is not of constant value. In fact, it depends on the indent and indenter diameter d and D, respectively :

$$\varepsilon_r = 0.2\frac{d}{D} \tag{1.18}$$

This dependence makes application of dimensional analysis to the spherical geometry very delicate. To work around this problem alternative approaches have been proposed. Some of them extended the earlier definition of the representative strain [Cao and Lu, 2004] while other approaches used neural networks [Huber and Tsakmakis, 1999, Tyulyukovskiy and Huber, 2006].

The authors mentioned that the major difficulty with the tip spherical is to obtain experimental proper results with minimal noise. This problem should be partially resolved thanks to the im-

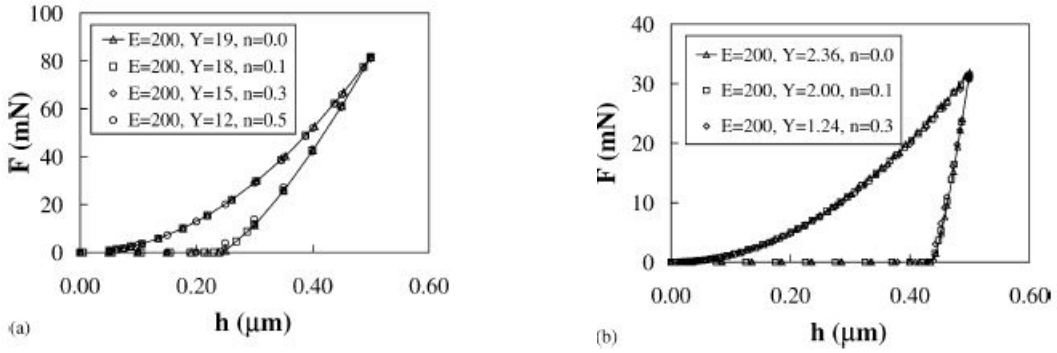

(a) Highly elastic material

(b) Highely plastic material

FIGURE 1.21: Identification procedure for highly elastic material using a conical indenter [Cheng and Cheng, 2004]

provements in nanoindentation instruments. In fact, the thermal drift is automatically corrected and the vibrations of the machine are made minimal. The only remaining problem is then the preparation of the samples.

1.4.4 Application to brittle materials

Regarding brittle hard materials, a different approach is generally considered to characterize the non−linear behaviour : a spherical indenter with a radius, R, mounted on a standard tensile machine is pressed on the polished surface of the specimen. Afterwards, the contact radius of the permanent indent, a, is measured under optical or Nomarski microscopy after gold coating. The indentation stress or mean pressure, p_0, is defined as the maximum applied load, P, divided by the contact area after complete unloading, i.e. $p_0 = P/\pi a^2$, and the indentation strain, a/R, as the contact radius a divided by the sphere radius R. In the elastic domain, p_0 is proportional to a/R [Johnson, 1987].

Using a set of indenters with various radius, a scatter-plot is obtained as shown in FIG.1.22a for silicon nitride with fine, medium and coarse microstructures. Because of the deviation from linearity, $p_0(a/R)$ relations were successfully used to derive the nonlinear mechanical behaviour of the brittle materials, see FIG.1.22b. In fact, Fischer Cripps and Lawn [Fischer-Cripps and Lawn, 1996] analysed the stress field in tough ceramics and proposed simple relations based on finite element calculations to determine the work hardening coefficient λ (this coefficient ranges between 0 and 1 : 0 for perfect plasticity without hardening and 1 for pure elasticity).

$$\begin{cases} \sigma = E\varepsilon, & \text{if } \sigma \leq Y \\ \sigma = Y + \lambda(E\varepsilon - Y) & \text{if } \sigma \geq Y \end{cases} \tag{1.19}$$

In this equation, the yield stress Y corresponding to the first plastic flow is experimentally determined. Indeed, by combining the critical shear stress criterion and Hertzian theory, it is possible to correlate the yield stress Y with the mean pressure of subsurface damage initiation. From the micromechanics point of view, it is found that the yield stress Y is related to the intrinsic shear stress of the different materials while λ is determined by the damage intensity Nl^3 where N is the density and l the size of the faults [Lawn, 1998].

However, for hard materials such as silicon nitride, the deviation from linearity in the indentation stress−strain curve is overestimated because of the flattening of the indenting spheres [Lee et al., 1997]. In fact, it is found that the yield stress and hardening coefficient of Tungsten carbide (WC) indenters are below the identified values of tested specimens. The deviation is accentuated because of the flattening of the indenters. In addition, the described technique requires optical measurements of the remaining contact radius and subsurface damage observation increasing the uncertainty of parameter values.

The indentation and inverse analysis were recently considered to characterise gypsum based materials with different porosity volume contents. The authors succeed to obtain Drucker-Prager constitutive model parameters based on spherical indentation and numerical simulations [Clément et al., 2013]. In case of dense ceramics, an approach was recently proposed by Luo et *al.* [Luo et al., 2014] to calculate the true $\sigma - \varepsilon$ curve of Si_2N_2O−Si_3N_4 composites based on nanoindentation tests using a Berkovich rounded tip and finite element calculations. However, because of the size

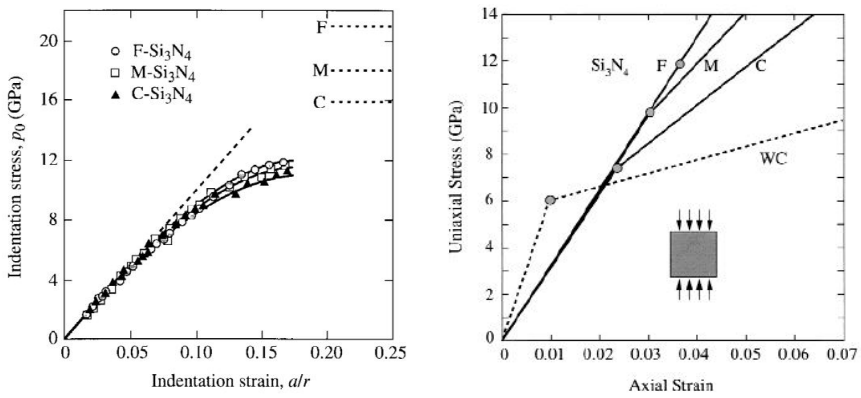

(a) Indentation stress - strain curves (b) Uniaxial stress - strain curves

FIGURE 1.22: Indentation and true stress-strain curves for fine (F), medium (M) and coarse (C) silicon nitride [Lee et al., 1997]

of the indenter considered by the authors, $R_{berk} \simeq 500$ nm, only ultra-fine-grained microstructures were tested and characterized.

1.5 Conclusions

In this chapter, we have presented without going into details some general aspects related to technical ceramics, their remarkable mechanical properties and listed some industrial application domains. We have focused on silicon nitride based materials as illustrating example. We discussed the damage in fully dense Si_3N_4 with different grain sizes and with high porosity volume content. A transition from brittle to quasi-plastic damage mode was experimentally demonstrated with increasing the microstructure coarseness. We presented the principle of inverse analysis to derive the material parameters from the load versus displacement curves. The problem of uniqueness of the solution using sharp indenters was also highlighted.

In light of this background, there is possibility to go further on the understanding of damage mechanisms in case of silicon nitride. This includes dense materials with different grain size and specimens containing a few percent of porosity volume content ($\leq$ 20 %). To the best of our knowledge, application of this inverse technique to silicon nitride has not been addressed yet, despite the fact it is conceivable to use the reverse analysis to obtain the material parameter of Si_3N_4. Studying the effect of porosity on the mechanical resistance of brittle materials to contact damage seems interesting.

Chapter 2

Materials and techniques

This second chapter is devoted to the presentation of the experimental procedure and numerical methods utilized in this work. It is divided into four sections : (i) the experimental conditions to process the materials of this study, their microstructural and mechanical characterization ; (ii) the investigation of the contact damage at the macroscopic and mesoscopic scale using diamond spheres with different radii ; (iii) the preparation of thin foils from the damaged area beneath the indents by Focused Ion Beam milling (FIB) and observation by Transmission Electron Microscopy (TEM) ; (iv) the instrumented indentation testing technique and experimental-numerical coupling to derive the yield stress σ_y and hardening coefficient K for the sintered materials.

Contents

2.1 Materials

2.1.1 Processing conditions

Commercially available high purity nanosized silicon nitride powder (SN-ESP, UBE Industries, Japan) with high α/β ratio ($\geq$ 95 %) was selected as starting material in this study. Powders with high α-phase content are known to lead to materials with better mechanical properties thanks to the β elongated grains resulting from the α to β phase transformation at high temperatures during sintering [Park et al., 1997]. The physical properties and composition of SN-ESP powder are summarized in TAB.2.1. In order to study the effect of an oxide additive additions on the grain sizes and mechanical behaviour, various amounts of yttrium oxide (Y_2O_3 : 99.99 % high purity, Wako Pure Chemical Industries, Japan) ranging from 1% to 5 % were added to the starting silicon nitride powder. This permits to easily control the microstructure of the materials, as it will be discussed in chapter 3 and 4. The batches were ball mixed as slurry in ethanol with alumina balls as media and finally dried in an electric oven at 80 °C.

TABLE 2.1: Physical properties of starting silicon nitride SN-ESP powder

Grade SN-ESP	**SSA** (BET) 6-8 m^2/g	**density**(g cm^{-3}) 3.19
Purity	O $\leq$ 2.0%	C $\leq$0.2 %, Cl $\leq$ 100ppm
	Cl $\leq$ 100ppm	Fe $\leq$100ppm,Al, Ca $\leq$ 50ppm
phase	α-phase crystal $\geq$ 95%	

Consolidation of the mixtures was carried out using SPS apparatus (SPS-1050, SPS Syntex, Inc., Japan) under vacuum conditions. In order to investigate the effect of the spark plasma processing conditions on the Si_3N_4 mechanical behaviour, batches containing 1 and 5% of Y_2O_3 were sintered at different final sintering temperatures T_f : 1600, 1650, 1700 and 1700°C. During the processing , the heating rates were as follows : 120°C/min from room temperature to 600°C, 100°C/min from 600°C to 1600°C, then 20°C/min from 1600°C to the suitable temperature T_f. A typical example of sintering cycle until 1700 °C is presented in FIG.2.1. All the processing conditions considered in this work are summarized in TAB.2.2.

Finally, to investigate the effect of the porosity content on the microstructure, mechanical properties and contact damage, the maximum applied pressure during the sintering process was also decreased from 40 MPa to 20 then to 10 MPa for a selected set of batches (A, B and C, respectively). Note that in addition to pressure, the amount of yttrium oxide was decreased to 1% for specimen C in order to increase further the porosity volume fraction.

2.1.2 Microstructural characterization

The bulk densities ρ of the sintered disks were measured using Archimedes method with distilled water as the immersion medium according to ASTM-C20 standard [ASTM, 1981]. The relative density reported is the experimental density ρ divided by the theoretical one ρ_{the}. A rough

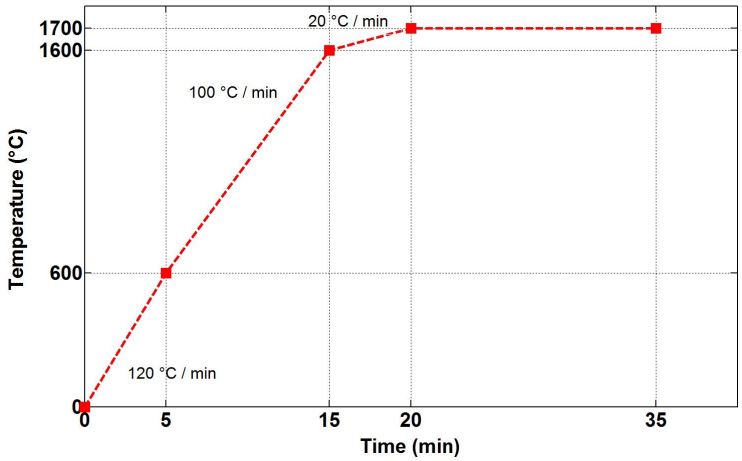

FIGURE 2.1: Sintering temperature cycle

approximation of ρ_{the} is calculated using the mixture law from the theoretical densities of the starting $\alpha-Si_3N_4$ (3.19 g cm^{-3}) and Y_2O_3 (4.47 g cm^{-3}) powders. This is due to the fact that no change in the phase composition was taken into account during the calculation of ρ_{the}. However, because both silicon nitride phases have very similar bulk densities, the induced error remained acceptable.

Five measurements were performed for each material to calculate the average value and the standard deviation.

The top surfaces of the prepared samples were polished on progressively finer SiC disks then fi-

TABLE 2.2: List of the sintered materials and corresponding processing conditions

Material	Yttria,wt %	Temperature (°C)	Time (min)	Pressure (MPa)
Y1T1600	1	1600	15	40
Y1T1650	1	1650	15	40
Y1T1700	1	1700	15	40
Y2T1700	2	1700	15	40
Y3T1700	3	1700	15	40
Y4T1700	4	1700	15	40
Y5T1700 (A)	5	1700	15	40
Y5T1650	5	1650	15	40
B	5	1700	15	20
C	1	1700	15	10

nal polishing performed using diamond pastes (3 µm, 1 µm and 1/4 µm). Final roughness of about 0.1 µm was evaluated using scratch tests under low applied normal loads on Agilent nanoindentation apparatus. After polishing, chemical attacks were conducted using sodium hydroxide solution (NaOH) at 500°C (FM27, Yamato Scientific Co, Japan) to highlight the grain structures. Etching time was optimised for each considered material. After etching, the samples were carbon coated to avoid charge-up during image acquisition. The materials were then observed under scanning electron microscopy (SEM 7500F, JEOL, Japan). Additional electron backscattering diffraction observations (EBSD, TSL, USA and SEM 8503F, JEOL, Japan) were also performed to examine different crystallographic orientations of the grains. Finally, the different crystalline phases for each processing condition set were examined by X-ray diffraction (XRD) measurements with Cu K_α radiation at 40kV−40mA (Ultima IV, Rigaku). Continuous scanning was performed from 10 to 100° with an angle increment of 0.02°. The acquired data was analysed using Jade 5.0 and Topas softwares for Rietveld refinement. Rietveld refinement was performed to determine precisely the α/β ratio, considering some textural effects.

2.1.3 Mechanical properties

2.1.3.1 E, H and flexural strength

The elastic properties were calculated on SPSed disks using standard ultrasonic method (TM506A, Hitachi). First, the thickness of the disks was measured with an accuracy of a micron. Young's modulus and Poisson's ratio values are then given by following relations :

$$E = \rho \frac{V_L^2(1+\nu)(1-2\nu)}{1-\nu} \tag{2.1}$$

$$\nu = \frac{1-2(V_T/V_L)^2}{2-2(V_T/V_L)} \quad , \tag{2.2}$$

In eq. 2.1, V_T is the shear (transverse) velocity, V_L the longitudinal velocity of the waves and ρ the bulk density of the tested materials.

Concerning the hardness of the sintered materials, it was measured with a Vickers diamond indenter which is a four sided pyramidal tip. The tests were performed on well polished surfaces using a Buehler Micromet 5104 machine. After complete unloading, the final imprints were observed under optical objectives attached to the testing machine at magnification of $\times 10$ and $\times 40$. Primary tests were completed to investigate load and dwell time effects on hardness values, then they were set to 19.6 N (2kgf) and 15 s, respectively. A serie of ten tests was performed for each material in order to improve the confidence in the results. Indent locations were spaced by at least five times the diagonal length to avoid any mutual influence.

Flexural strength σ_r values were measured at room temperature on standard Instron 5965 machine. Three point-bending tests were performed with an outer span L= 20 mm. The disk-shaped specimens measuring 30 mm in diameter and 3 mm in thickness were cut using a diamond saw into rectangular specimens with depth b=2 mm and width d= 3 mm. Each specimen was ground with 600 diamond disc and edges chamfered to eliminate machining flaws that can be precursor fracture origins. In order to obtain a representative value, five bars were tested for each material of TAB.2.2 at cross-head speed of 0.05 mm/min.

The bending strength value σ_r was then calculated using the standard formula :

$$\sigma_r = \frac{3FL}{2bd^2} \tag{2.3}$$

Where F is the maximum applied load.

2.1.3.2 Fracture toughness

The measurement of the fracture toughness K_C (resistance to crack propagation) of the obtained materials was performed by means of Vickers Indentation Fracture technique (VIF). Contrary to Single Edge Notched Beam (SENB) or Single Edge Pre-cracked Beam (SEPB), VIF has the advantage of being simple to set up without any special preparation of the tested samples and can be performed on small samples as it is the case of SPS disks. The method is often disputed [Quinn and Bradt, 2007] to give an exact, relevant measure of the toughness but it was used here mainly for comparison purpose.

Broadly speaking, this approach relies the applied load P, the elastic modulus E, the hardness H, and the geometrical parameters of the residual surface impression, i.e. half diagonal length a and crack extension from the corners of the imprints to the material toughness K_C. The crack system developing under Vickers indentation is shown in FIG.2.2.

Indentation tests were performed on the polished surface of the specimen using diamond Vickers indenter on standard hardness testing machine (Buehler Micromet 5104). The cracks and diagonal lengths were measured by optical microscope (VK100, Keyence) with a resolution of 0.1µm. Numerous models exist in the literature based on the pioneer work of Evans and Charles [Evans and Charles, 1976]. Because the derivation of exact analytical solution for the crack system seems out of reach, most of proposed equations are based on experimental data fitting. In case of silicon nitride based materials, two semi-analytical models are usually used :

Niihara model [Niihara, 1983] for Palmqvist system ($l/a < 2.5$) under an applied load of 19.6 N (2 kgf) :

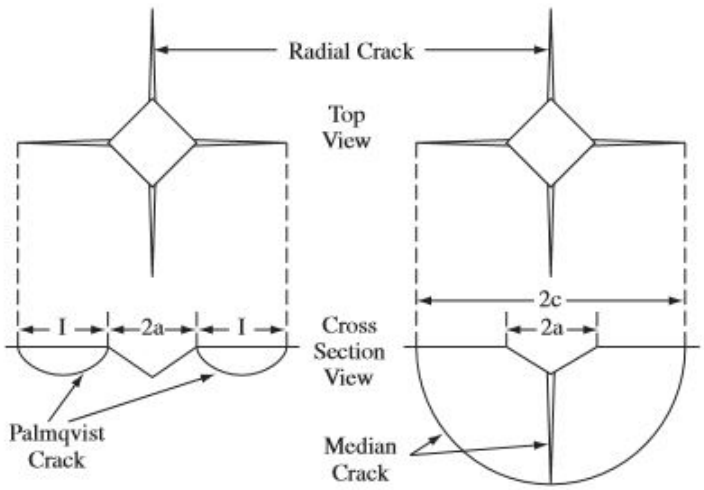

FIGURE 2.2: Crack formation by Vickers indentation [Strecker et al., 2005]

$$(\phi K_C/Ha^{1/2})(H/E\phi)^{2/5} = 0.035(\frac{l}{a})^{-3/2} \tag{2.4}$$

where ϕ is the constraint factor (= $H/\sigma_y \simeq 3$).

For median cracks ($c/a > 2.5$), a load of 196 N (20 kgf) was applied and K_C given by the Miyoshi model [Miyoshi, 1985] (Japanese Industrial Standard) :

$$K_C = 0.018(\frac{E}{H})^{1/2}(\frac{P}{l^{3/2}}) \tag{2.5}$$

To highlight potential mechanisms of reinforcement, the crack paths after indentation were observed in detail under electron microscopy (SEM 7500F, JEOL, Japan).

2.2 Contact damage

2.2.1 Macroscopic scale

The usual procedure to study the subsurface contact damage under single or cycling loading in brittle materials is the bonded-interface sectioning (BIS) technique. Here, we recall a brief description and principle derivations, more details about this technique are given in reference [Guiberteau et al., 1994]. The approach consists of two polished surfaces clamped face to face using a thin layer of strong adhesive (FIG.2.3). The specimens are then mounted on a flat rigid substrate using a thin layer of commercial crystalbond to lock any rigid body displacement.

Indentation tests are afterwards symmetrically made on the specimen polished top surface using hard balls under cross−head speed of 0.05 mm/min (Model 5965, Instron). After complete unloading the adhesive is dissolved to separate the two halves, their surfaces cleaned with acetone. They are then dried and finally gold coated to observe the damage under optical or electronic microscopy.

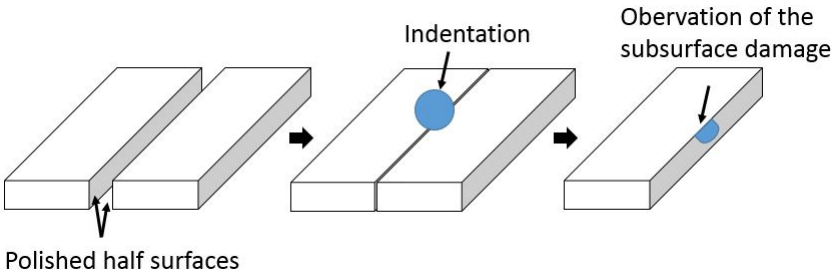

FIGURE 2.3: Schematic illustration of the bonded-interface technique

2.2.2 Mesoscopic scale

The method described in the previous section is easily implemented and pertinent in case of large contacts (few millimetres diameter). However, the use of this technique for very small indents (few micrometers diameter) is complicated and may affect the observed damage (stress concentration on the edge flaws, asymmetric loading ..). Another observation approach is then needed to deal with these problems due to the contact area reduced size. Here, examination of the damage

below the indents was performed using focused ion beam cross−sectioning technique (Versa 3D Dual Beam, FEI company). It consists of three successive steps : firstly, one micrometer carbon layer deposition is made on the top surface of the indent to prevent etching during milling. The second step is digging using a focused beam of accelerated gallium ions (Ga^+) beneath the contact zone to the desired depth. A first approximation of this depth is given by the Hertz theory [Johnson, 1987]. The interaction of the incident beam (electron beam or ion beam) generates secondary electrons and secondary ions which can be collected to simultaneously perform micrograph acquisition within the zone of interest (SEM or SIM images). This latter step can provide abundant information about the local damage mechanisms at high resolution.

Intermediate cleaning steps at moderate electron beam with current up to 3 nA were also made to minimize ion/surface interactions. The advantage of using the described technique is the ability to observe beneath small indents with a minimum influence on the damaged zone when compared to standard polishing or cutting techniques [Uchic et al., 2007, Zaefferer et al., 2008]. This difference is due to the fact that no mechanical stress is applied on the sample. In addition, machining and observation steps are simultaneously performed in the vacuum chamber. 3D reconstruction of the damaged area can be also obtained (slice & view technique).

Because of the low conductivity coefficient and brittle nature of the silicon nitride materials, it is necessary to optimize the experimental conditions (acceleration voltage, current, exposure time) in order to minimize charge-up and possible damage artifacts.

With this aim in mind, preliminary work was performed on Si_3N_4 specimens free of indents. It is important to report that no microcracking or any other damage mechanisms were observed. Therefore, we can clearly assert that the damage results only from the mechanical load applied to the top surface of the specimens.

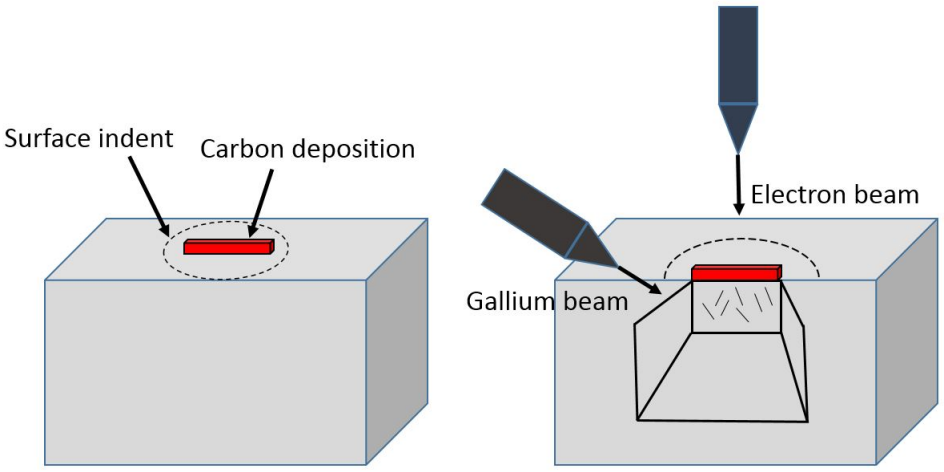

FIGURE 2.4: Schematic illustration of the focused ion beam sectioning technique

2.3 TEM observations

Transmission Electron Microscopy (TEM) is a very versatile and powerful technique for high resolution observation (nanometric scale) to highlight the nature of the subsurface contact damage. In case of material science specimens, the use of Annular Dark-Field (ADF), High Resolution Electron Microscopy (HREM) and High Angle Annular Dark Field (HAADF) modes are feasible.

Having said that, the challenge consists of preparing specimens as thin as possible (typical required thickness is about 100 nm) to enable the penetration of analysing electron beam. This difficulty is accentuated by the hard brittle behaviour of the materials considered in this study. Usually for the sake of time and resources savings, conventional H-bar technique (FIG.2.5) is commonly used. It requires initial preparation of the specimen. In fact, tripod grinding and polishing up to 30-20 microns thickness using diamond films is performed, then the microchip is mounted to a special support and moved to a FIB instrument. Final thinning to the suitable thickness is then performed using ion beam.

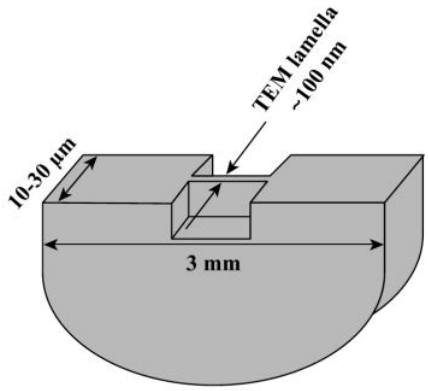

FIGURE 2.5: H bar sample using FIB [Schlesinger and Paunovic, 2011]

Here we use an alternative method referred to as *in situ* lift-out technique requiring no specimen preparation. In continuity of the damage observation presented in section 2.2.2, cross-sectioning of the opposite side is made to machine thin lamellas from the damaged area under the residual impressions, an example is given in FIG.2.6. Here lies another advantage of the FIB technique : high spatial accuracy (up to 50 nm) of target selection. The procedure is detailed in annex A. We sum up below the main steps of the TEM thin foil machining. One should add that a part of the preparation can be automated to get a better reproducibility and minimize the work time spent by the operator.

A) Surface impression left after unloading is marked and a carbon layer is deposited to prevent etching. The suitable dimensions of specimen are about 20 µm length × 20 µm width × 1 µm thickness. The bottom and edges of the lamella are cut.

B) A manipulator probe is introduced in the chamber and linked to the lamella, then the last specimen-bulk body connection is removed

C) The specimen is glued to a TEM grid using carbon deposition and its connection with the probe is cut.

D) The sample is tilted and final thinning under acceleration voltage of 5kv and beam current of 16 pA with an incidence angle of $\pm 2^{\circ}$. The final specimen dimensions are about : 20 µm

length × 20 µm width × 100 nm thickness. The sample is then introduced into the TEM instrument (Titan3^{TM}G2 60-300, FEI campany) for the observations.

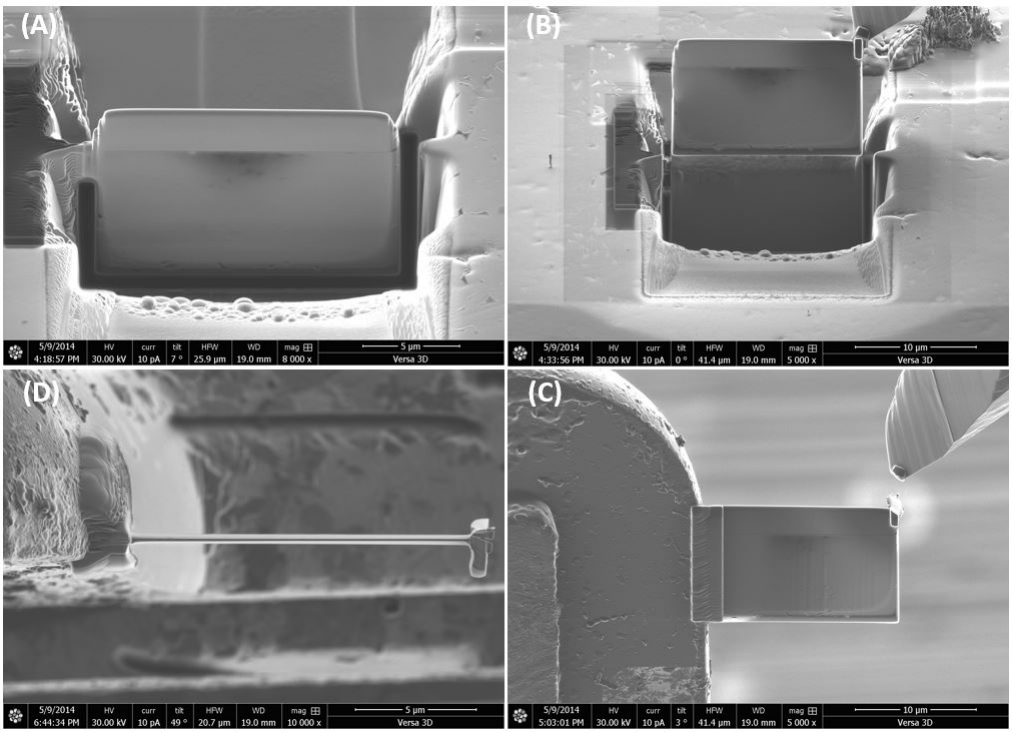

FIGURE 2.6: Transmission Electron Microscopy thin foils preparation from the damaged area (a) edges and bottom cutting (b) lift-out (c) TEM grid (d) rotation and final thinning

2.4 Indentation technique

2.4.1 Indentation stress-strain curves

The indentation testing is one of the most popular techniques used to characterize the mechanical behaviour of brittle materials. In fact, the indentation stress or mean pressure, p_0, defined as the ratio between the applied load P and the contact area S, i.e, $p_0 = P/\pi a^2$ can be plotted versus the indentation strain, a/R, where a and R represent the contact and sphere radius, respectively. In the elastic domain, Hertz (1881) have demonstrated that p_0 is proportional to a/R [Hertz, 1881]. If a deviation from this linear relation occurs, the first point corresponds to the yield stress Y. Combining the critical shear stress criterion ($\tau_c \simeq 0.5$ Y) and Hertz theory for elastic contacts ($\tau_m \simeq 0.47$ p_0) provides a first approximation value for the yield point, $p_0 = 1.1$ Y [Guiberteau et al., 1994].

Two diamond spheres of radii $R_1 = 0.2$ mm and $R_2 = 1$ mm were used to produce indents at the polished surfaces of the sintered materials. An assembly system was specially machined to attach the tip on an Instron 5965 standard tensile testing machine. After complete unloading, the indented surfaces were gold coated for 60 seconds then observed under optical microscopy at ×10, 20 and 50 magnification for an accurate measurement of the contact radius a. Because of limited number

of indenters, one expect the deformation range a/R to be limited. However, the general trend could be obtained.

For comparison purpose, 3D scanning of the residual surface depressions was performed and the indent profile along a symmetry axis was extracted, see FIG.2.7.

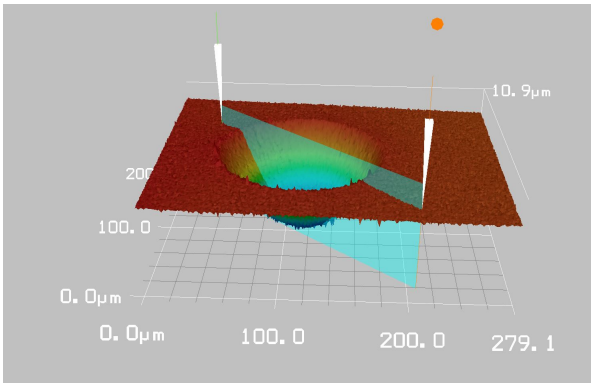

FIGURE 2.7: 3D indent profile (keyence VK-100)

2.4.2 Instrumented indentation technique

To assess the local mechanical behaviour of a large variety of materials including hard ceramics, instrumented indentation technique is generally used [Hay and Pharr, 2000, Doerner and Nix, 1988]. It consist of a hard indenter of a given geometry is pushed into a flat well−polished surface. The applied load, P, and the vertical displacement of the indenter, h, are simultaneously recorded during testing to obtain a $P-h$ curve. A typical profile of this latter one is shown in FIG.2.8. Standard configuration of the instruments commercially available is presented in FIG.2.9. The force is applied through electromagnetic actuation transducers. High load module available on some devices allows working with maximum loads up to 10 N. The indenter displacement has a resolution of few nanometers while the applied load resolution is of few millinewtons. The samples are mounted on a vibration isolator which reduces the noise and increases the accuracy of the measurements. This highlights the importance of measuring experimentally the true tip radius to obtain accurate values of E and H. .

Oliver and Pharr method [G.M Pharr, 1992] improved the earlier work of Downer and Nix [Doerner and Nix, 1986] to capture the Young's modulus and surface hardness from the unloading part of the measured curves assumed to be purely elastic. We recall thereafter the main relations without getting into too much details. The interested reader can easily refer to the articles cited a bit earlier.

$$E_r = \frac{\sqrt{(\pi)}}{2\beta}\frac{S}{\sqrt{A(h_c)}} \tag{2.6}$$

$$H = \frac{P_{max}}{A(h_c)} \tag{2.7}$$

Equation (2.6) relates the contact stiffness S, the reduced modulus E_r and the projected area A, while Eq.(2.7) permits to derive the hardness H to the applied load P_{max} and again, the projected

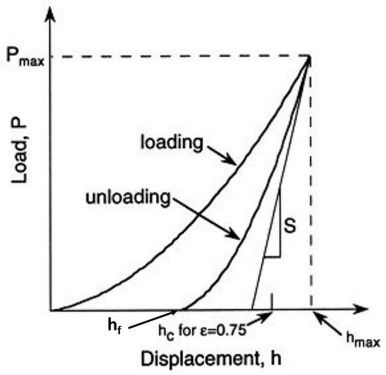

FIGURE 2.8: Indentation technique

area A. β is a geometrical correction factor related to the type of the indenter (β = 1 for a spherical shape). One can note that the Poisson's ratio is not calculated in indentation technique, a value of 0.3 is commonly used. For better accuracy, we will use the value determined by the ultrasonic measurements.

The determination of the contact area A(h_c) between the indenter and the specimen is critical to obtain the desired parameters. A geometrical analysis permitted to obtain A for a spherical indenter :

$$A(h_c) = \pi(2Rh_c - h_c^2) \tag{2.8}$$

With h_c derived from the maximum of the indenter displacement and loads, h_{max} and P_{max}, respectively,

$$h_c = h_{max} - \varepsilon\frac{P_{max}}{S} \tag{2.9}$$

Again ε is a geometric parameter related to the indenter geometry, a value of 0.72 was obtained in

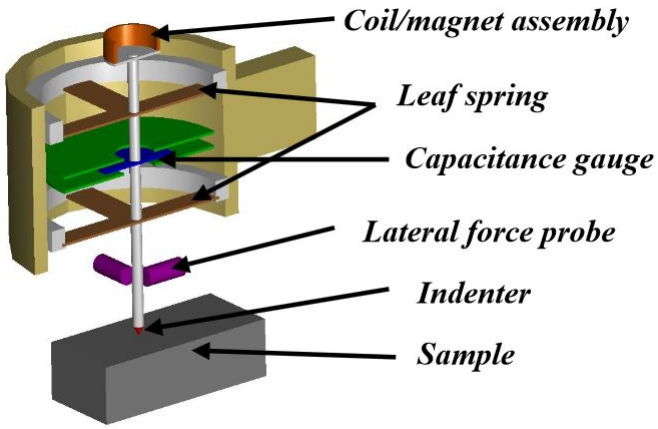

FIGURE 2.9: Schematic diagram of the actuating and sensing mechanisms of the Nano Indenter G200

case of spherical tip [G.M Pharr, 1992].

The previous set of equations allows to obtain a single value for E and H at the peak indentation load, i.e, for P =P_{max}. With the recent developments in the measuring instruments, a CSM (Continuous Stiffness Measurement) technique was developed. It consists of superimposing a small harmonic oscillation to the main applied load and continuously measure the contact stiffness S. The evolution of elastic modulus and hardness depending on the penetration depth is obtained, see for example FIG.2.10. It allows to obtain a profile for specimen mechanical properties along vertical axis z and therefore more representative average values and evaluate the influence of the surface roughness.

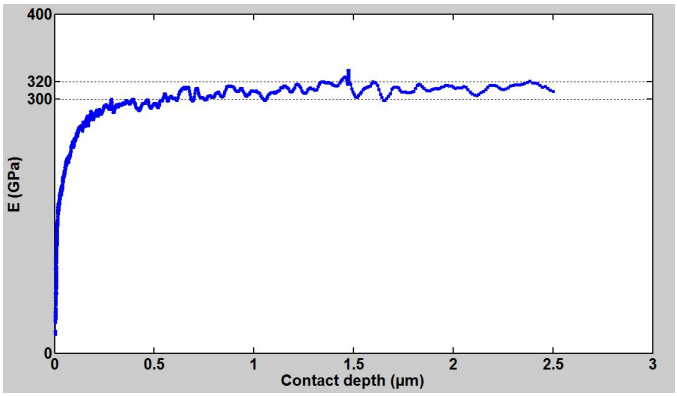

FIGURE 2.10: Evolution of Young's modulus with contact depth for dense Si_3N_4

A spherical diamond tip of radius of 50 µm manufactured by Synton-MDP (Switzerland) was utilized. The selection of indenter geometry is driven by the parameters which one aims to identify from the experimental data.

This issue is made easier by the concept of representative strain ε_r introduced by Tabor [Tabor, 1996]. The Berkovich and Vickers tips are standard products and can be machined more precisely. However, they are characterized by constant representative strain

$$\varepsilon_r = 0.2 cot\theta \tag{2.10}$$

Where θ is the half apex angle of the equivalent conical indenter (70.3 and 68°, respectively). In case of spherical shape, ε_r varies with increasing the contact radius a making possible a smooth transition from an elastic to plastic regime :

$$\varepsilon_r = 0.2a/R \tag{2.11}$$

The use of diamond material for the tip is imposed by the high hardness of ceramic materials to minimize the tip deformation. Indentation experiments were conducted using Agilent Nano Indenter G200 system. All the tests were performed under constant strain rate of 0.05 s^{-1} and allowed thermal drift rate of 0.05 nm s^{-1}. To obtain a representative curves, arrays of 5 by 5 with an inter-indentation spacing of 100 microns along the x and y directions were performed or each material, see FIG.2.11. The initial distance between the tip and the specimen surface is 1000 nm and the surface approach velocity was fixed to 10 $nm.^{-1}$. The spherical tip used in this study was observed with a high resolution digital microscope (KH-7700, Hirox) for a 3D reconstruction of

the tip profile. No deviation from the spherical shape or surface defects were noticed. However, it is found that the true tip radius is 42 µm. The difference between this "true" value and one proposed by the manufacturer is due to the difficulty of polishing a hard anisotropic diamond crystal into spherical shape.

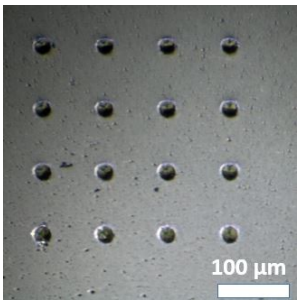

FIGURE 2.11: Indents made by spherical tip

The calibration of the indentation system was performed by indenting a reference material with well−known elastic modulus and hardness. Standard silica specimen (E = 69−72 GPa, ν=0.17 and H=10 GPa) was used in this work to calibrate the tip.

2.4.3 Finite Element Model

In order to perform the indentation test simulations, an axisymmetric two-dimensional Finite Element Model (FEM) was constructed under the commercial package Abaqus v6.11 [Simulia, 2011]. The model is composed of a diamond (E_i =1140 GPa, ν_i=0.07) coni−spherical indenter with a radius R of 42 µm and a large homogeneous domain, see FIG.2.12. The indenter tip was assumed to be purely elastic while the specimen was considered as an elastoplastic material with an isotropic hardening.

The contact between the indenter and the sample was assumed to be frictionless as no influence of friction coefficient was noticed on the global response of the model within the load range considered in the nonindentation tests (0 -10 Newton) as shown in FIG.2.13.

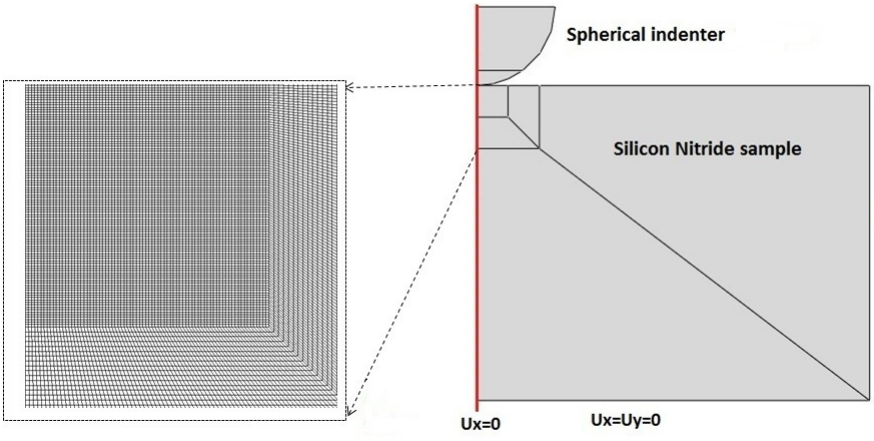

FIGURE 2.12: Abaqus model for a Hertzian contact of a sphere indenter on a flat ceramic specimen

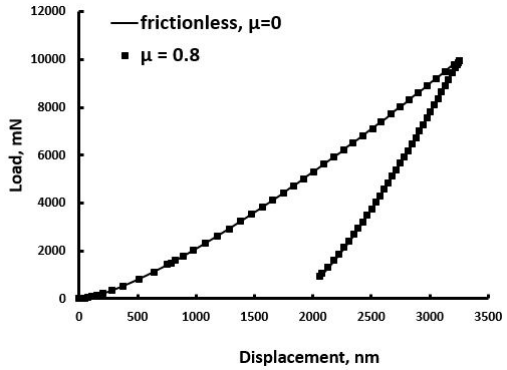

FIGURE 2.13: Influence of the friction coefficient on the load-displacement curve for an elasto-plastic material

Bilinear four-node axisymmetric elements (CAX4R) with reduced integration and hourglass control were used to mesh the model. Fine meshing was considered in the contact area to ensure the convergence of the contact simulation and meshes gradually increasing coarseness further from the contact zone were generated.

In order to optimize the computation time, the sensitivity to the mesh refinement was studied. It was found that 5000 elements in the contact zone are enough to reproduce well the indentation response of model within a large interval of the penetration depth. The Von Mises yield criterion (J_2 flow theory of plasticity) is assumed in all the numerical part of the study to represent the yield surface.

$$J_2 = \frac{1}{6}[(\sigma_1 - \sigma_1)^2 + (\sigma_2 - \sigma_3)^2 + (\sigma_1 - \sigma_3)^2] \tag{2.12}$$

Where σ_1, σ_2 and σ_3 are the principal stresses. This criterion is preferred over that of Tresca and maximum reduced stress criterion because of its easier implementation in the numerical approaches. The last criterion has the disadvantage of having discontinuous normals on the corners of the yield surface. However, it is well admitted that the predictions obtained using the three models are very similar [Johnson, 1987].

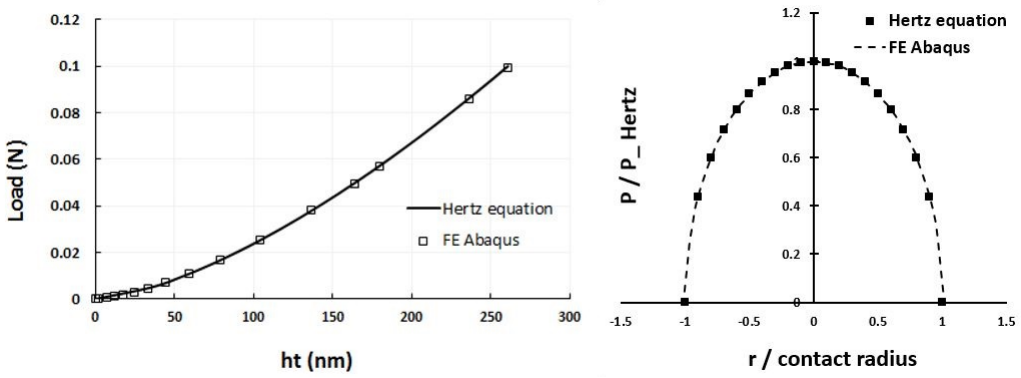

FIGURE 2.14: Comparison between Hertz equations and abaqus model

2.4.4 Uniaxial stress-strain curves

2.4.5 Minimization approach

The objective of this approach is to minimize the error between the experimental data and numerical data from finite element simulations. The minimization procedure aims to find the set of material parameters $\boldsymbol{p}$ which better describe the mechanical response of the tested specimen.

We define F_2^{exp} and F_2^{FE} as the numerical and experimental force of the model under the same imposed vertical displacement, the gap is then :

$$\chi^2 = \sum_{i=1}^{n} [\frac{F_2^{exp} - F_2(p)^{FE}}{w_i}]^2 \tag{2.13}$$

Expanding χ^2 by its Taylor series to the second order about the initial value of $\boldsymbol{p}_0$ selected as a starting point for the identification process,

$$\chi^2(\boldsymbol{p}_0 + \Delta\boldsymbol{p}) = \chi^2(\boldsymbol{p}_0) + \mathbf{g}^T \Delta\boldsymbol{p} + \frac{1}{2}\Delta\boldsymbol{p}^T H \Delta\boldsymbol{p} \tag{2.14}$$

Where $\boldsymbol{g}$ is the gradient of χ^2 with respect to $\boldsymbol{p}$ and $\mathbf{H}$ the Hessian matrix calculated as follows :

$$\begin{aligned} g_i &= \frac{\partial \chi^2}{\partial p_i} \qquad \text{for } i = 1, ...n \\ H_{ij} &= \frac{\partial^2 \chi^2}{\partial p_i \partial p_j} \quad \text{for } i, j = 1, ..n \end{aligned} \tag{2.15}$$

The minimization of Eq.(2.14) is obtained when its gradient with respect to $\boldsymbol{p}$ vanishes. This gives us the equation enabling to calculation of the new increment for the searched parameters :

$$\Delta\boldsymbol{p} = -\mathbf{H}^{-1}\mathbf{g} \tag{2.16}$$

And thus the input values at iteration $i+1$ are obtained : $\boldsymbol{p}_{i+1} = \boldsymbol{p}_i + \Delta\boldsymbol{p}$. These operations are repeated until the stopping condition is satisfied, i.e. $\chi^2 < \epsilon$ with ϵ set according to the desired accuracy on the constitutive parameters. The study showed that ϵ = 1 % is a good compromise between the computation time needed for the iterative process and the error on the parameters.

Equation (2.16) shows that the computation of each increment requires determining the Hessian matrix, which is not always an easy task. In fact, the direct inversion of $\mathbf{H}$ is often infeasible or can be numerically costly in terms of computation time. It is therefore necessary to find a satisfactory approximation to avoid any explicit calculation. It turns out that by definition, χ^2 is the sum of positive terms. Thus, it can be re-rewritten as follows :

$$\chi^2 = \frac{1}{2}\sum_{m=1}^{n} f_i^2 = \frac{1}{2}\mathbf{f}^T\mathbf{f} \tag{2.17}$$

with **f = s - e** where **s** and **e** are the experimental data from the indentation tests and numerical model output, respectively. One can use Gauss-Newton technique to obtain an approximation for $\mathbf{H}$. In fact, let's $\mathbf{J}$ be the Jacobian matrix of $\mathbf{f}$, it is found that the Hessian matrix can be approximated by Gauss-Newton matrix $\mathbf{G}$:

$$\mathbf{H} \simeq \mathbf{G} = \mathbf{J}^T\mathbf{J}. \tag{2.18}$$

Because the matrix **H** can be poorly conditioned, Levenberg-Marquardt algorithm [Levenberg, 1944, Marquardt, 1963] uses a damping factor λ (adjusted at every iteration) modifying Eq.(2.16) to recalculate the parameter increment :

$$\Delta \boldsymbol{p} = -[\mathbf{H} + \lambda I]^{-1}\mathbf{g} \tag{2.19}$$

Finally, to take into account the boundary constraints of the considered material parameter, the cost function is penalized.

2.4.5.1 Validation

In this study, the indented ceramic specimens are considered to behave as elastoplastic materials. Hooke's law describes the elastic part of the mechanical response while a bilinear law was used to describe the plastic regime :

$$\begin{cases} \sigma = E\varepsilon, & \text{if } \sigma \leq \sigma_y \\ \sigma = \sigma_y + K\varepsilon_p & \text{if } \sigma \geq \sigma_y \end{cases} \tag{2.20}$$

The total strain consists of two parts,

$$\varepsilon = \varepsilon_e + \varepsilon_p \tag{2.21}$$

where ε_e and ε_p are the elastic (reversible) and plastic (irreversible) parts of the total strain. The unknown material parameters in Eq.2.20 are the uniaxial yield stress σ_y and the coefficient K describing possible hardening of the specimens. To test the consistency of the method, elastic modulus E was also considered as unknown in the identification procedure. The values obtained for this parameter are compared to the experimentally measured ones.

A flow chart of the numerical algorithm considered in this study is presented FIG.2.16. It was developed by F. Richard [Richard, 1999] for application on the reliability of composite materials. First, the searched material parameters are initialized and first numerical simulation using the Abaqus model described before is made. The gap between the numerical and experimental load versus displacement curves is then calculated. Levemberg-Marquart is applied to get best descent direction and the parameters are updated. This operation is repeated until suitable agreement between input and output *P-h* curves is obtained, i.e the gap is less the convergence criterion ϵ.

Here, we study the influence of the the initial value on the final identified parameters. We consider a fictive material whose mechanical behaviour is governed by the following parameters : E = 320 GPa, σ_y= 6.0 GPa and K = 16 GPa. The obtained values and convergence trend are shown in FIG.2.15. One can notice that :

- the same final value of σ_{yf} is reached after ten iterations and this regardless of the input value confirming the unicity of identified parameters.
- the algorithm returns exactly the expected values for σ_y and K i.e, 6 and 16 GPa, respectively.

2.4.5.2 Application to the SPSed materials

At this stage of the project, the finite element model of the contact sphere / plan and the identification procedure were validated. It is therefore possible to put them into practice on the

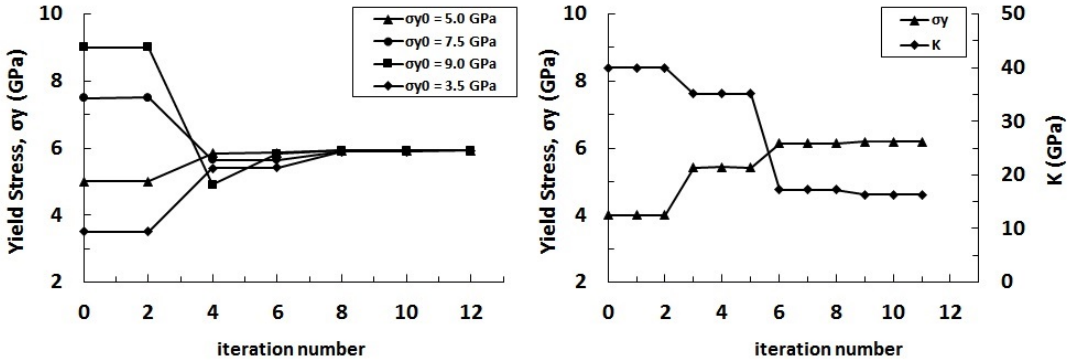

FIGURE 2.15: Convergence of the algorithm

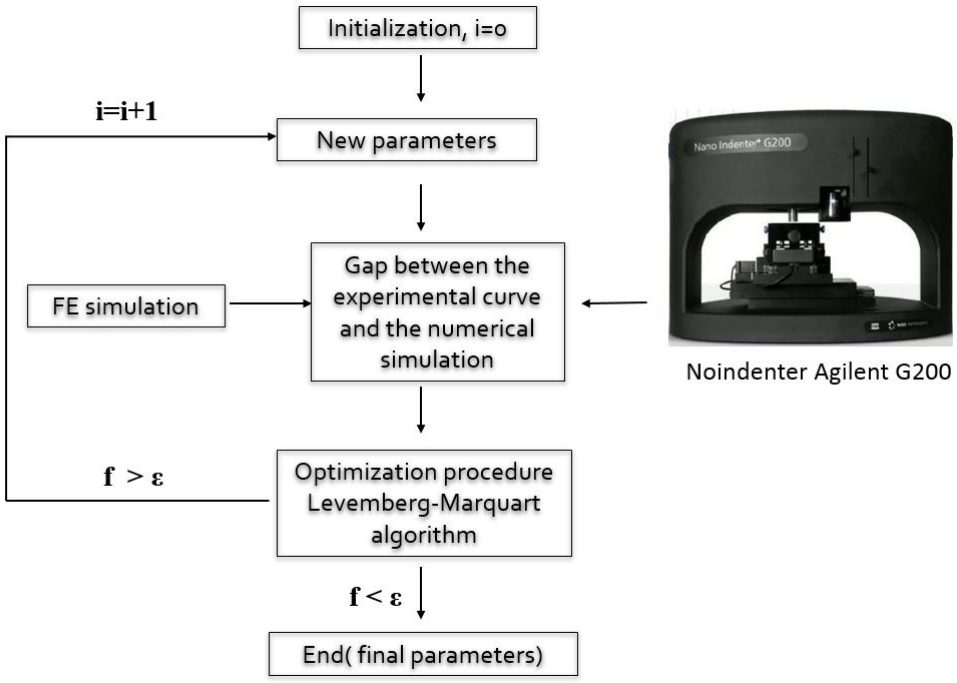

FIGURE 2.16: Flow chart of the numerical algorithm

different materials prepared. This will allow us to study the influence of processing conditions (temperature, additive amount, sintering pressure...) on the true σ-ε curves of silicon nitride.

We can more accurately simulate the stress and strain fields within the bulk Si_3N_4 and pressure distribution at the interface under vertical or pure rolling loading (no sliding). For the latter case, all the simulations were performed using in−house developed software Isaac which is based on semi-analytical approach of the contact problem [Jacq et al., 2002, Chaise and Nélias, 2011]. The conjugate gradient method (CGM) and Fast Fourier Transform (FFT) drastically reduce the computation time when compared to finite element software packages. The performed simulations

consist of three successive steps as shown in FIG.2.17 : (1) vertical loading to the maximum contact pressure, (2) rolling over a distance of 6 times the elastic contact radius and (3) unloading to zero

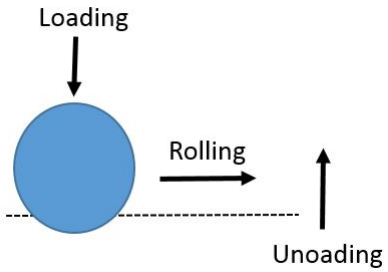

FIGURE 2.17: Rolling steps

An elastic diamond ball (E_i =1140 GPa, ν_i=0.07) of radius 0.2 mm was considered as rolling element over a flat homogeneous Si_3N_4 body. A maximum load of 45 N was applied corresponding to a maximum contact pressure P_{hertz} of about 24 GPa and elastic contact of about 30 μm.

2.5 Conclusion

We have briefly presented the different standard experimental techniques used to characterize the microstructure (density, grain size, phase composition) of silicon nitride materials processed by SPS. The mechanical property measurement techniques were also recalled. Bounded interface sectioning technique principles and the contribution of ion milling on the damage observation were emphasized.

We have also presented the preparation of the TEM electron transparent thin foils using FIB lift-out procedure. This approach is more costly because of the high hardness of Si_3N_4 but provides better accuracy in the selection of the area of interest. Finally, the instrumented indentation testing conditions were described.

The second part concerns the different numerical methods. A finite element model was build with the Abaqus commercial package and validated. Application of the Levenberg-Marquardt minimization algorithm to identify the plastic material parameters σ_y and K was also presented.

Chapter 3

Dense Silicon Nitride

Here, we present the microstructure, the mechanical properties and contact damage mechanisms (at surface and subsurface levels) of the fully dense materials with different grain sizes. FIB and high resolution TEM observation techniques are used to investigate the mechanisms of the subsurface damage. The load versus displacement curves are presented and the uniaxial stress-strain curves determined. Effects of grain size on the non-linear parameters, yield stress and hardening coefficient, are then analysed. Experimental and numerical indent profiles are compared for validation. We also performed pure rolling simulations to investigate the evolution of the plastic strain.

Contents

3.1 Material characterisation

Table 3.1 summarizes all the samples with their processing conditions and names. The yttria amount and sintering temperature are variable, while the sintering pressure and time are maintained constant, their values are 40 MPa and 15 min, respectively.

TABLE 3.1: List of the sintered materials and corresponding processing conditions

Material	Yttria,wt %	Temperature(°C)	Relative density (%)
Y1T1600	1	1600	98.3
Y1T1650	1	1650	98.3
Y1T1700	1	1700	98.3
Y2T1700	2	1700	98.9
Y3T1700	3	1700	> 99
Y4T1700	4	1700	> 99
Y5T1700	5	1700	> 99
Y5T1650	5	1650	> 99

3.1.1 XRD

X-ray diffraction patterns obtained for the silicon nitride materials sintered with addition of 1, 3 and 5 % of yttria are shown in FIG.3.1 as illustration example. It can be observed that diffraction peaks corresponding to α-Si_3N_4 become fewer with increasing the amount of sintering aid. Figure 3.2a shows the evolution of β-Si_3N_4 phase in the sintered materials as a function of the volume additive used during the sintering process. In addition, we illustrate in FIG.3.2b the evolution of β phase volume fraction as a function of the maximum processing temperature for 5 % of additive.

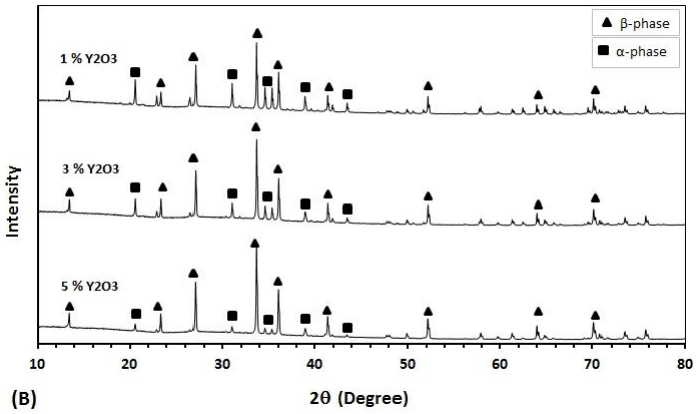

FIGURE 3.1: X-ray diffraction patterns of silicon nitride sintered with addition of 1, 3 and 5% Y_2O_3 at 1700 °C

In the first case, it can be easily noted that the $\alpha \rightarrow \beta$ phase transformation is enhanced through

the sequence 1% Y_2O_3 → 3% Y_2O_3 → 5% Y_2O_3. In the second one, the volume of β silicon nitride phase is relatively constant in the temperature range considered here, 1650°C - 1750°C.

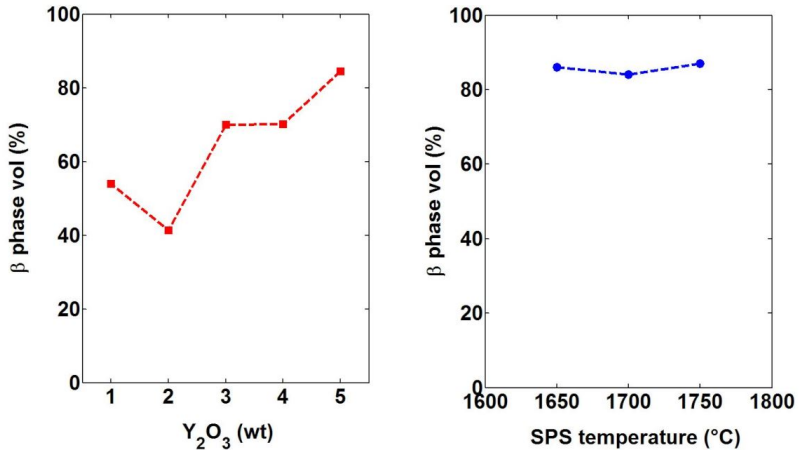

(a) Effect of yttria amount (b) Effect of SPS temperature

FIGURE 3.2: Effect of processing conditions on β phase composition of silicon nitride materials

3.1.2 Microstructures

From the table, one can report that fully dense materials were obtained when the amount of added Y_2O_3 was at least 3%, and more than 98% of the theoretical density was reached when only 1% and 2% of yttrium oxide were used. The evolution of the relative density in function of yttria amount is plotted in FIG.3.3. Also, one can notice that the relative density ρ / ρ_{the} (experimental density divided by the theoretical one) was not affected by the sintering temperature as it exceeded 1600°C, see TAB.3.1. It is due to a enough supply of intergranular liquid phase through which the mass transport takes place during spark plasma sintering.

Figures 3.4a, 3.4b and 3.4c show Electron Backscattered Diffraction (EBSD) maps of the silicon nitride materials processed with addition of 1, 3 and 5% of oxide additive at 1700°C, respectively. As expected, the resulting materials have microstructures showing significantly different grain sizes and morphologies. In fact, we can notice that gradual increase of the yttrium oxide amount from 1 to 5% caused a clear evolution from a fine microstructure with equiaxed fine grains to a coarse microstructure with random elongated grains. A quantitative measurement on electronic micrographs using commercial software ImageJ (National Institute of Health, USA) showed that for 3% Y_2O_3, the elongated β grains are of length 4.4 μm and diameter 1.0 μm while for 5 % Y_2O_3, they are of length 7.7 μm and diameter 1.5 μm. Thus, the aspect ratio, which commonly defined as length / diameter, is 5.4 and 7.7, respectively. It should be added that the elongated grains are of random spatial distribution in the matrix.

EBSD observations in FIG.3.5a, 3.5b and 3.5c provide some insights about the evolution of the number of elongated grains based on the sintering temperature for a fixed amount of additive, here 5 %. It is interesting to note that this evolution is not of monotonic manner : the number of large

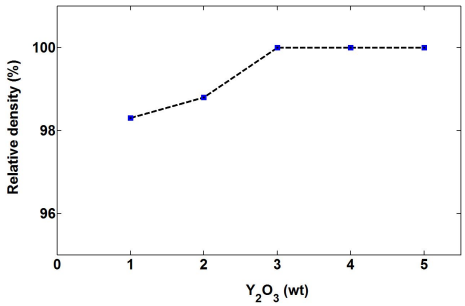

FIGURE 3.3: Evolution of the relative density of Si_3N_4 samples sintered at 1700 °C depending on the Y_2O_3 content

grains increases when the temperature is raised from 1650 °C to 1700 °C where the maximum is reached then decreases thereafter. In summary, having analysed XRD data and the microstructural evolution, we can draw the following conclusions : (i) for given sintering temperature, the number of elongated β grains increases with increasing the amount of yttria, (ii) for 5 % Y_2O_3, increasing the sintering temperature enhances grain precipitation so larger number of β grains are formed.

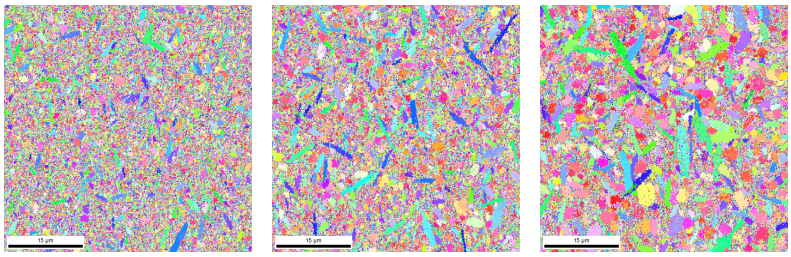

(a) 1% wt Y_2O_3 (b) 3% wt Y_2O_3 (c) 5% wt Y_2O_3

FIGURE 3.4: EBSD microcrographs of the materials sintered with addition of (a) 1% wt, (b) 3% wt and (c) 5% wt of Y_2O_3 at 1700 °C

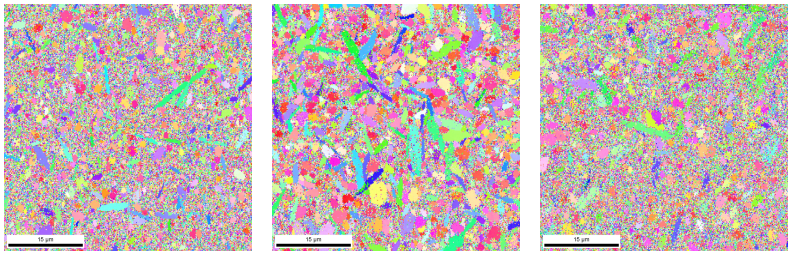

(a) 1650 °C (b) 1700 °C (c) 1750 °C

FIGURE 3.5: EBSD microcrographs of the materials sintered with addition of 5% of Y_2O_3 at 1650 (a), 1700 (b) and (c) 1750 °C

3.2 Mechanical properties

3.2.1 Influence of Yttria amount

3.2.1.1 E and H

As for the grain sizes, we have noticed a significant influence of Y_2O_3 amount on the mechanical properties of the processed silicon nitride based materials. The measured values for the Young's modulus and Vickers hardness are shown in FIG.3.6. One can observe that the elastic modulus linearly decreases from a maximum value of 336 GPa to a minimum value of 317 GPa when the amount of yttrium oxide increases from its minimum value of 1% to its maximum value of 5%. Concerning the Poisson's ratio, a constant value of 0.27 ± 0.01 is obtained for all the materials. This parameter is characterized by small variation in case of fully dense silicon nitride ceramics and thus regardless of the processing method. The hardness increases for 1% of yttria to 2 % where the maximum is reached ($\simeq$2000 Hv) and then linearly decreases with increasing the amount of the oxide additive to a minimum value of 1500 Hv.

Measured values using ultrasonic technique of the elastic modulus for materials with different additive amounts ranges between 336 and 317 GPa. The values are coherent with those already reported in the literature for fine, medium and coarse dense silicon nitride microstructures [Rhee et al., 2001]. The decrease of this main property is in large part related to difference of intrinsic elastic properties of α-Si_3N_4 and β-Si_3N_4 phases. In fact, it was reported in the first chapter that E_α lies between 340 and 362 GPa while approximate value of 312 GPa was reported for β-Si_3N_4 [Yeheskel and Gefen, 1985]. Therefore, an empirical mixture law can be used to relate the phase composition to the elastic modulus of final Si_3N_4 sample :

$$E_{Si_3N_4} = E_\alpha(1-f_\beta)+E_\beta f_\beta \tag{3.1}$$

The maximum gap between the values predicted using the previous approximation and the experimentally measured ones by ultrasonic technique is found to be about 3% (FIG.3.6a), a difference that remains acceptable in all application domains. Equation 3.1 is thus a very good approximation.

Regarding now the measured Vickers hardness, it is strongly dependent on the phase composition of silicon nitride materials thus, to the amount of sintering aid. In fact, it is found that the $\alpha-Si_3N_4$ grains have an intrinsic hardness which is about 25 % higher than the hardness of $\beta-Si_3N_4$ grains [Rice, 1998], values of 21 GPa and 16 GPa were reported. Materials containing larger fraction of $\alpha-$phase, i.e. small amount of yttrium oxide or sintered at lower temperatures have a higher Vickers hardness. A similar mixture law can be used to get a first estimation of the hardness value. In this study, even the small anomaly in the phase compositions at 2% of Y_2O_3 is recovered in the measured hardness value.

$$H_{Si_3N_4} = H_\alpha(1-f_\beta)+H_\beta f_\beta \tag{3.2}$$

However, it may be noted that the difference between the estimation based on Eq.(3.2) and the experimental values increases with for microstructures with larger grain sizes, see FIG.3.6b. Indeed, this latter one is an important parameter when dealing with the hardness of ceramic materials but it is not taken into account in the fitting equation. In this case, it was reported that

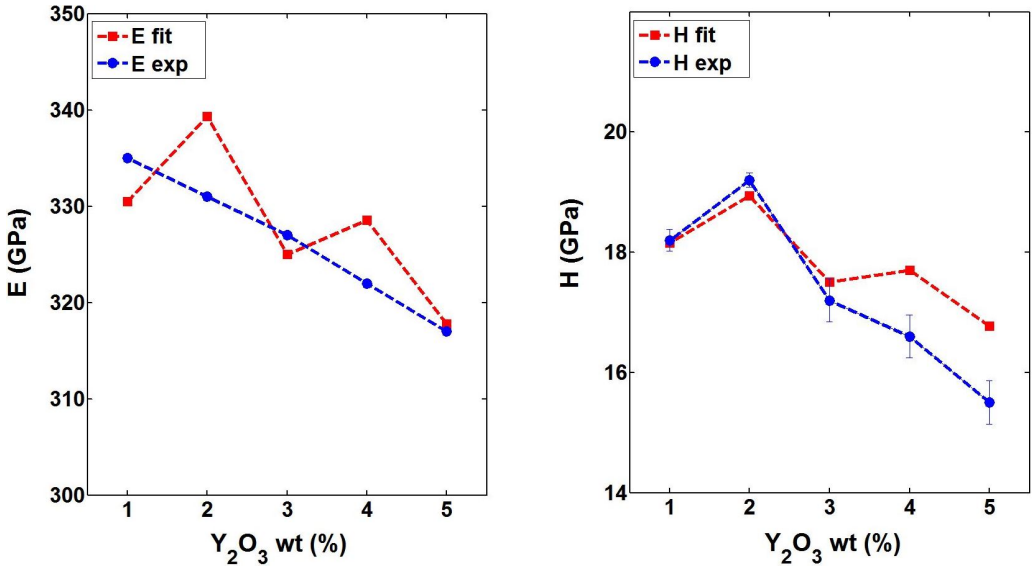

(a) Elastic modulus (b) Vickers hardness

FIGURE 3.6: Evolution of Young's modulus and Vickers hardness for sintered materials

Hall-Petch law better describes the dependence between Vickers hardness and the inverse square root of microstructure grain sizes [Trunec, 2008].

3.2.1.2 Bending strength

At room temperature, the 3-point flexural strength linearly increases with addition of larger quantities of Y_2O_3 from its minimum value of 600 MPa to the maximum value of 1000 MPa (3 % Y_2O_3) and a constant value is observed thereafter, see FIG.3.7. The improvement of the material strength up to 3% of Y_2O_3 may be attributed to the gradual elimination of the residual porosity which fosters initiation and propagation of the cracks. After the full density is reached, increasing of additive amount and led to self reinforced silicon nitride materials with high flexural strength [Steinbrech, 1992].

Figure 3.8 shows SEM micrographs of fracture surfaces of the Si_3N_4 specimens containing 1% Y_2O_3, 3% Y_2O_3 and 5% Y_2O_3 after failure on bending tests. The surfaces are fairly rough for the three materials, which therefore demonstrates a predominance of intergranular crack propagation. Such mode is typical for brittle materials especially when characterized by a fine microstructure (FIG.3.8a). Pulled-out grains can be clearly observed in case of medium (FIG.3.8b) and coarse microstructures (FIG.3.8c). This partially explains better flexural strengths for the materials containing elongated β grains.

3.2.1.3 Fracture toughness

Values of fracture toughness obtained using Niihara model for Palmqvist crack (Eq.(2.4)) system are shown in FIG.3.9a. The tests were performed under maximum loads P = 9.8 N and 19.6 N to estimate the influence of the maximum applied load. One can observe that relatively similar

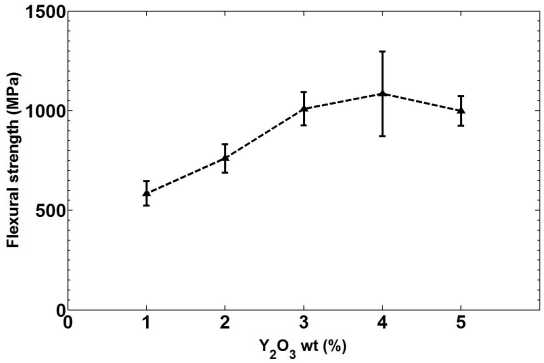

FIGURE 3.7: Evolution of fracture strength from 3-point flexural testing in function of yttrium oxide for sintering temperature of 1700 °C

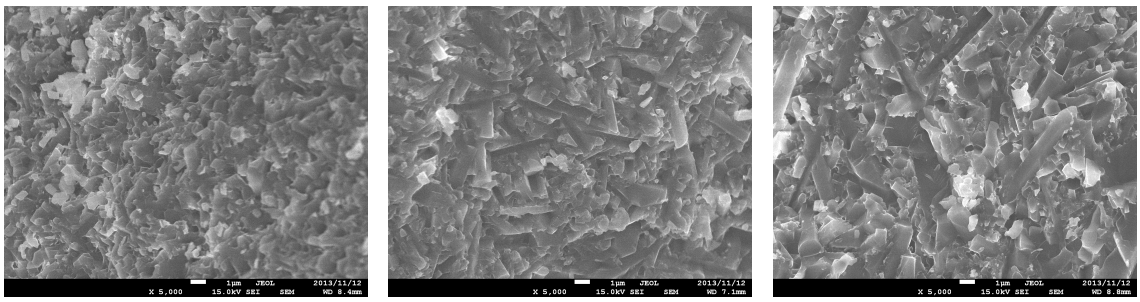

(a) 1% wt Y_2O_3 (b) 3% wt Y_2O_3 (c) 5% wt Y_2O_3

FIGURE 3.8: Fracture surface of a bending specimen sintered with different Y_2O_3 amounts

toughness values were obtained for both loads indicating no influence of P. On the other hand, values for K_C measured using Miyoshi model for median cracks (Eq.(2.5)) under a maximum load of 196 N are given in FIG.3.9b.

One can notice that the curve profiles are very similar for both models used in this work. Fracture toughness K_C slightly increases from 1 % to 2 % Y_2O_3 where maximum values of 6.75 and 8.75 MPa $m^{1/2}$ were obtained when considering Miyoshi and Niihara model, respectively. Then a relatively constant value for K_C were measured and thus independently of the amount of sintering additive. However, we can observe that Miyoshi model provides lower values when compared to Niihara model for each Y_2O_3 amount although no lateral fissure appears during testing to distort the crack length measurements and thus the toughness FIG.3.10a.

Toughening mechanisms such as crack deflection and bridging because of the elongated grains after crack propagation can be clearly observed under scanning electronic microscopy (FIG.3.10b and FIG.3.10c). The crack path is tortuous and propagate following the grain boundaries characterised by a lower toughness compared to the intrinsic α-Si_3N_4 and β-Si_3N_4 grains. This behaviour is likely to dissipate more energy and increase the fracture toughness of brittle materials up to factor two [Hutchinson, 1989] and leads to so-called *in-situ* composites or self-reinforced materials. However, it was also noted that when grain size becomes excessively large, it is energetically more favourable to the crack to propagate from a trangranular way, FIG.3.10c (see large β grain which

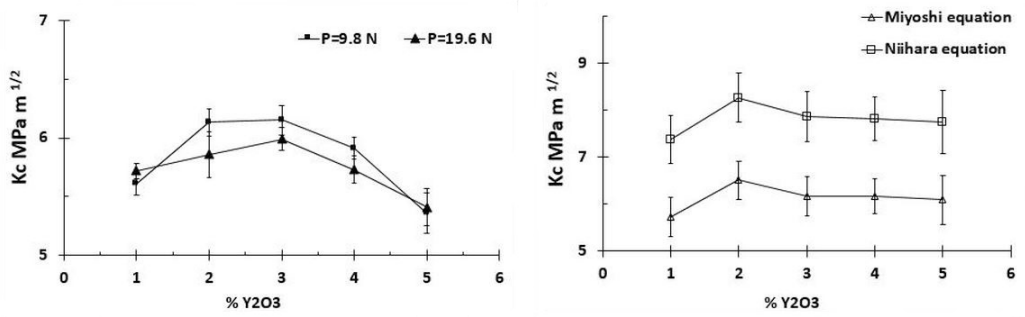

(a) Effect of maximum load for Palmqvist crack system (b) Niihara versus Miyoshi for median crack system

FIGURE 3.9: Toughness values measured by VIF under different applied loads using Niihara equation for Palmqvist cracks and for different amounts of yttria using Niihara and Miyoshi models for median cracks

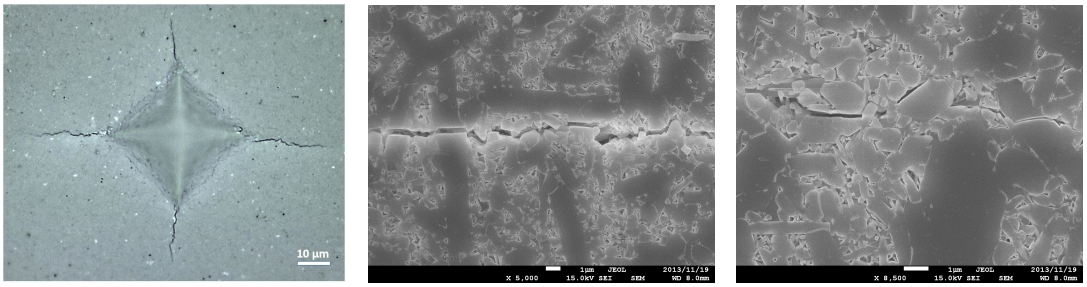

(a) Residual imprint after VIF testing (b) SEM micrograph (× 5000) (c) SEM micrograph (× 8500)

FIGURE 3.10: Observation of the crack path for the measurement of the fracture toughness

is traversed, on the right).

It is to note that Vickers indentation technique was used here to obtain a first approximation regarding the resistance of ceramic materials to cracks propagation. If more precise values are required or if there is a need to investigate the effect of grain size on K_C, other techniques such as single edge notched beam or chevron-notched beam, are to be preferred. They provide a more accurate values for the toughness but require more careful sample preparations.

3.2.2 Influence of SPS temperature

Table 3.2 summarizes the evolution of elastic modulus E, surface hardness H, bending strength σ_r and toughness by Niihara model for Palmqvist cracks regarding the spark plasma sintering temperature which ranges between 1600 and 1750 °C for 1 and 5 % of Y_2O_3.

It is clear that E is slightly affected by the sintering temperature for the two additive amounts with a mean standard deviation of less than 7 %. The maximum values 336 GPa and 317 GPa are reached at the highest temperature, i.e, 1700 °C, this temperature is optimal to maximize the Young's modulus.

TABLE 3.2: Effect of sintering temperature on the elastic modulus, hardness, flexural strength and toughness of Si_3N_4

Yttria,wt	1			5		
Sintering temperature (C)	1600	1650	1700	1650	1700	1750
E (GPa)	308	315	336	311	317	311
H (GPa)	15.8	14.2	18.2	17.2	15.5	14.2
σ_f (MPa)	638 $\pm$ 116	677 $\pm$ 82	585 $\pm$ 74	744 $\pm$118	999 $\pm$ 74	621 $\pm$62
Kc (MPa $m^{1/2}$)	4.65 $\pm$ 0.12	4.34$\pm$0.11	5.72$\pm$0.13	5.52$\pm$0.18	5.52$\pm$0.14	5.57$\pm$0.13

Concerning the Vickers hardness, one can observe a significant influence of the temperature for 1% and 5% Y_2O_3 with maximum values of 1813 and 1761 Hv at 1700 and 1650 °C, respectively. The measured flexural strength depends on the sintering temperature. The maximum values of 677 MPa and 999 MPa are reached at 1650 and 1700 °C for 1 and 5% of Y_2O_3, respectively. Finally, the toughness value remains fairly constant throughout the temperature range considered in this work.

3.3 Contact damage

Having characterized the processed materials under different aspects, we are now interested in the following section on their response under a contact loading on the surface and under the residual indents. The observations were performed at two different scales (macroscopic and mesoscopic) by using indenters of various radii. We will not go into detail regarding the mechanics at macro scale. On the other hand, we took a closer look about the mechanisms at the mesoscopic scale by means of advanced techniques such as Focused Ion Beam and Transmission Microscopy.

3.3.1 Surface damage

The tests were performed using a diamond indenter of radius R_2 = 1.0 mm. For fine silicon nitride, one can clearly observe from optical observations in FIG.3.11 that increasing the applied load enlarges the contact area. In addition, scanning of the residual depressions revealed that they are of increasingly depths, 1.2, 1.7 and 2.5 µm for 750, 1000 and 1500 N, respectively. Consequently, these measurements indicate a more important subsurface damage. In addition, we could observe that the first ring crack initiate when the applied load is 750 N (FIG.3.11a). The initiation of the cracks is controlled by the pre-existing surface flaws or defects under the influence of the radial part of stress and occurs during the loading step. Some models have been proposed to take advantage of this form of crack to easily measure the brittle material toughness [Warren, 1978]. Going back to the critical load for crack initiation, P_c : it corresponds to a maximum contact pressure P_{hertz} of about 21.9 GPa. This loading level is not reached during a normal service but can be observed in the presence of hard inclusions or impurities.

If the applied load is gradually increased up to 1000 N (FIG.3.11b) then to 1500 N (FIG.3.11c), the surface cracks develop in a significant way until the failure of the specimen.

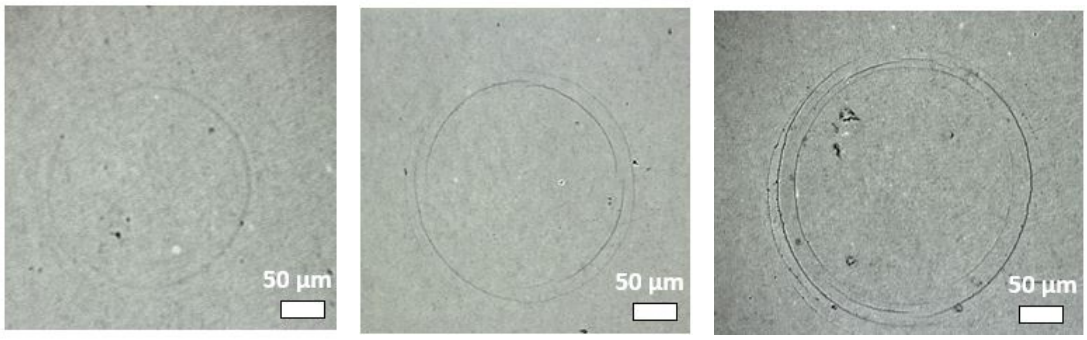

(a) 750 N (b) 1000 N (c) 1500 N

FIGURE 3.11: Optical observation of surface damage under increasing loads for Si_3N_4 with fine microstructure

Regarding the coarse Si_3N_4, the observed fracture mechanisms are quite similar, except for highest load, i.e, 1500 N. Indeed, in addition to the classical ring cracks well developed radial cracks were also observed, see FIG.3.12. They are similar to those characterizing sharp indenters

such as Berkovich or Vickers tips. Contrary to the first type, the initiation of radial fissures occurs during the unloading step [Swain and Hagan, 1976]. We do not show here the response of the material with an average microstructure (sintered with 3% of Y_2O_3) because the evolution of surface cracks was very similar to the one with fine microstructure.

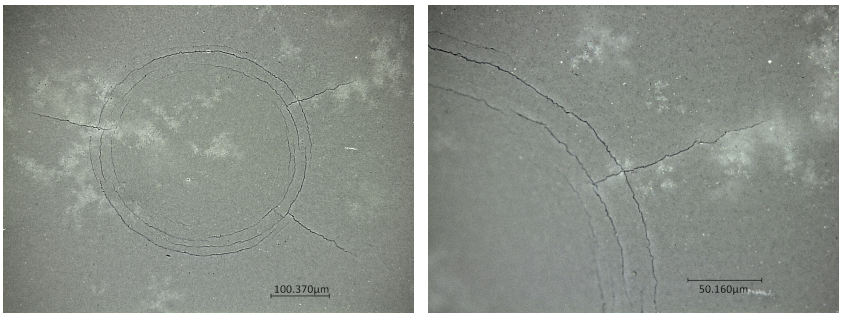

(a) 1500 N (b) 1500 N-higher magnification

FIGURE 3.12: Surface damage in coase Si_3N_4 at peak load P = 1500 N

3.3.2 Subsurface damage

3.3.2.1 FIB observations

Because the bearing ball radii can vary by several orders from one application to another, it would be attractive to study the influence of the indenter size on the response of the materials developed. The tests in the following section were performed using a smaller diamond indenter of R_2 of 0.2 mm radius under maximum load of 70 N on standard Instron tensile machine. At this scale no cracks were observed on the surface for the three materials as illustrated for example in case of coarse Si_3N_4 (FIG.3.13a). However, there were permanent indents as shown in (FIG.3.13b). In addition, figure 3.14a illustrates the evolution of indent profiles as function of the peak load. The surface depressions are of increasingly depth, which indicates an accumulation of the subsurface damage as plotted in FIG.3.14b.

Because of the technical limitation regarding the maximum observable depth, it is mandatory to make a compromise between the size of the area and quantity of damage. We decided to apply a maximum load of 45 N equivalent to maximum pressure $P_{hertz} \approx 24.0$ GPa. This charge also corresponds to the first easily observable residual imprint on the sample surface.

Let's take a closer look at the tensile stress, σ_m given by :

$$\sigma_m = \frac{1-2\nu_s}{3} P_{hertz} \tag{3.3}$$

Which gives $\sigma_m = 3.2$ GPa, a value much higher than the measured macroscopic strength σ_f for all the elaborated materials which maximum is slightly higher than 1.0 GPa as discussed in section about the mechanical properties. The fact that no cracking mode on the surface of the sample is related to the volume sollicited in the indentation is much smaller than the one considered in 3 point bending tests.

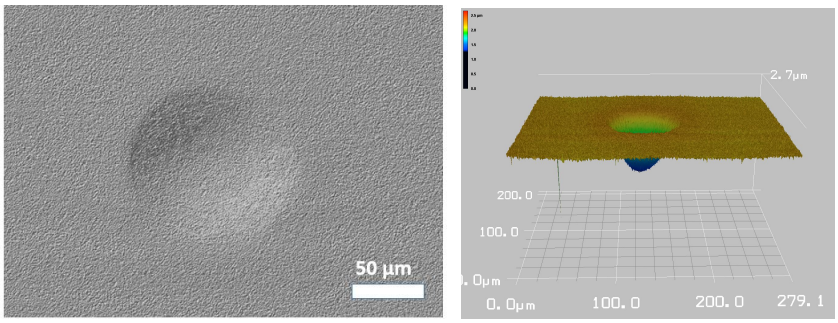

(a) Surface observation (b) 3D profile of the indent

FIGURE 3.13: Surface contact damage observation in coarse Si_3N_4 after indentation with a sphere of radius 0.2 mm at peak load P = 70 N

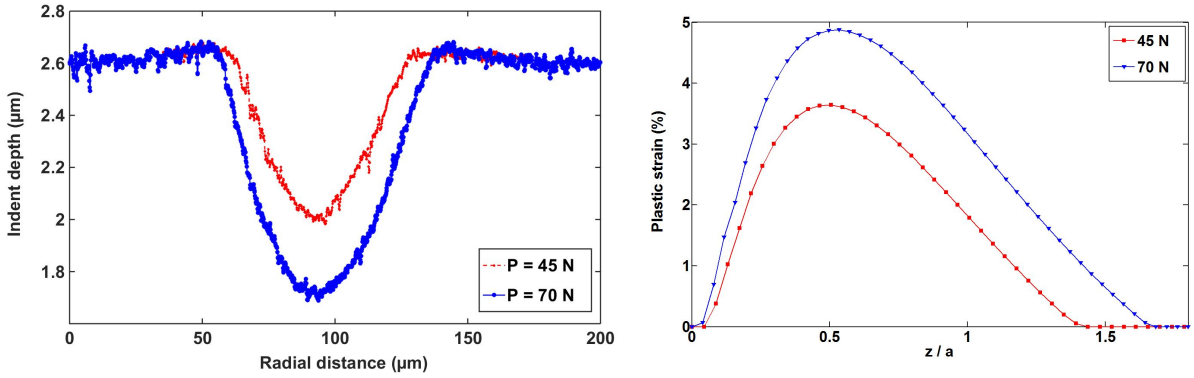

(a) Indent profiles (b) Damage profiles

FIGURE 3.14: (a) Evolution of indent depth in coarse silicon nitride after indentation with sphere of radius 0.2 mm, (b) plastic strain profiles under 45 N and 70 N

In addition, it is admitted that elongated β grains improve the resistance of ceramics with coarse microstructures to the propagation of long cracks leading to materials with R-curve behaviour, i.e increase of toughness with increase of crack length. So, the resistance to short cracks is found to be deteriorated [Rhee et al., 2001]. We know from the Hertz theory that for $\nu_s = 0.3$ the value of the maximum principal shear stress τ_m :

$$\tau_m = 0.31\, P_{hertz} \tag{3.4}$$

Therefore, τ_m = 7.7 GPa, a value higher than $\frac{\sigma_y}{2}$. The exact values of uniaxial material yield stress σ_y will be given and discussed later (section 3.4).

At smaller scale, the material underwent a permanent deformation without evidence of ring cracks at the surface, see FIG.3.15a. The deformation is accompanied by high density of short cracks (FIG.3.15b). The size of the microcracks is found to be about few micrometers, order of

grain sizes, they initiated from the weak grain boundaries and propagate along and across the adjacent grains. We can also observe a uniform distribution of the cracks in the damaged zone.

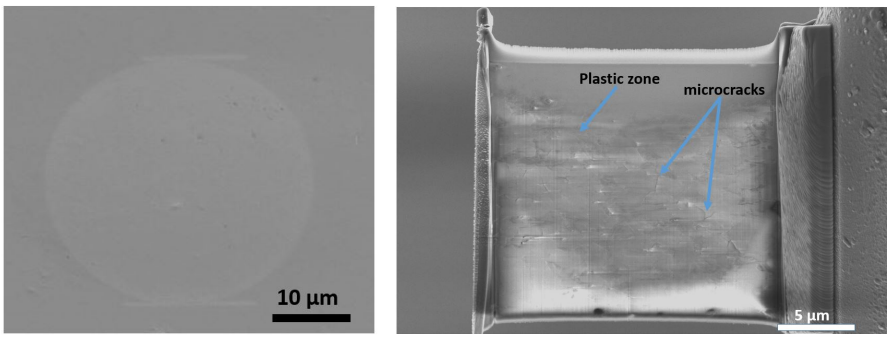

(a) Carbon deposition at the surface of the sample (b) FIB cross section beneath the residual impression

FIGURE 3.15: Subsurface damage in coarse silicon nitride after indentation with a sphere of radius 0.2 mm at peak load P = 45 N

For a better estimation of the lifetime time of the rolling elements, damage modes which occur under contact loading should be better quantified. In this context, Rhee et *al.*[Rhee et al., 2001] assumed that shear and tensile stresses lead to quasi plastic and fracture modes in brittle materials, respectively. The authors then experimentally measured the critical loads for fracture P_c and localized deformation P_y and finally introduced a transition radius r^* for various brittle ceramic materials. Quasi plastic mode occurs if the indenter radius R is smaller than r^*, i.e. $P_y \leq P_c$ while fracture occurs when R is larger than r^*, i.e. $P_y \geq P_c$. The authors calculated a value r^* of 12 mm for coarse Si_3N_4 having approximatively the same mechanical properties. We have experimentally demonstrated that the transition radius for the sintered material with heterogeneous grain size ranges between 0.2 and 1 mm. This value is significantly lower than that predicted by the previous model. The deviation from the obtained results of Rhee et *al.* is probably due in one hand to the hypothesis of perfect plasticity used to build the described model. In fact, we have demonstrated that the constraint factor H / Y depends on the grain sizes (no longer a material invariant), and on the other hand to the microstructural properties especially the β grains and the glassy boundary phase which nature has a significant effect on the degree of contact damage and the crack initiation critical load [Lee et al., 2005]. According to Lawn [Lawn, 1998], the plasticity dominates for sharper i.e, smaller, indenters because the load to initiate cracks becomes high enough that plasticity occurs first. The assumption concerning the distribution of critical flaws has also been put forward then rapidly abandoned.

3.3.2.2 TEM observations

In order to go through the damage mechanisms at the nanometre scale, thin specimens for transmission electron observations were prepared from the damage zones under the residual indents. High resolution TEM observations (Titan3 G2 60-300, FEI Company) under acceleration voltage of 300kV and beam current of 0.060 nA revealed both intergranular and transgranular propagation of the microcracks (FIG.3.16). These cracks were not observed in the matrix away from

the indents or in blank specimens. The observation confirms that the different damage modes are caused by the charge applied to the Si_3N_4 solid surface.

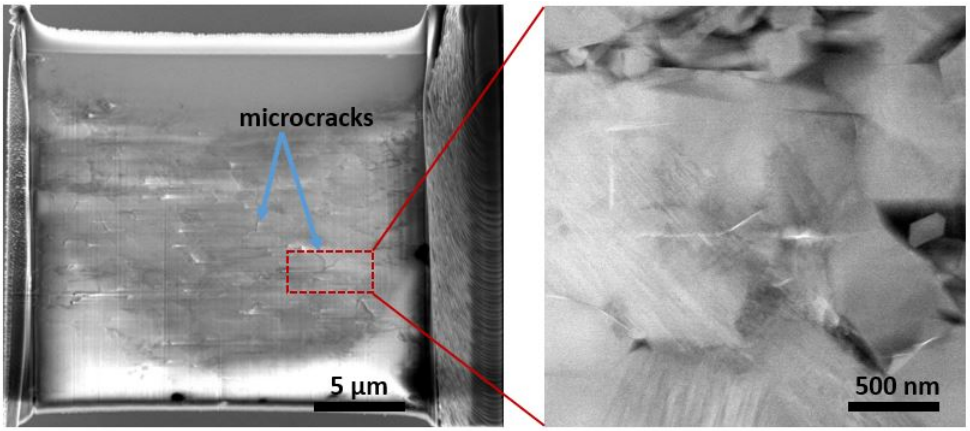

FIGURE 3.16: TEM observations of the damaged area

Evident traces of sliding system activation in the elongated grains located in the damaged area can be observed, FIG.3.16. According to Evans and Sharp [Evans and Sharp, 1971], the most stable dislocations in elongated β-Si_3N_4 are expected to have $\langle\ 0\ 0\ 0\ 1\ \rangle$ Burgers vector and $\{1\ 0\ \bar{1}\ 0\}$ primary slip system. In spite of the strong covalent bonds which characterize the ceramic materials, contact loading generates shear stress high enough to overcome apart the atomistic links. An illustration example of the observed line defects under high magnifications is shown in FIG.3.17. A large part of the crystal remain free of defects while other are severely distorted. It should be noted that this type of defects was observed in the center and boundaries of the damaged area.

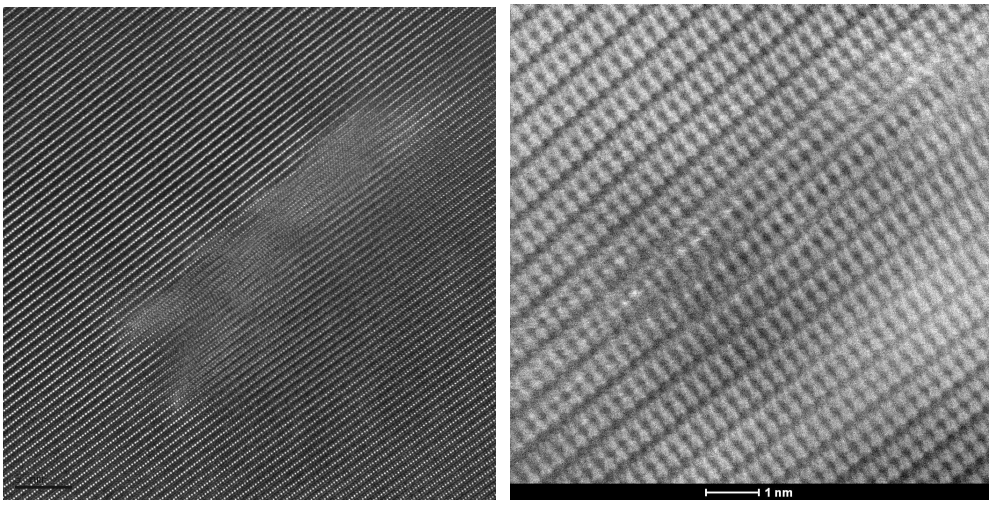

(a) Magnification $\times$ 3.8 10^5 (b) Magnification $\times$ 7.2 10^6

FIGURE 3.17: High-angle annular dark-field imaging of the lattice defects

3.4 Mechanical behaviour laws

We have seen in the previous section that the developed materials have a nonlinear behaviour. In the following sections, we will attempt to model this behaviour for representative materials. To assist in the reading of the following sections, we recall here the main information regarding the materials selected :

- F-Si_3N_4 : it has a bimodal fine microstructure consisting of 45.3 vol % of equiaxed α grains and 54.7 vol % of fine β grains ;
- M-Si_3N_4 : the microstructure is bimodal and consists of 30 vol % of equiaxed α grains and 70 vol% of β with mean of length 4.4 µm and diameter 1.0 µm ;
- C-Si_3N_4 : the microstructure is coarse and consists of 15.5 vol % of equiaxed α grains and 84.5 vol % of β with mean of length 7.7 µm and diameter 1.5 µm.

The mechanical properties such elastic modulus and hardness of the above listed materials will be given if needed.

3.4.1 Plastic parameters

Typical load−displacement curves for the three materials obtained using the spherical tip of 42 µm radius up to a maximum load of 9 N are plotted in FIG.3.18. For illustration purpose, the Hertz solution (elastic) is plotted for each material. The fits were calculated using the identified elastic moduli. A good correlation between the initial loading stage of the experimental curves and the Hertz fits was observed. Substantial deviation from linearity in the high load region indicates plastic deformations. In fact, despite the large elastic recovery in the unloading part of the indentation curves, residual irreversible displacements after unloading still subsisted. Furthermore, the residual displacement is more pronounced and the deviation from linearity occurs earlier with increasing the heterogeneity of the microstructure, i.e. the grain sizes.

Table 3.3 summarizes the identified yield strength σ_y and hardening parameter K values of sintered silicon nitride specimens. For comparison purpose, we have also reported the elastic modulus measured by ultrasonic technique E_{us} and yield stress Y given by the Tabor's relation [Tabor,

TABLE 3.3: Plastic parameters for F-Si_3N_4, M-Si_3N_4 and C-Si_3N_4. The values and standard deviations are based on 4 different identifications for each material

Material	Y1T1700 (F-Si_3N_4)	Y3T1700 (M-Si_3N_4)	Y5T1700 (C-Si_3N_4)	Ref. [Lee et al., 1997]
E_{us}(GPa)	336	327	317	315 - 335
E_{id}(GPa)	330 $\pm$ 3.0	322 $\pm$ 2.3	357 $\pm$ 1.9	
Y (GPa)	5.9 $\pm$ 0.1	5.7 $\pm$ 0.2	5.1 $\pm$ 0.2	
Yield stress σ_y(GPa)	10.0 $\pm$ 0.3	9.4 $\pm$ 0.1	7.8 $\pm$ 0.1	7.3 - 11.7
Hardening K(GPa)	41.5 $\pm$1.0	25.8 $\pm$1.1	31.4 $\pm$5.9	
H / σ_y	1.82	1.87	1.99	1.79 - 2.16

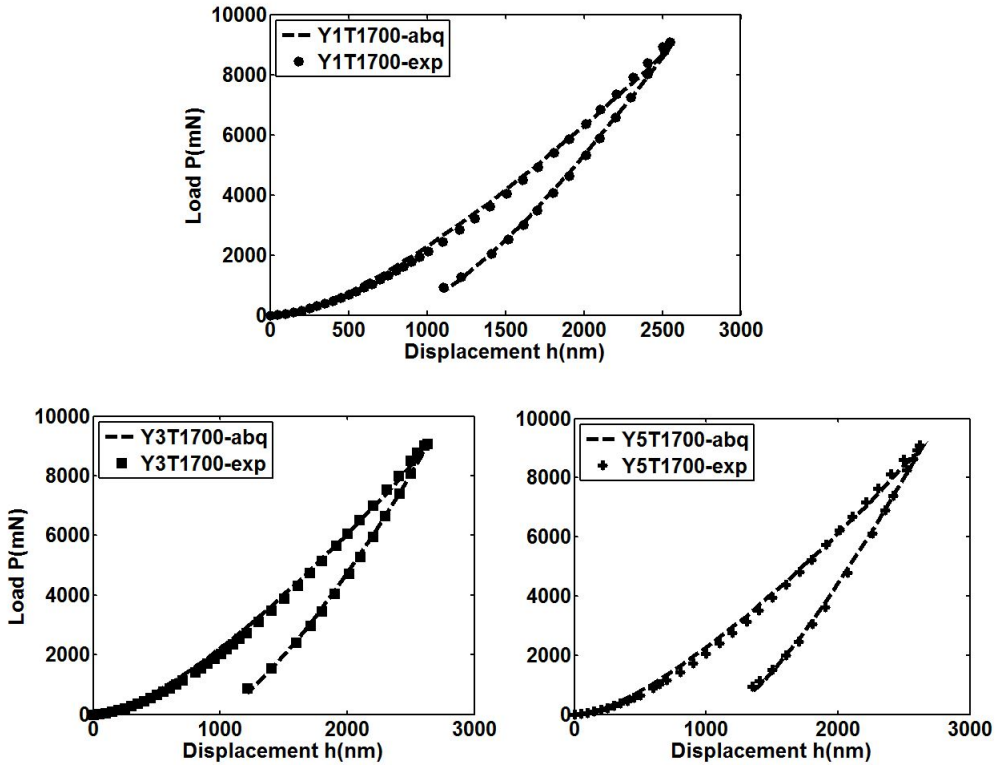

FIGURE 3.18: Experimental and numerical *P-h* curves for fine, medium and coarse Silicon Nitride specimens

1951] :

$$Y = H_v/c \tag{3.5}$$

where H_v is the Vickers hardness and $c \simeq 3$.

One can notice a good agreement between the identified elastic modulus E_{id} and the experimental one for F-Si_3N_4 and M-Si_3N_4. The gap between the experimental values and numerical simulations is more pronounced for C-Si_3N_4 for which a difference of about 15% was observed. The yield stress σ_y decreases by about 20 % with increasing the heterogeneity of the microstructure through the sequence F-Si_3N_4 $\rightarrow$ M-Si_3N_4 $\rightarrow$ C-Si_3N_4. The Tabor's relation with $c \simeq 3$ gives an overestimated value for σ_y especially in the case of the silicon nitride with a fine microstructure. From the experimentally measured Vickers hardness and numerically identified yield stress, the estimated constraint factor H / σ_y was calculated and reported. It can be seen that the values obtained for the factor range between 1.8 and 2.0 depending on the grain sizes. We calculated about 10 % increase through the sequence F-Si_3N_4 $\rightarrow$ M-Si_3N_4 $\rightarrow$ C-Si_3N_4.

For ductile materials, well known Hall-Petch [Hall, 1951] or Orowan equations describe an inverse relation between the yield stress and grain size d in the metals at room temperature,

$$\sigma_y = \sigma_0 + \frac{k_y}{\sqrt{d}} \tag{3.6}$$

where σ_0 and k_y are material coefficients.

We noted the same trend for the materials of this study identified as brittle in the literature : SPSed silicon nitride ceramics with small grains have the highest yield strength. The latter property diminishes with increasing the microstructure coarseness and the minimum obtained for C-Si_3N_4. One can theorize that the mechanisms are similar for both material classes : the effect of the grain boundary density on the movement of dislocations for which the mean free paths depend on the grain size.

Grain boundary chemistry play also an important role in the mechanical response of studied materials. Indeed, it is recognized that these last are susceptible to be weakened and their composition changed by the addition of a significant amount of a sintering additive as it is the case for C-Si_3N_4 [Xu et al., 1995]. The weakening enhances the quasi-plastic deformation and partially suppress cracking at the surface as it was experimentally demonstrated.

The hardening parameter K does not point to a clear trend. However, typical high values superior to 20 GPa were obtained regardless of the grain sizes with a maximum value of 40 GPa in case of F-Si_3N_4. The high values of K indicate that Si_3N_4 behaviour is largely dominated by the elastic part. The result agrees well with the conclusions of Lee et *al.* [Lee et al., 1997].

The high values of the work hardening parameter K, typical for brittle materials, contradict the perfect plasticity assumption for silicon nitride ceramics under the Hertzian contact. This observation is confirmed by the discrepancy between the values of σ_y and that given by the Tabor's relation, especially in the case of the finest microstructure. At least 30% deviation from the value of $c = 3$ usually considered for silicon nitride constraint factor was calculated. Nevertheless, the values obtained by inverse identification must be compared to other characterization techniques before final validation.

The *P-h* curve profiles are very similar for the three materials sintered with addition of 5% of Y_2O_3 and processes under maximum temperatures of 1650, 1700 and 1750 °C, see FIG.3.19. Table 3.4 summarizes the phase composition in the materials and the different parameters previously introduced. The initial slope is not very different which is consistent with the measured value of the elastic modulus. The maximum displacement seems also to be the same for the three materials. The identification method was also applied to these different temperatures, the results are reported in TAB.3.4.

The values obtained for the three materials are very close, and this independently of the parameter considered. We recall from the section 3.1.2, that these materials are fully dense but have microstructure with dissimilar grain sizes.

3.4.2 Validation

Although the identified parameters seem consistent with the microstructure grain size gradual evolution, the theory based on Hall-Petch prior work and the values of previous studies reported in published papers, additional tests are needed for final validation. TEM nanoindentation of ceramic nanoparticles [Calvié et al., 2014] or nanocubes [Issa et al., 2015] and compression of micropillars [Östlund et al., 2011] may be considered. But in each case, a sophisticated *in-situ* nanomechanical testing system is required and the derivation of behaviour laws at larger scale has not been addressed yet. Here, we will use a simpler approach. The profiles of the permanent indents on F-Si_3N_4, M-Si_3N_4 and C-Si_3N_4 were obtained using keyence VK-100 profilometer. The indentation tests

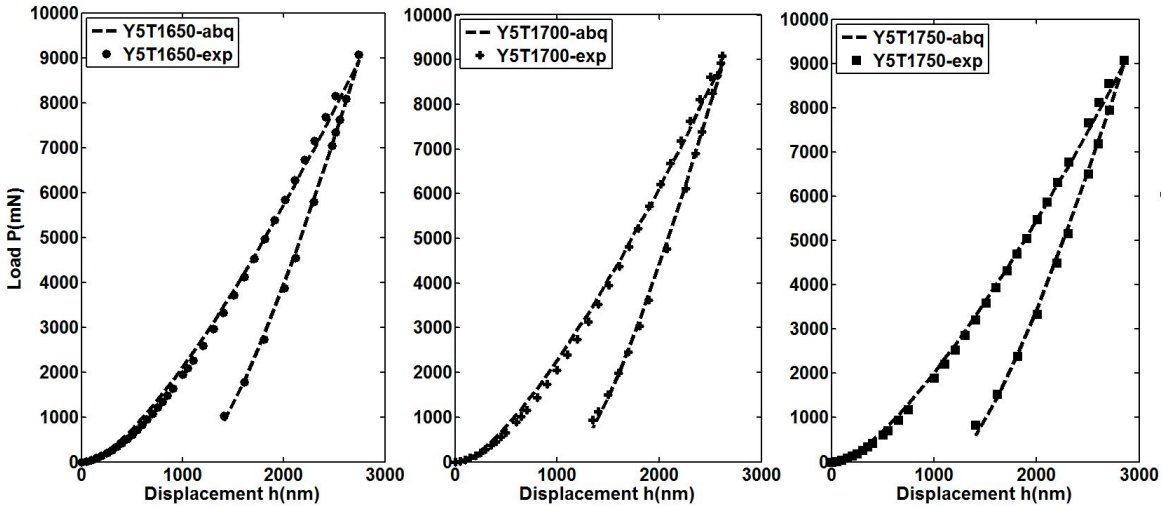

FIGURE 3.19: Experimental and numerical *P-h* curves silicon nitride specimens sintered at different temperatures

were performed on standard tensile machine using the diamond sphere of radius R = 0.2 mm under maximum load of 45 N. The first observation concerns the experimental depth of the residual impressions : it increases through the sequence F-Si_3N_4 $\rightarrow$ M-Si_3N_4 $\rightarrow$ C-Si_3N_4. This result is consistent with the decrease in hardness as function of grain sizes as discussed in section related to the mechanical properties (cf. sec 3.2.1).

In parallel, we have used the true stress-strain curves previously identified on Abaqus software to numerically estimate the material response under the same contact conditions. The results about the vertical displacement U_z of slave surfaces (part of the specimens in contact with the indenter) at the end of the unloading step are plotted in FIG.3.20.

One can notice that the numerical model reproduces well all the general experimental profile features for the three indented materials. The radius of the numerical profiles can be slightly underestimated by the model but the error remains acceptable, error less than 5 %. What is interesting is that the height of pile-up, which can generate a significant overpressure under rolling conditions, is well captured by the numerical simulations. On the other hand, it is found that the maximum depths were overestimated by FE calculations in all cases. In fact, the experimentally measured and numerically simulated maximum depths are reported in TAB.3.5. One can observe that the higher deviation is reached for C-Si_3N_4 with a gap $\approx$ 18%. A large part of this mismatch is due to the unavoidable experimental and numerical uncertainties (exact indenter shape, smooth surfaces, isotropic assumption...).

However, one can rightly think that the supplementary part in the gap may be attributed to the limited number of parameters introduced to describe the non-linear behaviour of the ceramic materials. In fact, in the bilinear law we recall below, all the damage is modelled thanks to the plastic deformation.

TABLE 3.4: Plastic parameters for silicon nitride with 5% Y_2O_3 SPSed at 1650, 1700 and 1750 °C. The values and standard deviations are based on 4 different identifications for each material

Material	Y5T1650	C-Si_3N_4	Y5T1750
β phase vol(%)	84	85	85
E_{us}(GPa)	311	317	311
E_{id}(GPa)	320 ± .0	357 ± 1.9	314 ± 1.0
Y (GPa)	5.7 ± 0.1	5.1 ± 0.2	3.55 ± 0.2
Yield stress σ_y(GPa)	8.0 ± 0.1	7.8 ± 0.1	7.3 ±0.1
Hardening K(GPa)	34.5 ±1.	31.4 ±5.9	32.1 ± 2.3
H / σ_y	2.15	1.99	1.94

$$\begin{cases} \sigma = E\varepsilon, & \text{if } \sigma \leq \sigma_y \\ \sigma = \sigma_y + K\varepsilon_p & \text{if } \sigma \geq \sigma_y \end{cases} \tag{3.7}$$

Indeed, in addition to slip system activation and dislocation motions, FIB and TEM observations revealed other damage phenomena consisting of short cracks initiation at the weak points, i.e, grains boundaries, in the microstructures. It is clear that the proposed model based only on plastic deformation can not describe all the damage modes. More complex constitutive laws including different mechanisms (microcracks initiation and coalescence) may correct the discrepancy between the experimental and numerical profiles.

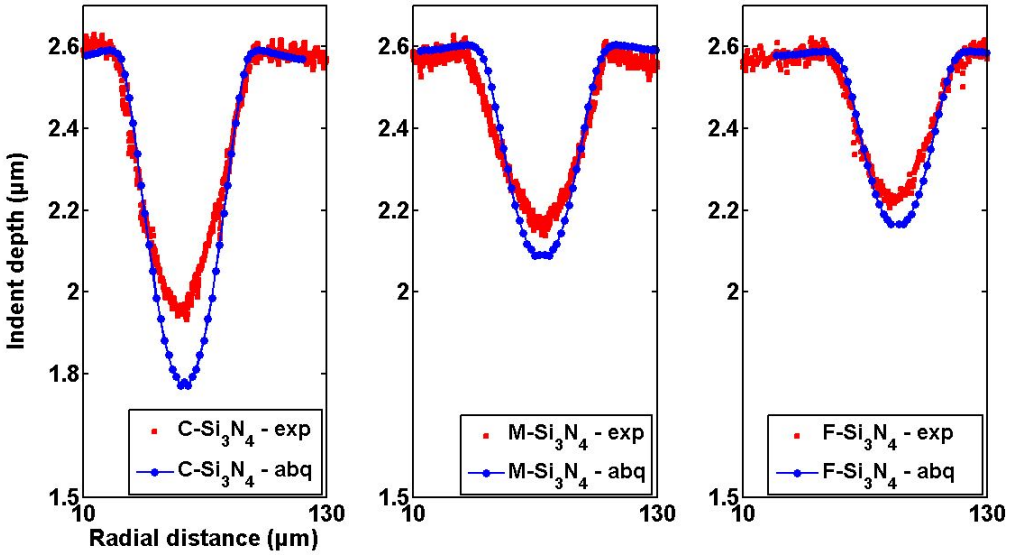

FIGURE 3.20: Experimental versus simulated profiles for materials sintered with 5% Y_2O_3, 3% Y_2O_3, 1% Y_2O_3

TABLE 3.5: Experimental depth versus numerical calculation under vertical load P= 45 N with sphere of radius R_1 = 0.2 mm

Materials	F-Si_3N_4	M-Si_3N_4	C-Si_3N_4
Experimental depth (μm)	0.42	0.49	0.69
Numerical depth (μm)	0.48	0.53	0.81
Gap (%)	+14.0	+ 9.3	+ 17.6

3.4.3 Strain and stress fields

We have seen in the section describing the FIB technique that it is technically impossible to image the whole damaged area at the mesoscopic scale. We will inevitably turn towards numerical modelling to estimate the extent of the subsurface damaged area at the small scale. In fact, taking advantage on the identification of silicon nitride nonlinear parameters, it is possible to quantify the subsurface plastic zone as shown in FIG.3.21 for fine (F-Si_3N_4) and coarse (F-Si_3N_4) microstructures. The plastic deformation remains confined to a small zone which dimensions are in the order of the elastic contact radius, i.e ≈ 30 μm for applied load P = 45 N and sphere radius R = 0.2 mm. The shape of this plastic area also confirmed that this damage mode follows the contours of the principal shear stress

$$\tau = \frac{1}{2}|\sigma_1 - \sigma_3| \tag{3.8}$$

To quantify the damage degree in the three materials, we plot the plastic strain profile along the symmetry axis in FIG.3.22a. The maximum values of plastic strain slightly depend on the grains size. In fact, value of 2.5 %, 3 % and 3.5% at depth z approaching half the elastic contact radius were measured for F-Si_3N_4, M-Si_3N_4 and C-Si_3N_4, respectively. These results are consistent in relation to the variation of the yield strength and indent depths that were discussed in the previous section.

In addition to plastic strain, we are able to plot the surface pressure profiles when taking into account the nonlinear part of σ - ε curves, the results are shown in FIG.3.22b for the three materials. One can observe a clear deviation of the all profiles from the Hertz solution based on elastic assumptions. The deviation is about 35, 30 and 25 % for the fine, medium and coarse microstructures, respectively. This result is not surprising with respect to previous paragraph. In fact, damage accumulation reduces the surface pressure until a plateau is reached in the case of perfect plasticity.

Similar numerical simulations were performed for the materials Y5T1650, C-Si_3N_4 and Y5T1750 which, it should be remembered, were sintered at 1650, 1700 and 1750°C, respectively. The profiles of the resulting plastic strain after the ball is discharged are plotted in FIG.3.23. We clearly observe that the response of the three materials is very close with slight variation for maximum deformations and contact radii.

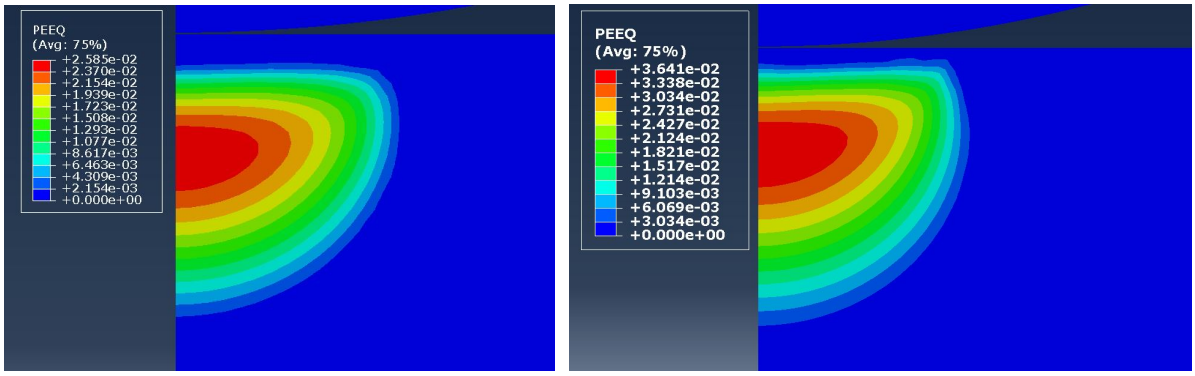

(a) F-Si_3N_4 (b) C-Si_3N_4

FIGURE 3.21: Plastic zone in fine and coarse specimens from Abaqus simulations taking into consideration the nonlinear behaviour of materials

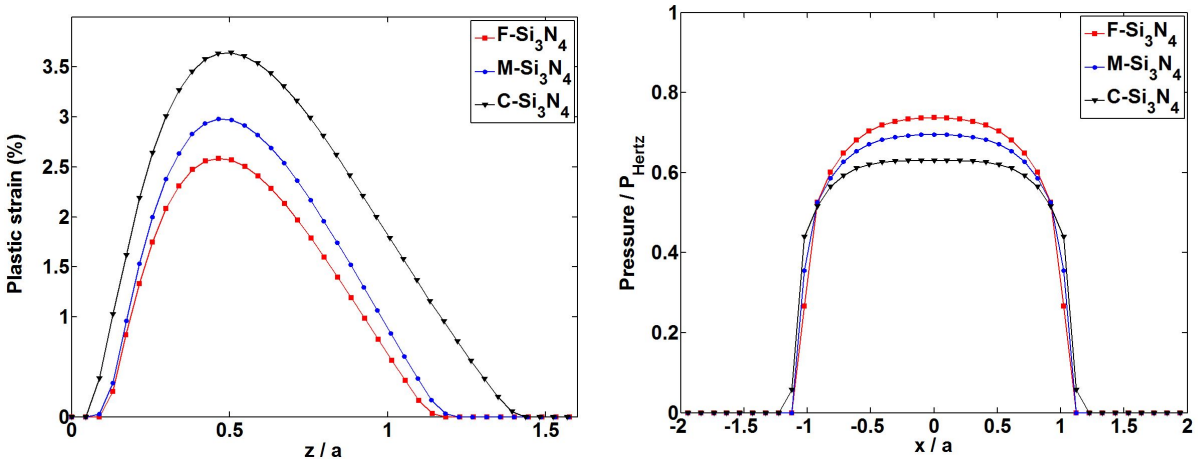

(a) Equivalent plastic strain after complete unloading (b) Contact pressure at maximum load

FIGURE 3.22: Equivalent plastic strain profile in depth at the center of the contact and pressure profiles under maximum load for the three materials

3.4.4 Rolling simulations

Because the first application for which are designed the silicon nitrides is bearings in the automotive or aeronautic industries where the materials are subjected to high number of cycles up to several millions. It is therefore crucial to keep a close look on the evolution of subsurface plastic strains. Here, the plastic zones at the maximum of vertical load of 45 N and after pure rolling (friction neglected) over a distance of 6 times the elastic contact a. The same maximum load is applied during the rolling step as shown in (FIG.3.24). The movement of the ball has an important effect on the damaged (plastic) area. In fact, it is well known that in the plastic regime, the zone size with a permanent deformation is slightly larger than the Hertz contact radius, see FIG.3.25

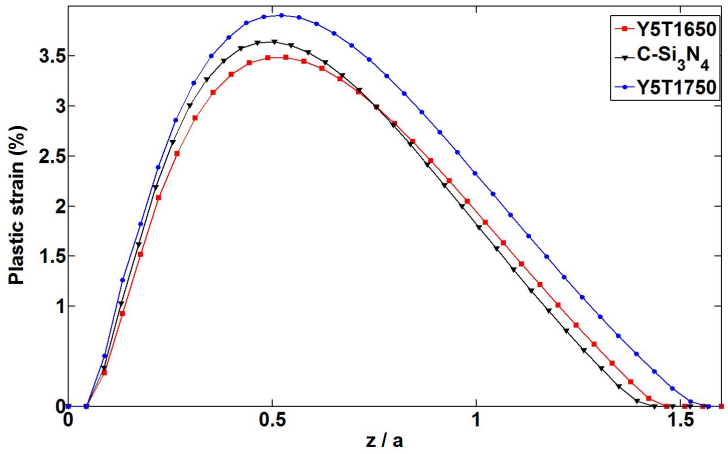

FIGURE 3.23: Evolution of the plastic deformation as a function of the sintering temperature under vertical loading , P = 45 N and R = 0.2 mm

(A). At the end of the rolling loading, the size of this zone is found to be greater than 6 times the elastic contact, see FIG.3.25 (B).

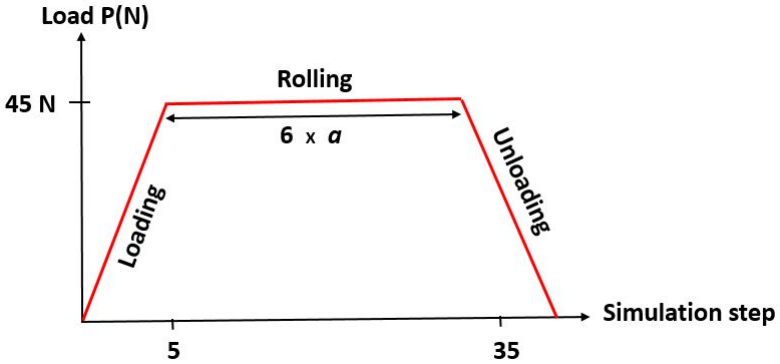

FIGURE 3.24: Loading steps in the numerical simulations of rolling over Si_3N_4 specimens

With this in mind, we have picked out the maximum of the equivalent plastic strain at each time increment of the simulation. It was found that the vertical position for this maximum is close to that predicted by the Hertz theory, $z = 0.47\ a$, the result is plotted in FIG.3.26. One can notice four distinct parts in these curves : in the first domain, the stress field in the solids is purely elastic. When the von Mises equivalent stress is higher than the material yield stress σ_y, then maximum of ε_p increases with increasing the applied load. Once the maximum load is reached, i.e 45 N, the motion of the ball starts in the horizontal direction and ε_p increases further. It is interesting to note that the increasing rate of ε_p varies significantly from material to material. After the maximum of deformation is reached, a steady state is obtained when the rolling distance is higher than 4 times the contact radius. Finally, the unloading step is carried with no variation of the plastic strain.

Even if the curve profiles are similar for the three materials considered in the simulation, it can be noticed that the residual deformation strongly depends on the grain sizes. In fact, more than 6% of plastic strain is achieved for C-Si_3N_4 while the maximum is only about 3.5% for F-Si_3N_4. Finally, M-Si_3N_4 behaviour is intermediate to these two cases with 4.5% of maximum plastic strain. Although a single pass was simulated, one could argue that the resistance of the Si_3N_4 to rolling contact fatigue is significantly different from one microstructure to another.

Concerning referenced materials Y5T1650, C-Si_3N_4 and Y5T1700, because of the close values obtained for the elastoplastic parameters (TAB.3.4), a very similar response for the three materials under the rolling conditions outlined above is expected. Figure 3.27 illustrates the evolution of the maximum plastic strain ε_p. It can be seen that varies by about 15 % from a material to another, the maximum is obtained for Y5T1750, sintered at 1750 °C. This is consistent with the fact that this material has the lowest yield strength. Here, we clearly observe the effect of rolling on the damage accumulation. While the materials are equivalent after pure vertical load, one can note a significant difference at the end of the rolling simulation.

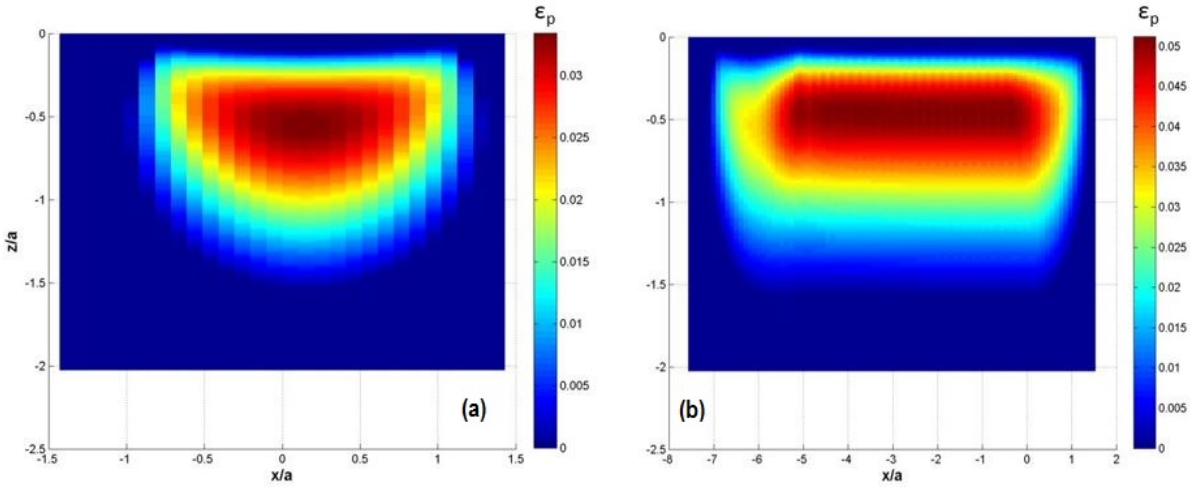

FIGURE 3.25: Evolution of the plastic zone under : (a) vertical loading, (b) rolling over a distance of 6 times the contact radius. Simulations were performed using sphere of radius R_1 = 0.2 mm at load P = 45 N

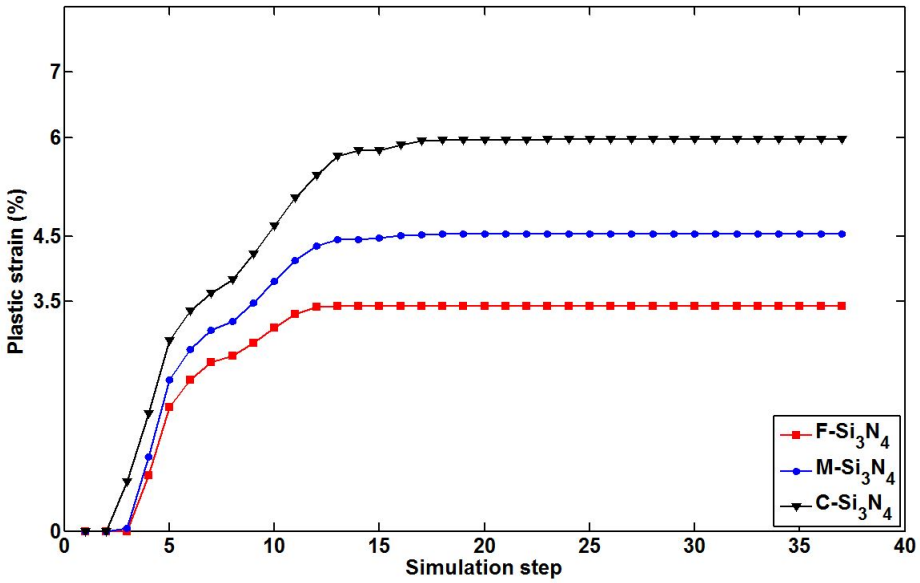

FIGURE 3.26: Evolution of the plastic deformation

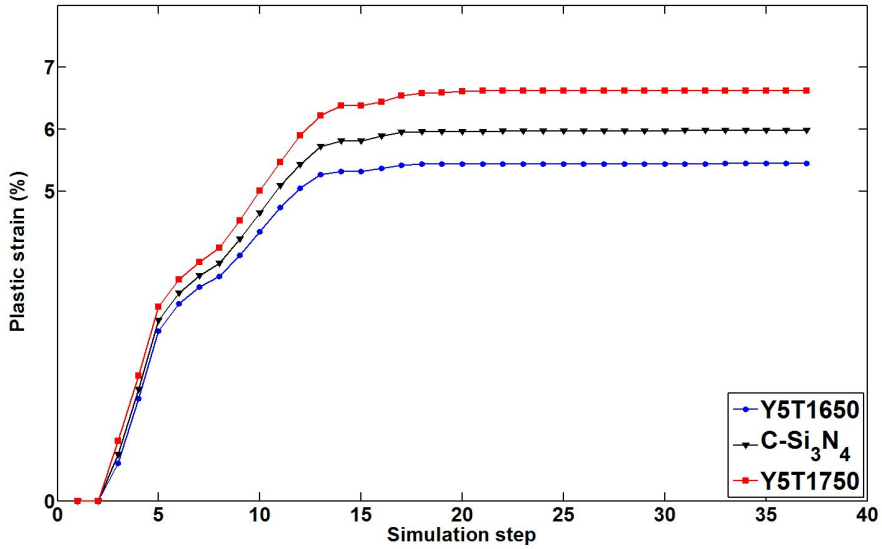

FIGURE 3.27: Evolution of the plastic deformation as function of the sintering temperature

3.5 Conclusions

Fully dense silicon nitride ceramics with different grain sizes were processed using spark plasma sintering technique at temperature of 1700°C with addition of 1, 3 and 5% of Y_2O_3. A gradual evolution from materials with fine equiaxed α grains to microstructures containing large elongated β grains was observed. Significant effect of the processing conditions such as temperature and aid amount on the mechanical properties was also noticed. The mechanical behaviour at small scale was investigated using indentation testing technique with spherical diamond tips. Load versus displacement indentation curves were coupled with identification algorithm to take into account the non-linear part of the mechanical behaviour. A good agreement is found between the measured elastic modulus and the calculated one.

The yield stress σ_y significantly depends on the grain size and high values were obtained for the hardening parameter K. The identified parameters were afterwards used to simulate the mechanical response of materials under vertical or rolling loadings. It was numerically demonstrated that these latter conditions enlarge the damage zone independently of the material microstructure.

Finally, Hertzian contact tests at macroscopic and mesoscopic scales were performed to investigate damage modes at the surface and beneath the indents. Experimental observations revealed a remarkable size effect in the damage mode for coarse microstructure : fracture at large scale and quasi−plastic deformation at smaller scale. In addition, the transition radius for a coarse silicon nitride microstructure was experimentally obtained. The mechanisms at small scale were investigated by means of focused ion beam and transmission microscopy. They consist of distributed short cracks in addition to dislocation motion due to slip system activations.

Chapter 4

Porous Silicon nitride

The purpose of this last chapter is to introduce the particular case of porous silicon nitride materials. They were obtained by sintering at pressure lower than required for a full density. The results about the microstructures are reported and the influence of porosity content on the mechanical properties are analysed. The damage mechanisms at the surface and subsurface levels are presented and discussed. In addition, numerical simulations on the size effect in contact damage are performed. Finally, the indentation stress-strain and true uniaxial stress-strain curves were obtained and analysed.

Contents

4.1 Materials

4.1.1 Microstructure

Materials with three different degrees of porosity volume content were obtained depending on the imposed uniaxial pressure during the sintering process. The temperature profile and the sintering hold time were the same for all the materials, 1700°C and 15 min, respectively. As previously reported, the batch A (95% Si_3N_4 + 5% Y_2O_3) sintered under a pressure of 40 MPa led to fully dense specimen showing no residual pores. It will be considered as the reference material in the subsequent study. On other hand, the specimens from powder mixtures B (95% Si_3N_4 + 5% Y_2O_3) and C (99% Si_3N_4 + 1% Y_2O_3) sintered under 20 and 10 MPa respectively showed 3 and 18 % of residual pores (TAB.4.1). This porosity is defined as :

$$\phi = 1 - \frac{\rho_{exp}}{\rho} \tag{4.1}$$

Where ρ_{exp} and ρ are the experimental and theoretical densities, respectively.
The sintering pressure plays an important role in the powder consolidation. Therefore, insufficient pressure leads to an incomplete densification of the starting batches.

TABLE 4.1: Materials and corresponding processing conditions

Material	Yttria,wt %	Pressure (MPa)	Porosity ϕ (%)
A	5	40	0
B	5	20	3
C	1	10	18

Optical micrographs of the material surfaces under $\times 20$ objective combined with a quantitative processing of the acquired data using commercial ImageJ software revealed that the voids are of irregular shape and random spatial distribution in the materials with 3% and 18% of voids, the observations are shown in FIG.4.1. The random distribution of the residual cavities allows to assign an isotropic behaviour to materials considered in this chapter. This distribution is due to the fact that no pore morphology control was made and the incomplete densification results exclusively from the insufficient pressure applied during the sintering process of the starting batches. Increased pore interconnectivity was also observed for the materials with the highest amount of porosity, i.e. material C. In addition, it is found that the size of the largest cavities in both materials ranges between 1 and 2 μm. This results will have a major importance in indentation tests as it will be discussed somewhat later.

Figure 4.2 shows scanning micrographs of the porous Si_3N_4 specimens after chemical etching with NaOH at 500°C for 10 seconds. One can observe that the two porous materials, i.e, B and C, exhibit a relatively similar microstructure features. These latter ones consist of randomly oriented rodlike grains with high aspect ratio ($\geq$ 10 from the photographs in FIG.4.2) embedded in a glassy phase. Materials B and C have approximatively the same grain size even if the mechanisms behind the elongated grains are quite different. In fact, in material B, the elongated grains result from the $\alpha \rightarrow \beta$ phase transformation leading to grain growth and rearrangement at elevated temperatures. These transformations mechanisms were enhanced by the relatively large amount of Y_2O_3 (5%)

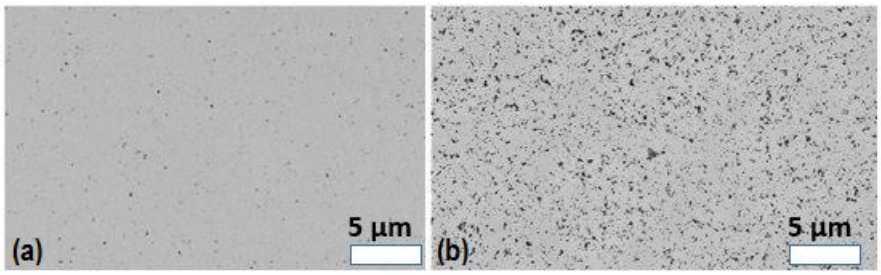

FIGURE 4.1: Surface porosities in Si_3N_4 sintered at 20 MPa (a) and 10 MPa (b)

and elevated temperatures used in the sintering process. Regarding the material C, the grain growth was not impeded by the insufficient pressure applied. Because of this similarity in microstructure features, the difference in mechanical properties and behaviour under contact conditions will be as first approximation attributed to the residual porosity content. However, one has to keep in mind that the other microstructural parameters such the glassy phase for example may play a role on mechanical properties values.

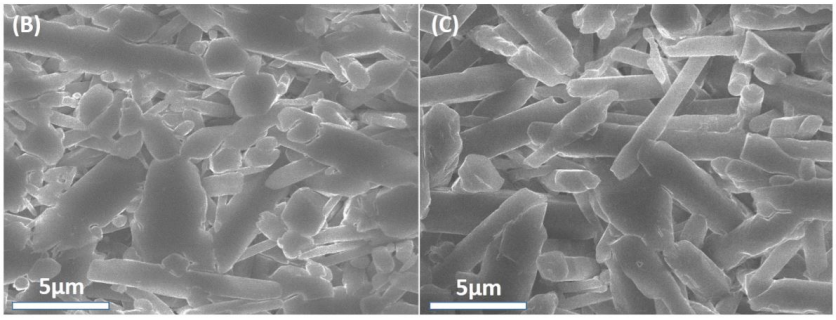

FIGURE 4.2: Microstructure of silicon nitride materials with 3 % (a) and 18% of pores (c)

In addition to the microstructural aspects, the fracture surface of materials B and C were also observed under electronic microscopy to reveal the different fracture mechanisms of these materials. The micrographs are shown in FIG.4.3. Note that the presence of 3% of pores does not radically change the surface texture when compared to the dense materials of chapter 3.

4.1.2 XRD

The last step on the characterization of the microstructure consists of determining the phase composition. X−ray measurements followed by a phase identification revealed that materials A and B have the same diffraction pattern, whereas material C shows a slightly different pattern (see FIG.4.2). Concerning the phase composition, $\alpha-Si_3N_4$ is less present in material C with 18% of porosity, while $\alpha \rightarrow \beta$ phase transformation was enhanced for the specimen with 3% of porosity leading to more β grains. We can therefore attest the fact that the phase composition is more significantly related to the amount of yttrium oxide used to process the materials, here 5 and 1 % than the sintering pressure which had no significant effect on the phase content.

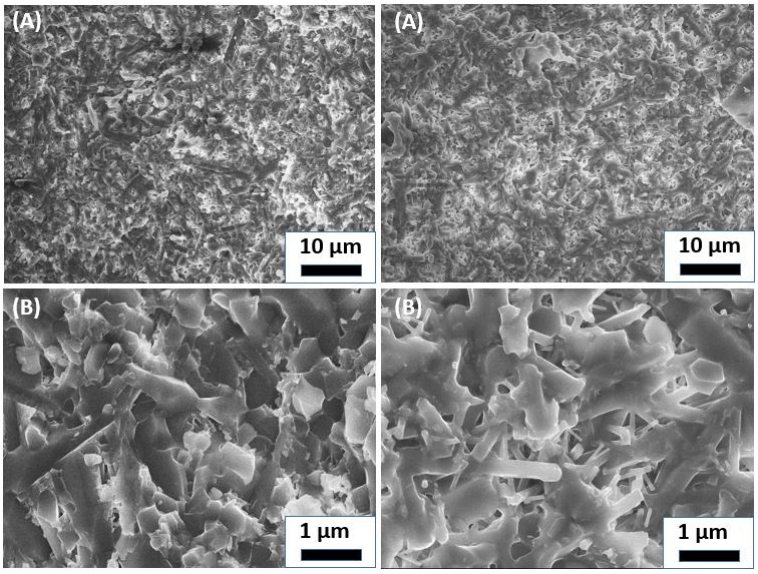

FIGURE 4.3: Fracture surface in materials with 3% (left) and 18% (right) porosity volume content at different magnifications : (A) ×1000 and (B)×5000

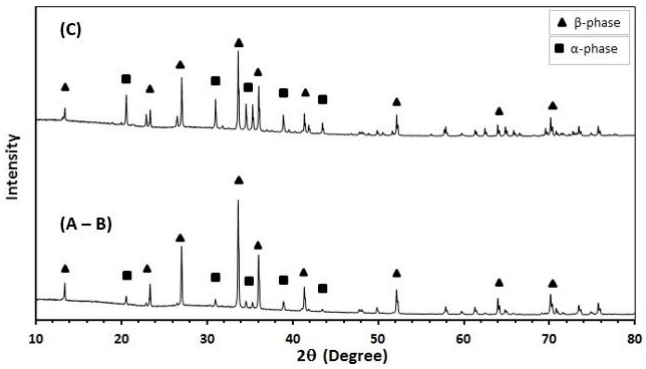

FIGURE 4.4: X-ray diffraction patterns of SPSed silicon nitride with different porosity content

4.2 Mechanical properties

4.2.1 Effect of the porosity content

The experimentally measured bulk density, porosity fraction, Young's modulus and Vickers hardness of materials A, B and C are reported in TAB.4.2. The bulk density ρ linearly decreases with increasing the porosity volume content ϕ. Consequently, the density of the Si_3N_4 specimens can be estimated by a simple mixture law as follows : $\rho = \rho_o(1-\phi)$ where $\rho_o = 3.25$ g/cm^3 is the porosity of the dense material A. One can also notice that the elastic modulus E and the Vickers hardness of the Si_3N_4 specimens strongly depends on the porosity, ϕ. In fact, E and H decreases by about 50 % from their maximum values of 317 GPa and 1580 Hv (material A, zero porosity) to their minimum values of 170 GPa and 725 Hv (material C, 18% porosity). Even if they are not reported here, there is a strong likelihood that the other mechanical properties such the flexural

strength and fracture toughness to be significantly impacted [Diaz and Hampshire, 2004].

TABLE 4.2: Density and mechanical properties of porous silicon nitride specimens

Porosity ϕ	Density (g/cm^3)	Elastic modulus (GPa)	Poisson's ratio	Hardness (Hv)
0	3.25	317	0.27	1580 $\pm$14
0.03	3.16	282	0.25	1219 $\pm$7
0.18	2.69	170	0.22	725 $\pm$23

4.2.2 Data regression

Several empirical and semi empirical models based on the minimum solid area (MSA) concept have been proposed to predict the effect of porosity on the elastic properties of brittle bodies. Other models combining the porosity volume fraction and phase composition of the silicon nitride ceramics have been also proposed [Yeheskel and Gefen, 1985]. In the current work, we consider the three following models, with two adjustable parameters, widely used in the literature for moderate porosity volume fraction range, $0 < \phi < 0.3$:

(i) A Linear empirical approximation proposed by Dean and Lopez [Dean and Lopez, 1983]

$$E = E_0 (1 - h\phi) \tag{4.2}$$

(ii) An empirical exponential relation by Spriggs [Spriggs, 1961]

$$E = E_0 exp(-b\phi) \tag{4.3}$$

(iii) A semi− empirical power law based on the work of Phani and Niyogi [Phani and Niyogi, 1987a]

$$E = E_0 (1 - c\phi)^n \tag{4.4}$$

Where E and E_0 are the elastic moduli at porosity ϕ and zero respectively. The positive constants h, b, c and n are related to the studied material. The parameters of each model could be determined from experimentally obtained results by performing data fitting [Luo and Stevens, 1999]. For the considered silicon nitride materials, the identification of early mentioned parameters was performed using the Excel solver which is based on generalized reduced gradient algorithm (GRG2) for non-linear problem optimization.

The results of the fitting procedure are presented in TAB.4.3. We can remark that the experimental elastic modulus data are well fitted by the three models considered in this work. The mean error reached in the regression process is found to be less than 2%. From χ^2 values, the best approximation of the considered mechanical properties was obtained when considering the exponential model (Eq.4.3) with a mean error of 0.7 %. Zero−porosity moduli E_0 values obtained with the three models are nearly the same. In addition, they are in very good agreement with the experimental Young's modulus of the fully dense material A reported previously (E_A = 317 GPa). It is found that the best fitting of the experimental data is obtained for Eq.4.3 with $b = 3.42$ and E_0 = 314 GPa. A theoretical value of b = 3 is expected for spherical voids with an ideal packing geometry [Rice, 1998]. The deviation from this exact value (+ 11 %) is probably because

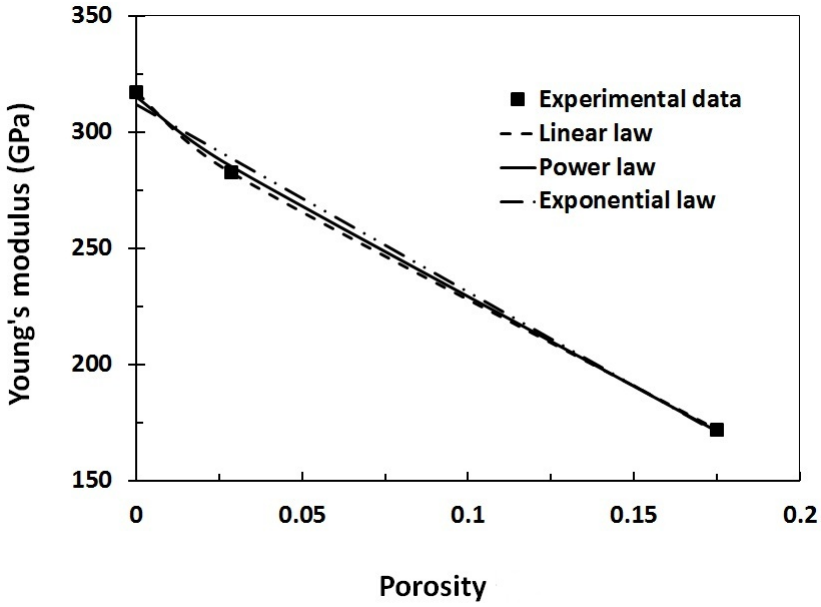

FIGURE 4.5: Experimental and estimated values of Young's modulus as function of porosity volume fraction

TABLE 4.3: Summary of parameters of regression models

Equation	E_0	Other parameters	Mean error (%)	χ^2 value
$E = E_0 (1 - h\,\phi)$	311	h = 2.58	1.5	65
$E = E_0 \exp(-b\,\phi)$	314	b = 3.48	0.7	10
$E = E_0 (1 - c\,\phi)^n$	313	c = 1.00	1.0	25
		n = 3.16		

of the non−spherical geometry of pores, their random spatial distribution within the bulk body of the samples and finally due to the limited number of points used for the regression process. Concerning the equation 4.4, the value $c = 1$ confirms the random spatial distribution of grains in the materials. Regarding the other parameters i.e. h and n, they are in same range of values than those reported for porous silicon nitride materials [Diaz and Hampshire, 2004, Phani and Niyogi, 1987b]. In fact, the author obtained values for h ranging from 2.11 to 3.11, and for n ranging from 1.21 to 2.56.

The influence of the porosity on hardness values is generally approximated by a relation similar to Eq.4.3 with H_0 corresponding to the hardness of the fully dense material A and b as fitting parameters.

Using the same data fitting procedure, final values of 1502 Hv and 4.42 are obtained for H_0 and b, respectively. The mean error in data regression is found to be less than 6%. We can also notice that H_0 is in very good agreement with the hardness of dense material A (1580 Hv) as expected. The value obtained for fitting coefficient b is larger than the theoretical value of 3 but it

is coherent with values ranging from 3.1 to 5.7 reported in the literature for hot-pressed and hot isostatic pressed silicon nitride bodies [Rice, 1998].

Finally, increased porosity slightly affected the Poisson's ratio ν, which showed values of 0.25 and 0.22 for 3% and 18% porosity, respectively. However, it is well-known in the literature that both a reduction of the Poisson's ratio [Rouxel et al., 2008] and increase of the porosity may enhance the densification capability of brittle materials.

4.3 Brittle to quasi-plastic transition

4.3.1 Macroscopic scale

In this section, we propose a study of mechanical response of sintered materials under pure vertical contact loading. The optical half-surface and side views of Hertzian contact damage on material B and C are reported in FIG.4.6 after single indentation testing with a sphere of radius 1 mm at peak vertical load P = 500 N. Material B with 3% of porosity content showed several deep circular ring cracks. They initiate outside the contact site then extend into cone cracks propagating downwards. The mechanisms are similar to those already reported for fully dense brittle materials. In addition to surface cracks, one can notice some damage accumulation below the contact zone. On the other hand, for the material with 18% porosity volume content, a clear depression was observed without any evident of fracture at the surface. A significant deformation of half hemispherical shape extends beneath the indent. It can be also observed a pronounced crack at the boundary between the damaged area and the undamaged one. According to Latella *et al.*[Latella et al., 1997], the crack is due to the material compaction during loading then it is pulled out because of the large elastic recovery during the unloading step.

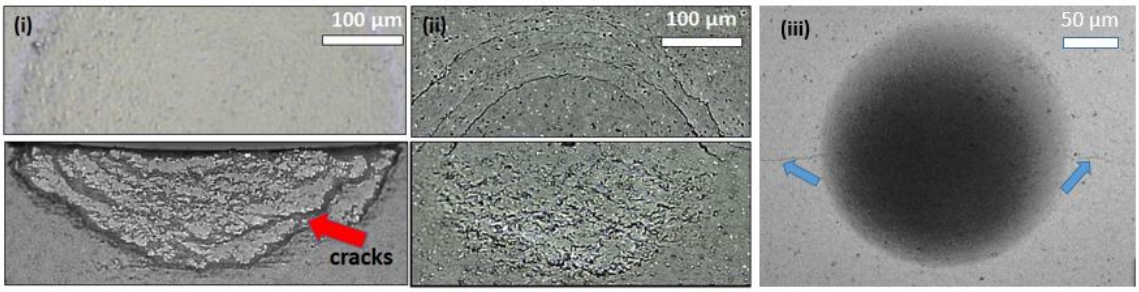

FIGURE 4.6: Optical micrographs of surface and subsurface contact damage in silicon nitride materials with porosity (i) 18% and (ii) 3% under maximum load of 500 N, (iii) specimen with 18% of porosity under 750 N. Indentation tests were made by diamond sphere of radius R_2= 1 mm

Both surface and subsurface damage mechanisms are intimately related because of stress redistribution. Figure 4.7 shows the radial stress field σ_{rr} at the surface of the Si_3N_4 porous materials previously introduced. The numerical simulations were performed with Abaqus software with taking into account the nonlinear part of the mechanical behaviour due to the subsurface damage, more details are given in section 4.4.2. The applied load and indenter radius correspond exactly to the experimental conditions, 500 N and 1.0 mm, respectively. One can observe that tensile stresses (positive part) are released for 18 % of porosity volume content when compared to the less porous material. In fact, a decrease of about 10% of the maximum stress value is observable. This has the

effect of delaying the initiation of surface ring cracks when increasing the porosity volume content in brittle materials.

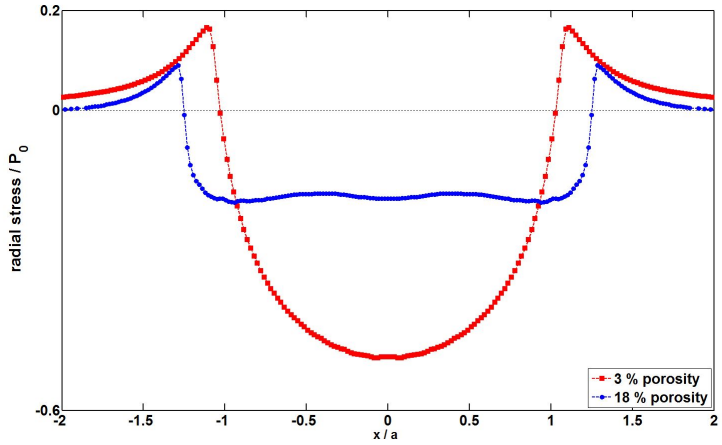

FIGURE 4.7: Radial stress distribution at the surface of the porous silicon nitride materials

If the maximum applied load is increased further, up to 750 N, optical observations of the contact sites revealed the initiation of ring and radial cracks (FIG.4.6 (iii)). Finally, it should be noted that the catastrophic failure of the specimens from instantaneous cracks initiation and propagation occurred at 1700 N and 1200 N for materials B and C. Thus, the failure loads correspond to maximum contact pressure of 23.3 and 17.7 GPa , respectively.

Repeat loading under maximum force P = 500 N of diamond ball of radius R_2 = 1 mm have been performed on the highly porosity material, i.e. with 18 % of porosity content. First, we can observe that no cracks are present at the surface and thus independently of the number of cycles n. However, for n = 8, more damage consisting of pore increased interconnectivity on the sides of the surface impressions can be noticed (FIG.4.8 (ii)).

Using a laser profilometer VK100, the residual indent profiles after n = 1, 4 and 8 could be determined and plotted. it is found that the measured maximum depth was about 5 µm after one cycle and 6 µm after 4 cycles. On the other side, the contact radius is almost constant. If the number of cycles is increased up to 8, no additional surface depression was measured (FIG.4.8 (iii)). This phenomenon can be attributed to a complete pore closure and full material compaction after only few cycles.

Finally, additional contact tests were performed at gradually increased peak load, P = 50, 80 and 100 N using the spherical ball of radius R_1 = 0.2 mm. The indent profiles are shown in FIG.4.9. We can observe that the contact radius and the maximum surface depression continuously increase reflecting an increasingly important damage accumulation. In fact, it is found that the maximum depth is 2, 4.5 and 6.5 µm , and respectively. We can therefore conclude that the maximum applied load is more on the contact critical damage accumulation than a moderate number of cycles.

4.3.2 Mesoscopic scale

The subsurface damage in the porous materials B and C (3 and 18 % of porosity, respectively) was investigated by means of the FIB sectioning technique described in chapter 2. The

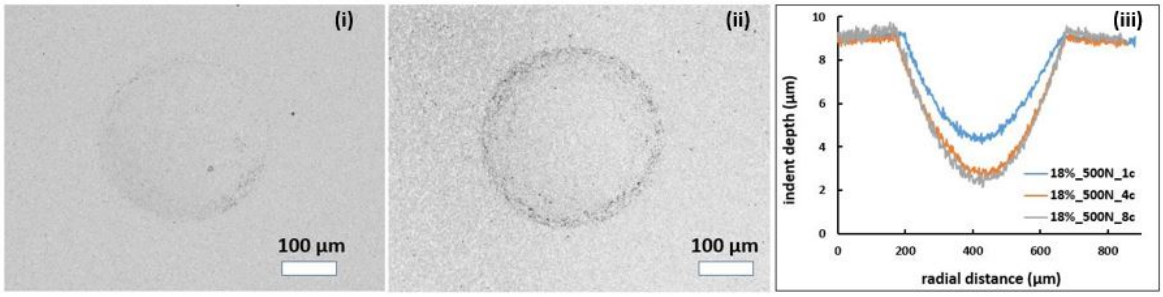

FIGURE 4.8: Effect of cycling on the surface damage and indent depth of 18% porous Si_3N_4 under P= 500 N : (i) single cycle, (ii) 8 cycles, (iii) residual indent profiles

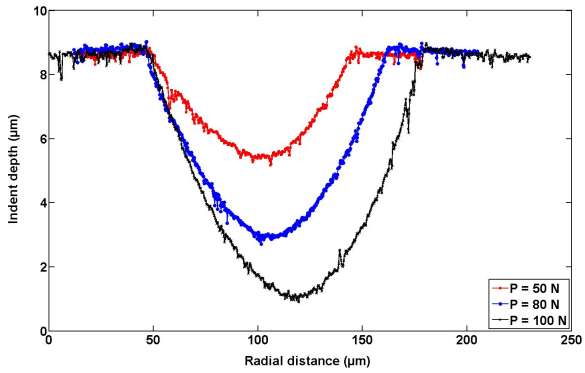

FIGURE 4.9: Effect of increasing the applied load on the indent profile

observations were carried out on polished silicon nitride specimens free of indents and the results are shown in FIG.4.10. One can observe no evidence of crack initiation or propagation at the subsurface sections. Therefore, the evolution of the damage will be strictly attributed to stresses generated by the contact loading.

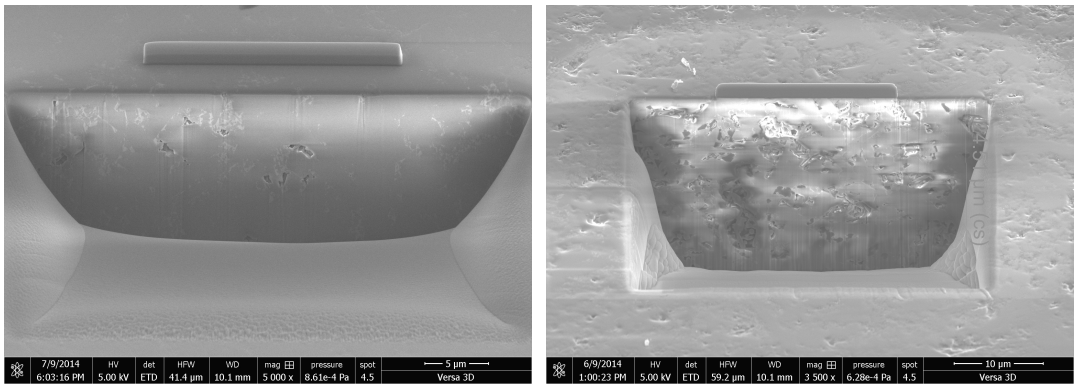

(a) 3 % of porosity content (b) 18 % of porosity content

FIGURE 4.10: FIB observation on porous silicon nitride free of indents

The damage under loading was investigated using the diamond sphere of 0.2 mm radius at peak load P = 45 N. The corresponding maximum contact pressure is 23.2 GPa for 3% of porosity and 17.4 GPa for 18% of porosity volume content.

The observations under residual indents are shown in FIG.4.11. One can remark that the subsurface damage in the low porosity material B consists of few short cracks departing from the pores and the weak intergranular glassy phase at grain boundaries. The observed area remains smooth showing no evidence of densification. Regarding the more porous material C, evident densification can be observed in addition to microcracks. Due to this densification, the surface depression is more pronounced for 18% porosity with a maximum depth of 3 µm compared to only 1 µm for 3% porosity, see FIG.4.12. The microcracks are mostly inclined in the direction of maximum compressive stress [Sammis and Ashby, 1986] and initiate from the existing pores. The short cracks extend stably, deviate towards each other then coalesce to from a long macroscopic crack which propagation leads to a catastrophic failure of the specimen, see FIG.4.11. It should be mentioned that no cracks were observed at the surface and thus despite the high pressure applied, P_0=23 and 17 GPa on material B and C, respectively.

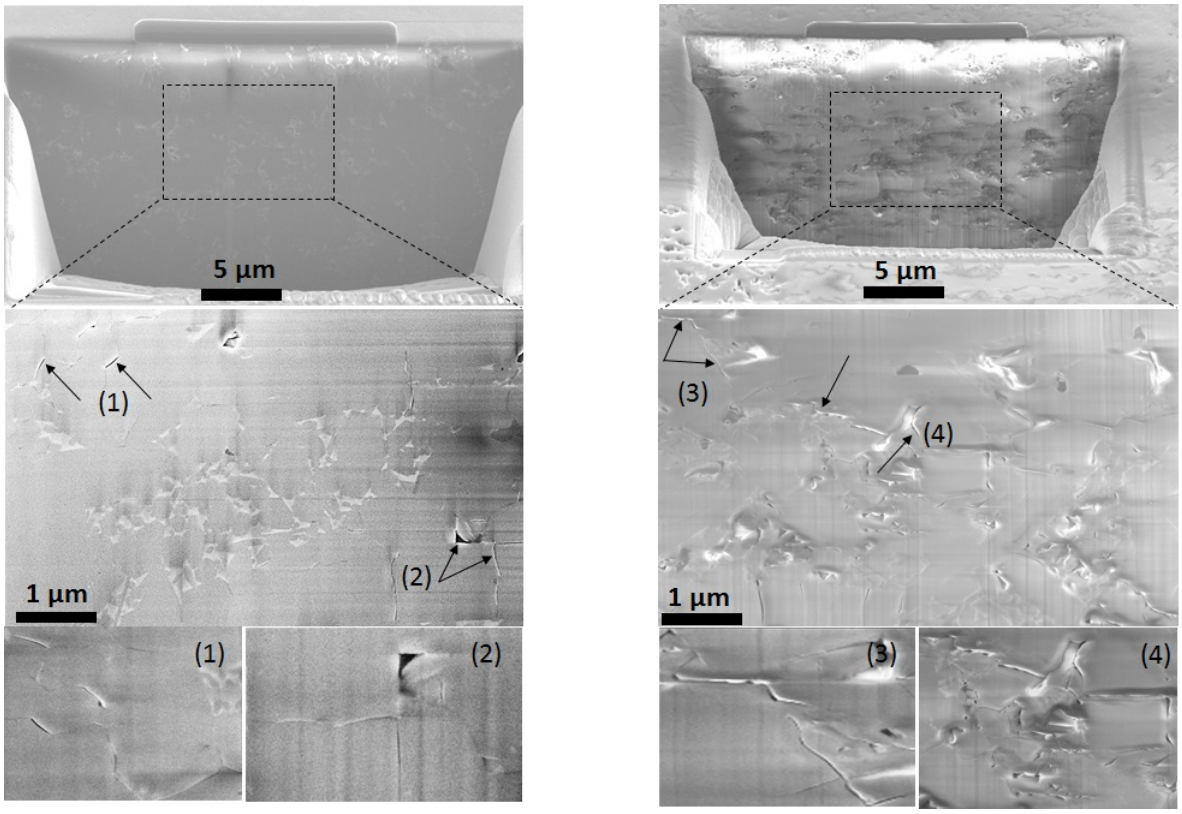

FIGURE 4.11: Subsurface damage after indentation with a sphere of 0.2 mm radius under 45 N for materials with 3% (left) and 18% of porosity content

The damage was also investigated after 8 loading-unloading steps up to 45 N on diamond sphere of radius 0.2 mm on silicon nitride wtih 18% of porosity, the FIB observations are shown in FIG.4.13. Although the texture of the surface is not very different from that of a monotonic loading,

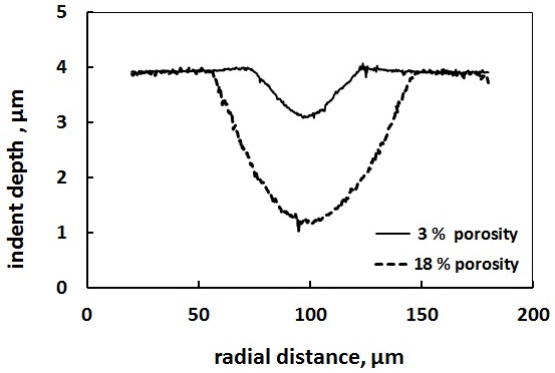

FIGURE 4.12: Indent profile for material 3 and 18 % of porosity content under 45N

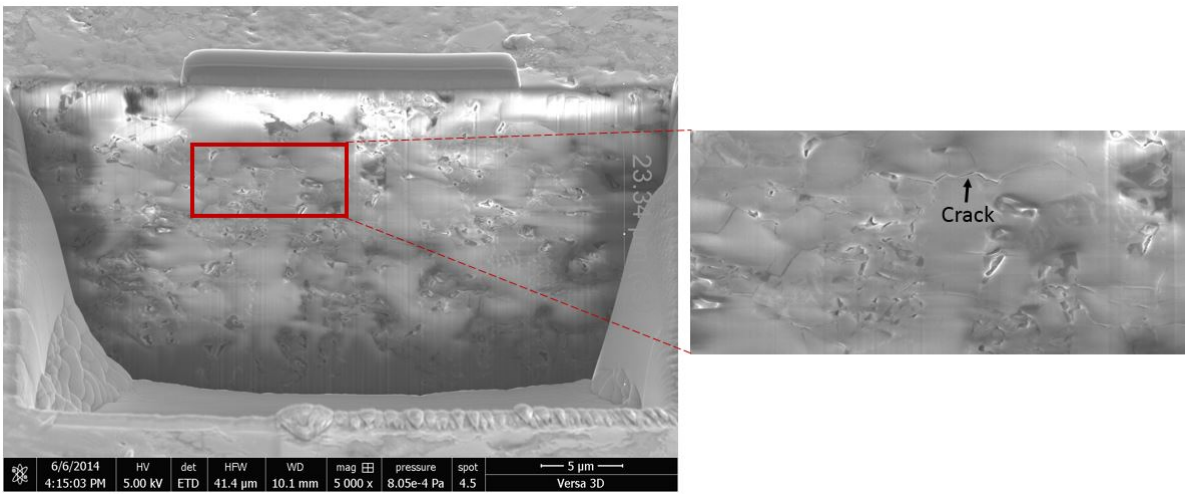

FIGURE 4.13: Subsurface damage in silicon nitride under 8 cyclic loading under 45 N on sphere radius of 0.2 mm

longer cracks parallel to the sample surface are apparent. If the number is increased further, one expect these cracks to extend then lead to material removal or failure of specimen.

The numerical simulation conducted considering a distribution of voids can give some explanation about the damage under contact sites. Of course, this is a simplified academic case with a spherical geometry shape and a uniform spatial distribution of the pores. These geometrical simplifications have been deliberately introduced in the model to reduce the total computation time. However, the presence of cavities and taking into account the mutual interactions are expected to have an important impact on the different stress fields in the massive and provide useful insights about the damage development. Thereafter, a cluster of $10 \times 5 \times 3$ inclusions was generated in an isotropic elastic half space. More details about the semi-analytical model used to solve the contact problem will be provided in the following sections.

The influence of the residual porosity is clearly illustrated for example in case of von Mises equivalent stress, see FIG.4.14. We recall below the maximum Hertzian value for σ_{VM} when consi-

dering only elastic homogeneous materials with Poisson's coefficient $\nu = 0.3$:

$$\sigma_{VM} = 0.62\, P_{Hertz} \tag{4.5}$$

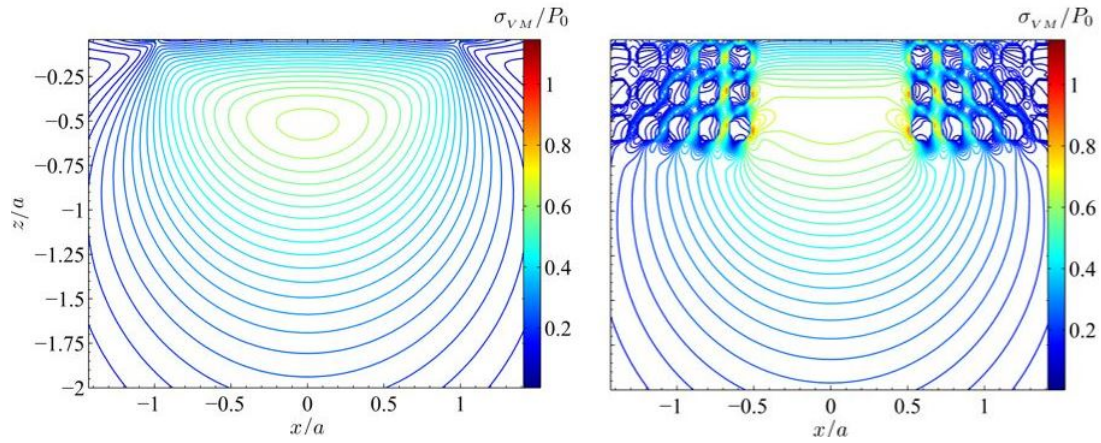

(a) homogeneous (b) porous

FIGURE 4.14: Equivalent von Mises stress distribution for homogeneous (a) and porous materials (b)

This theoretical value is in very good agreement with the numerically simulated one in case of the non-porous material. For the inhomogeneous case, it may be noted that the maximum value of the equivalent stress is highly magnified. Indeed, an increase up to 100 % was calculated for σ_{VM} at the matrix / pore interface as shown in FIG.4.14. Thus, it is conceivable that this over-stressing generate short cracks departing from the pores within the solid as it was experimentally observed using FIB cross sectioning.

4.3.3 Size effect

4.3.3.1 Experimental results

Indentation using spheres of two different radii revealed a significant size effect : at the macroscopic scale, ring crack initiation and propagation were observed at the top surface of the porous materials after indentation by a large sphere. In addition, significant damaged areas were observed under the indents. At the mesoscopic scale, i.e. for small indenting spheres, the damage mode consists of microcraking at the subsurface level while the surface remained free of cracks. The size effect was also evidenced by the capability of the porous specimens to withstand higher contact pressures for reduced indenter radius. The formula 'smaller is stronger' widely used for metals [Maass et al., 2009] is still valid for brittle materials, even if the mechanisms behind are quite different. For ductile materials, lattice defect (dislocation motion) reductions when the specimen become smaller and smaller is behind this behaviour. For the specific case of porous brittle materials, such behaviour can be attributed to two different mechanisms. The first concerns the probability $\mathcal{P}$ of meeting a critical defect which size and / or spatial orientation at the surface generate enough stress concentration to initiate cracking. It follows that volume of solicited material

is one of most critical parameters in determining the mechanical strength. $\mathcal{P}$ is generally related to the specimen volume thanks to Weibull theory for example. Unfortunately, this theory can not be used in the case of contact conditions because of the complexity of the stress field, but it is then obvious that the failure probability increases with increasing the indenter size.

The second hypothesis that may explain the size effect in damage mode considers the influence of the contact size on the radial stress field σ_{11} in presence of porosities. As mentioned earlier, σ_{11} positive (tensile) at the surface controls the initiation of classical ring cracks

4.3.3.2 Numerical simulations

A robust three dimensional semi-analytical code developed in the laboratory where interactions between inclusions are taken into account was used to run the numerical simulations. Because it is practically impossible to model the real geometry of pores and to reduce the cost of the 3D numerical calculation, we have considered the academic case of spherical holes uniformly distributed along the three directions *x*, *y* and *z*.

Two configurations were generated (see FIG.4.15) with a total number of 50 inclusions with a radius r=1 µm and spacing between two neighbouring inclusions d= 6 µm : the first one with R_1 = 0.2 mm and P_1= 45 N corresponds to the case of small diamond indenter (mesoscopic scale) while the second configuration with R_2 = 1.0 mm and P_2= 1125 N corresponds to the case of large indenter (macroscopic scale).

To consider only the scale effect in the problem, the corresponding maximum contact pressure P_{hertz}=23.2 GPa resulting from the applied loads P_1 and P_2 is the same (for ideally homogeneous material). The elastic properties are also similar in both configurations with E = 282 GPa, ν=0.3 for Si_3N_4 materials and E = 1141 GPa, ν=0.07 for the purely elastic spherical balls considered in the simulations. It should be added that no crack initiation and propagation criteria was introduced.

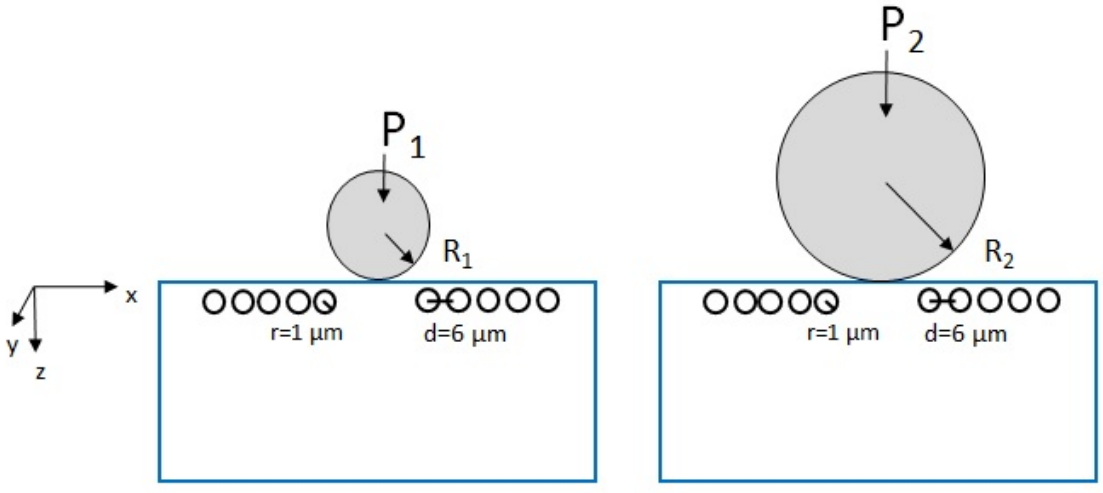

FIGURE 4.15: Configurations considered in the numerical simulation

Figure 4.16 represents the distribution of radial stress σ_{11} for the two configurations introduced above. The stress and distance from the contact center were reduced by P_{hertz} and the elastic contact in the two configurations, respectively.

It is found that the maximum of σ_{11} increases by 10 % for the larger indenter sphere. This over-stressing is due to the fact that, for the small indenter radius, the spherical porosities are located in an area with a sharp stress gradient, whereas for the larger indenter radius the size of the porosity becomes smaller relatively to the contact size, leading to porosity located in a more uniform and slightly higher stress field, which in turns produces higher stress concentration.

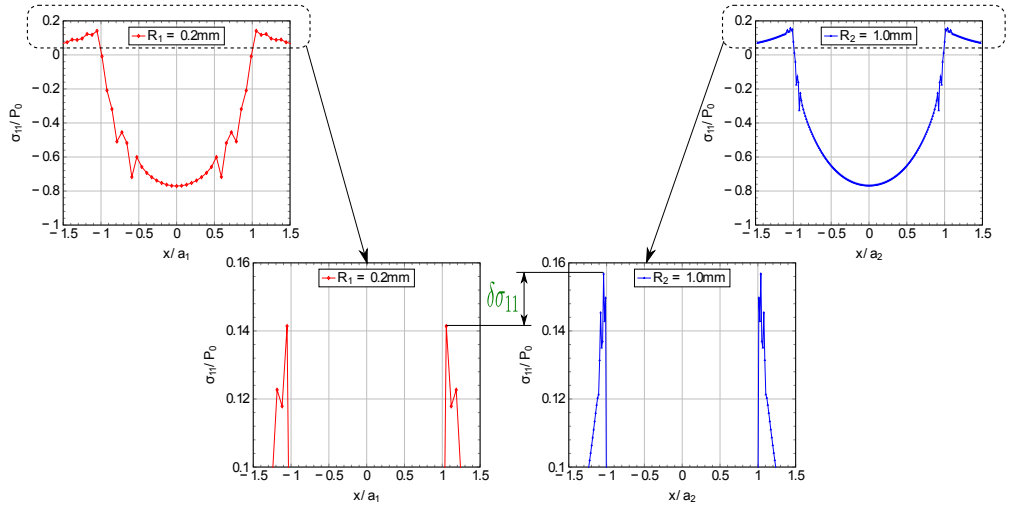

FIGURE 4.16: The obtained profile of the radial stress in the porous material for the two indenter radii

4.4 Mechanical behaviour

4.4.1 Indentation stress-strain curves

The indentation stress−strain curves, i.e. p_0 versus a/R, for single cycle indentation on specimens with 3% and 18% are plotted in FIG.4.17. For comparison purpose, we also reported the results for 37% of porosity from the work of She *et al.*[She et al., 2003] on hot pressed silicon nitride. Concerning the dashed line, it represents the Hertzian relation (linear) for elastic bodies. One can notice a clear deviation from linearity for three porosity contents. A plateau was also obtained in the high strain region, i.e. $a/R \geq 0.1$. It indicates a constant indentation stress in this region. This results from the competition between the stress redistribution in the bulk specimen because of pore collapses under the contact site and progressive increase of the applied load.

It is obvious from the experimental data that the mean contact pressure corresponding to the first deviation point, p_Y, is strongly related to the porosity volume fraction. Combining the critical shear stress criterion and Hertzian theory, it is possible to relate the yield stress Y to p_Y as follows [Rhee et al., 2001, Fischer-Cripps and Lawn, 1996] :

$$Y \approx \frac{p_Y}{1.1} \tag{4.6}$$

The measured Y values from Eq.4.6 are then approximately 10 GPa, 6.36 GPa and 1.5 GPa for 3%, 18% and 37% of porosity content, respectively. It should be noted that these values are in

good agreement with the measured hardness of the porous Si_3N_4, see TAB.4.2. A larger plateau quantified a higher capability of the porous materials to deform without crack initiation. This result confirms the effects of subsurface damage accumulation on the tensile radial stress. In fact, cracks were found to initiate for indentation $a/R \approx 0.15$ and 0.34 for samples with 3 and 18 % of porosity, respectively.

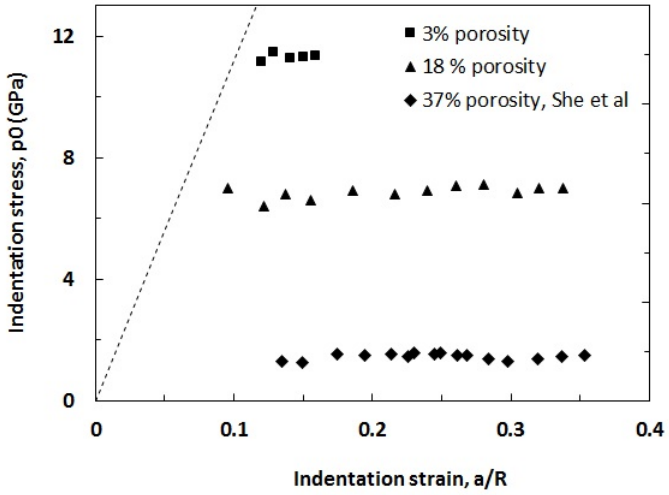

FIGURE 4.17: Indentation stress-strain for the porous materials

4.4.2 Stress - strain curves

Load versus displacement curves obtained by instrumented indentation testing for the porous materials using the diamond spherical tip of 42 µm radius are illustrated in FIG.4.18. The applied load was increased up to 9 N for both materials. The slope of the curves is significantly different for the two materials which is consistent with the reported value of elastic moduli. In addition, the maximum displacement measured is 2.5 µm and 5 µm for 3 and 18 % of porosity, respectively. These curves were averaged over the 25 tests performed on the polished surface of each materials. The first observation is about the curves allure for which no sudden discontinuities due to cracking or other damage mechanisms were noticed.

In addition, one can notice that the residual displacement after complete unloading is significantly higher for 18% then for 3% of residual porosity. Mean values of about 3.5 µm and 1.5 µm were obtained. This results quantitatively demonstrates the higher capacity to undergo locally a permanent deformation and therefore a more pronounced tendency for transition from elastic to elastoplastic behaviour in the mechanical response with increasing the porosity content.

The elastic modulus and hardness values derived from the *P-h* curves using Oliver & Pharr method described in section 2.4.2 are reported in TAB.4.4. They are representative of the materials properties because the size of the indents is large enough when compared to the size of the pores. For comparison purpose, we have also reported values for E and H from standard techniques (ultrasonic measurement and Vickers hardness, respectively). We find the same tendency concerning the influence of pores : the different mechanical properties deteriorate when the porosity content

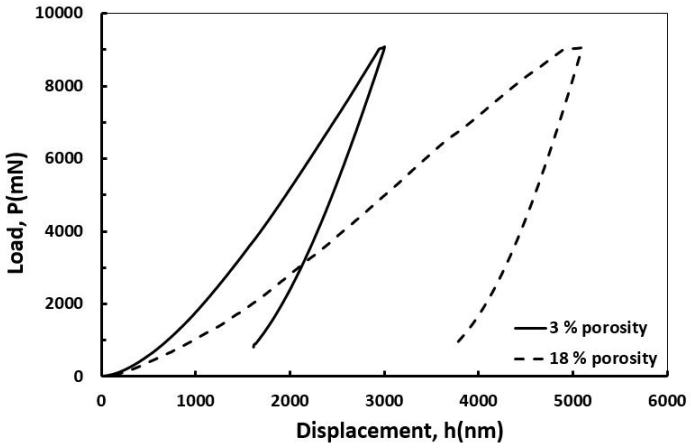

FIGURE 4.18: Effect of porosity on load versus displacement curves

increases. In addition, the low standard deviation values confirms a good reproducibility in the obtained *P-h* curves. The values derived from spherical indentation testing are in very good agreement (mean error less than 5%) with the standard techniques. The low discrepancy observed can be attributed to variation of the indenter radius with increasing the indentation depth.

Figure 4.19 shows the experimental and numerical load-displacement curves for the porous Si_3N_4 materials at the end of the identification process. The elastic response (Hertz fit) is plotted for each material using the identified elastic moduli. Usually the first deviation point is used to derive the plastic parameters of hard materials and to investigate the effect of the porosity volume content on the yield strength for example [Chintapalli et al., 2012]. However this approach requires accurate knowledge of the indenter geometry, which is a difficult task for small depths. The reverse method based on Levenberg-Marquardt algorithm is applied to identify the true $\sigma - \varepsilon$ curves.

The obtained values for Young's modulus E, uniaxial yield stress σ_y and hardening parameter K are reported in TAB.4.5. We report also the constraint factor H / σ_y calculated from the experimentally measured Vickers hardness and identified yield stress.

The identification of the parameters σ_y and K highlighted a gradual loss of stiffness of porous Si_3N_4. In fact, the yield stress sharply decreases when the indented materials become more porous. Concerning the constraint factor, it gradually increases to be close to the value of 3 for the more porous specimens. This demonstrate one again the mechanical transition from a nearly elastic

TABLE 4.4: Elastic modulus and hardness of porous Si_3N_4 materials

Porosity volume content ϕ	3 %	18 %
Hardness$_{sph}$ (GPa)	12.1 $\pm$0.4	6.6 $\pm$0.3
Hardness (GPa)	11.9 $\pm$0.1	7.1 $\pm$0.2
Elastic modulus$_{sph}$(GPa)	263 $\pm$3.7	184 $\pm$3.4
Elastic modulus$_{us}$(GPa)	282	170

behaviour for the dense material to much plastic behaviour without hardening for 18% of porosity content. This trend is confirmed by the sharp decrease of the hardening coefficient K from 44 GPa to a value close to zero.

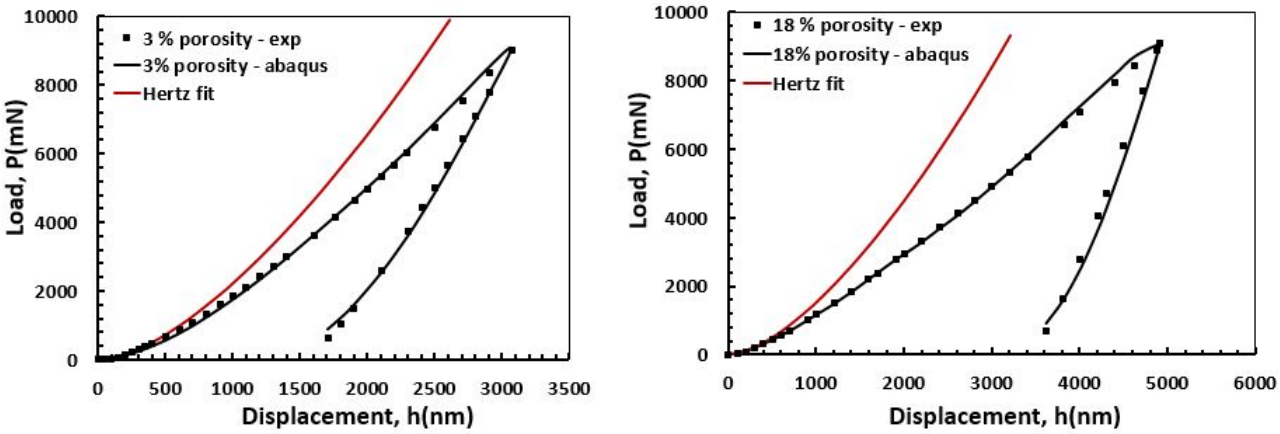

FIGURE 4.19: Experimental and numerical load versus displacement curves after identification for the materials with 3% (left) and 18% (right) of porosity content

TABLE 4.5: Elastic modulus and hardness of porous Si_3N_4 materials

Porosity volume content	0 %	3 %	18 %
E_{id}(GPa)	357 ±1.9	294 ± 0.4	183± 7.9
E_{us}(GPa)	317	282	170
σ_y(GPa)	7. 8± 0.1	5.1 ± 0.2	2.6 ± 0.1
K(GPa)	31.4 ±5.9	44.4 ±1.0	0.8 ±0.6
H / σ_y	2.0	2.33	2.53

We have previously reported that the intensity of the subsurface damage in silicon nitride ceramics strongly depend on the porosity volume content (see FIG.4.6). The evolution of the damage is numerically studied here. In fact, we plot the evolution of the von Mises plastic strain ε_p after complete unloading along the symmetry axis z for the two porous materials (FIG.4.20a). The maximum applied load was 500 N on the spherical indentor of radius R_1. The Plastic behaviour of the Si_3N_4 was modelled with the corresponding identified values of σ_y and K previously discussed. For 18% of residual porosity, the maximum of the damage is about 6 % whereas it reaches only 3% for the material with low porosity. In addition, we must add that value for 3% may be overestimated by the absence of surface ring or cone cracks in the numerical simulation. However, the curves obtained are in good agreement with experimental observations.

In addition to the subsurface damage quantification, we plotted in FIG.4.20b the evolution of the contact pressure profile along the radial axis x in function of porosity volume content. These results correspond to the experimentally applied load, P = 500 N under indenter size R_2 = 1 mm. One can notice from the numerical simulations the significant effect of nonlinear part of

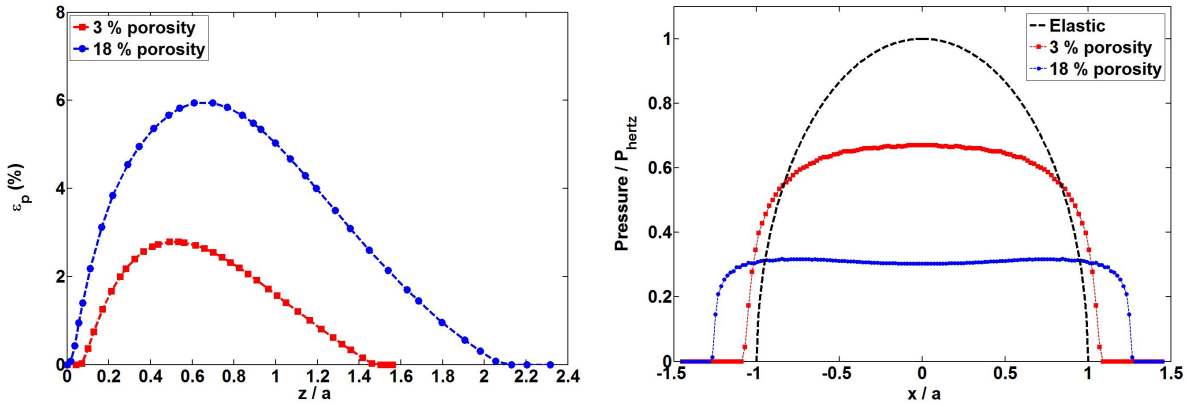

(a) Equivalent plastic strain (b) Surface pressure profiles

FIGURE 4.20: Evolution of the equivalent plastic strain along the axis of symmetry z (a), Pressure profile under a maximum vertical load of 500 N for 3 and 18 % of porosity content (b)

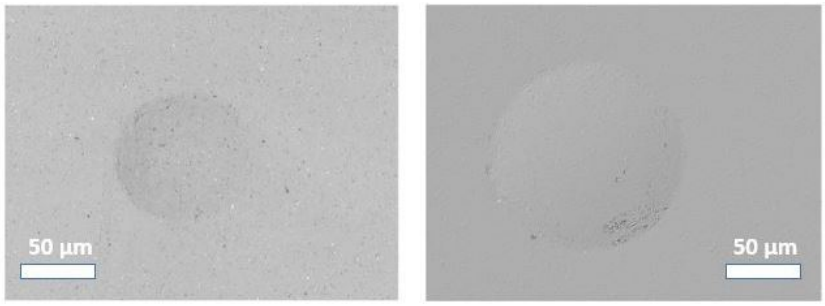

(a) 3 % (b) 18 %

FIGURE 4.21: Contact sites in 3 (a) and 18 % (b) porous silicon nitride after indentation under peak load P=100 N

the mechanical behaviour on the deviation from the theoretical profile. In fact, it is found that the highest value of the contact pressure decreases by a factor 2 when the porosity increases from 3 to 18 %.

To test the identified parameter relevance, we performed contact tests on the porous materials under a pure vertical loading up to 100 N using tip of radius R_1 = 0.2 mm. Figure 4.21 shows the residual impressions after complete unloading. We can notice the absence of surface cracks. This observation result states that only subsurface damage mechanisms were activated under the reported experimental conditions.

Figure 4.22 shows comparison between the experimental and numerically simulated profiles for the two porous materials. The experimental one was obtained by scanning the residual surface impressions. The indentation tests were performed on Instron testing machine using the diamond sphere of radius 0.2 mm under a peak load P = 100 N. In the numerical simulations, the mechanical behaviour of Si_3N_4 was modelled using the identified true $\sigma - \varepsilon$ curves from the inverse

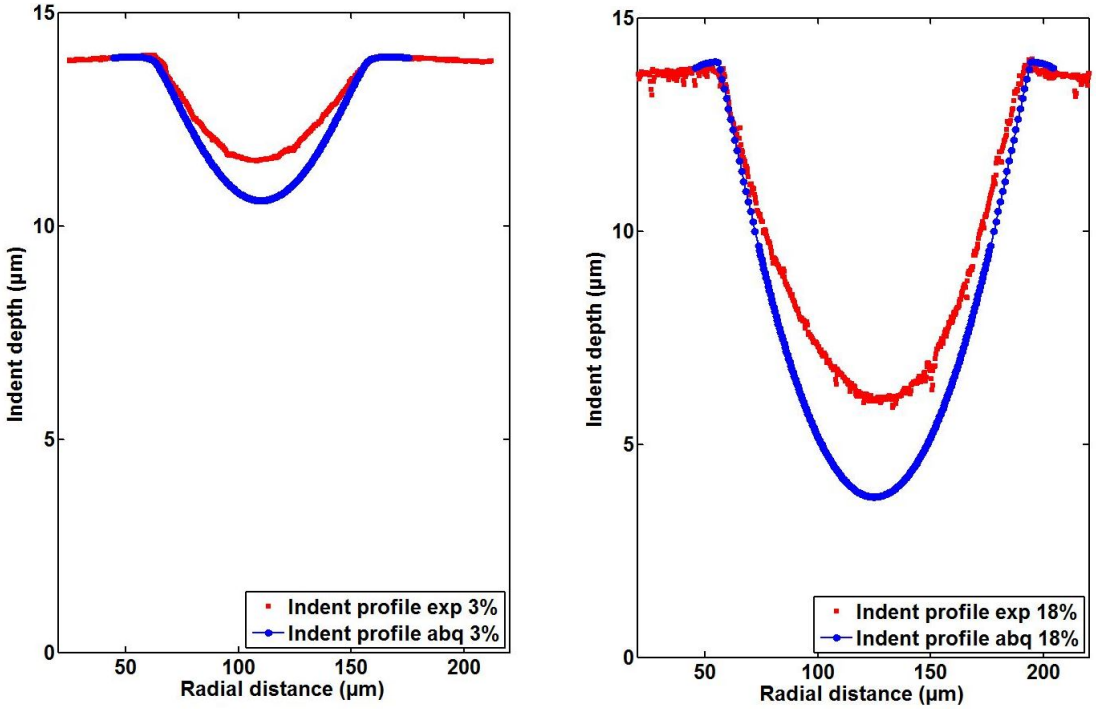

(a) 3 %

(b) 18 %

FIGURE 4.22: Experimental and simulated indent profiles on silicon nitride specimens with 3% (a) and 18% of pores (b) under peak load P=100 N with sphere of radius R = 0.2 mm

TABLE 4.6: Experimental depth versus numerical calculation under vertical load P= 100 N with sphere of radius R_1 = 0.2 mm

Porosity volume content	3 %	18 %
Experimental depth (µm)	2.48	8.2
Numerical depth (µm)	3.37	10.2

identification procedure already discussed.

The numerical simulations reproduce well the general geometric features (contact radius, pile-up...) of the surface indents. It is therefore clear that we can easily go back to the indentation stress-strain curve presented in the previous section. On the other side, it is observed that the maximum indentation depth is overestimated. To illustrate this crucial point, the experimental and numerical values of the residual depths for 3% and 18% of porosity are given in TAB.4.6. As discussed in case of dense silicon nitride materials, a part of the deviation can be attributed to experimental error but this is not the only explanation. Indeed, a large part of the overestimation of the indenter maximum penetration can be attributed to the fact that no crack initiation or propagation criterion was introduced in the simulations.

4.5 Conclusions

Silicon nitride materials with 3% and 18% of residual porosity were obtained when lower pressures were applied during the sintering process and their mechanical behaviour compared to the dense materials obtained in the previous chapter. The influence of porosity content on the elastic modulus and Vickers hardness were characterised thanks to empirical models widely used in the literature. It was found that the zero−porosity modulus E_0 values and other fitting parameters are in very good agreement with those reported in the literature for porous silicon nitride ceramics. The observed deviation from the expected theoretical values may be attributed to the heterogeneous grain geometry packaging and random pore morphology in the specimens.

The Hertzian contact damage mechanisms have been examined at the macroscopic and mesoscopic scales using diamond spheres of different sizes. Bonded interface and focused ion beam sectioning technique have been used to image the contact mechanisms. For the larger radius, it is found that increasing the porosity induced a transition from fracture at the surface to quasi-plastic damage mode, while for a reduced radius the damage consists only of subsurface microcracks initiated from the residual pores. The microcracks extend stably, interact with others and finally coalesce to form a macroscopic fissure leading to the catastrophic failure of the specimens.

Two hypotheses have been suggested to explain this size effect. The first one is the probability to find a critical flaw and the second one relates the contact size to stress field in presence of pores. Numerical simulations using semi-analytical code showed an increase of the maximum tensile stress with increasing the sphere radius. Finally, the true uniaxial stress-strain curves were obtained by means instrumented indentation and reverse identification. Critical stiffness loss was noticed while increasing the porosity volume content.

It is worth noting that subsurface damage mode is not easily detectable but can seriously reduces the lifetime of components. Therefore, it is essential to avoid the presence of pores or cluster of pores in the final product, and this by ensuring a proper control of the processing conditions.

General conclusions and prospects

Ceramic materials and more particularly technical ceramics present very interesting mechanical, thermal and electrical properties suitable in various industrial applications. Among these materials, silicon nitride is considered as an ideal candidate for the development of ball bearings for the automotive and aeronautic industries. The main objective of this thesis consists of in the investigation of the contact damage mechanisms of silicon nitride materials with different grain sizes (fine, medium and coarse) and porosity volume contents. This work aims also to identify the nonlinear parameters of the processed materials and study the effect of the density and other microstructural features.

The materials were processed by spark plasma sintering technique with addition of different amount of additive. Yttrium oxide was selected as additive. A gradual evolution from materials with fine equiaxed grains towards microstructures containing large elongated rodlike grains was observed with increasing the amount of sintering aid form 1% to 5%. In addition, a significant effect of the processing conditions (temperature, yttria amount) on the mechanical properties (elastic modulus, hardness, bending strength and toughness) was noticed. The contact damage is a crucial issue in case of brittle materials for bearings applications which can cause extra maintenance costs. The damage modes have therefore been extensively examined at different scales using standard methods such as bonded interface sectioning technique in addition to more sophisticated approaches like Focused Ion Beam milling and Transmission Electron Microscopy.

The Hertzian contact damages have been examined at macroscopic (large scale) and mesoscopic scales (small scale) by using diamond spheres of different radii on dense and porous materials. At the large scale, experimental observations revealed a remarkable size effect on the damage mode for coarse microstructure : fracture at large scale and quasi−plastic deformation at smaller scale. In addition, the transition radius for a coarse Si_3N_4 microstructure was experimentally obtained. The difference with values reported in the literature is attributed to the strong assumptions made in previous studies. For porous materials, it was found that increasing the porosity induced a transition from fracture at the surface to quasi-plastic damage mode at the macroscopic scale. For a reduced radius, the damage consists only of subsurface micro−cracks initiated from grains boundaries and residual pores. It is worth noting that this damage mode is not easily detectable but may deteriorate the lifetime of components. Therefore, it is essential to avoid the presence of pores or cluster of pores, and this by ensuring a proper control of the processing conditions.

The inverse analysis is a fundamental approach to fully characterize the mechanical behaviour of brittle materials. The technique was first applied to fully dense silicon nitride materials. A simple bilinear law was proposed as a first approach with the yield stress and hardening coefficient as unknown nonlinear parameters. They were obtained from the experimental load versus displacement curves from nanoindentation tests and minimization module based on the Levenberg-

Marquardt algorithm. The identified parameters were used to simulate the mechanical response of materials under a vertical or rolling loadings. It was numerically demonstrated that these latter conditions enlarge the damage zone independently of the material microstructure.

Although the results obtained with the proposed model (bilinear) are consistent, they are only a first approximation of the true mechanical behaviour of the processed materials. In fact, the bilinear law with two unknown parameters is also too simple to capture all the damage mechanisms observed experimentally. The weakness of the model has arisen at the comparison between experimental and numerical profile of indents. More advanced models can be proposed to take into account the microcracks events or incorporate a damage variable during the identification procedure. One can also think that Drucker-Prager model that takes into account the hydrostatic pressure can improve the numerical answer. Load versus displacement curves can also be obtained using indenter of larger radius. In fact, a new testing system has to be developed based on standard tensile machine where the displacement is measured using digital image correlation. The identification procedure will then be applied and results compared to those obtained by means of commercial nanoindentation machine. Another interesting perspective will be to investigate crack propagation and coalescence, also considering size effects.

Regarding the experimental side of the future work, one has to identify the exact physical characteristics of the dislocations (the burgers vectors and slip system) observed for coarse silicon nitride materials. Same work has to be done in case of materials with fine microstructure where plastic mode is dominant. It was also reported in previous studies dealing with contact damage that the sintering additive nature is of paramount importance on the material response. However, the state of the art has shown that only oxide additives were considered until now. Silicon nitride with non-oxide additive presents a very interesting alternative especially for high temperature applications. Finally, the porous materials can be tested under larger number of cycles to track changes in the short crack network.

Acknowledgements

This research was supported in part by a mobility grant from *Région Rhône-Alpes* in the framework of Avenir Lyon-Saint-Etienne program and JSPS Core-to-Core Program, A. Advanced Research Networks, international research core on smart layered materials and structures for energy saving.

Appendix

As presented in the second chapter, the observation of the damage under the contact sites was performed using Focused Ion Beam and Transmission Electron Microscopy. FIB is sufficient for porous specimens, however FIB + TEM are more suitable in case of dense specimens. In this annex, we want to give more details about the preparation of thin foil from the damaged area in fully dense silicon nitride materials. Prior to introducing the samples in the FIB, Hertzian contact tests were performed using diamond sphere of radius 0.2 mm. These experimental conditions are a good compromise between the accumulated damage and FIB instruments capacity. The surface indents were first observed under optical microscopy and the surface depression profiles obtained using a profilometer (VK100, Keyence). Sequentially scannng mode allows a 3D reconstruction of the surface depression as shown in the figure below.

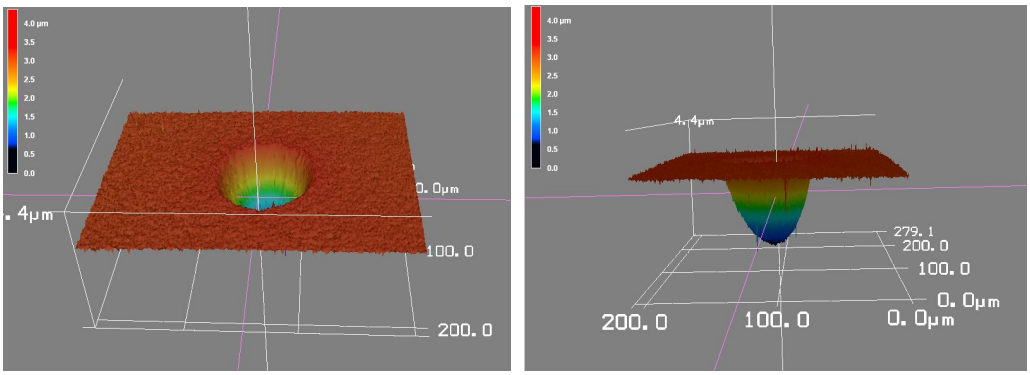

(a) (b)

FIGURE 4.23: 3D indent profile after indentation of silicon nitride specimen with sphere of radius 0.2 mm under peak load P = 45 N

After having measured the dimensions of the indent, the challenge consisted of investigating at the damage mechanisms under such small indents. This work was made more difficult by the fact that the silicon nitride is a very hard and not electrically conductive ceramic. The observations were made using Versa 3D DualBeam (FIB/SEM) system from FEI company. Before beginning with the steps shown on the next page, the surface of the indents was carbon coated to prevent etching.

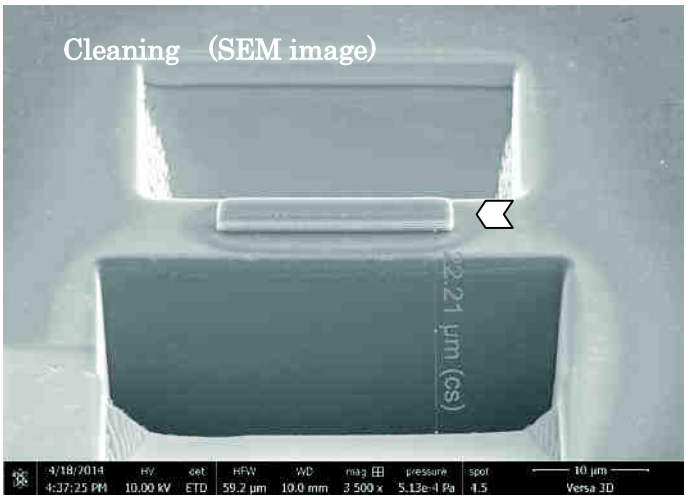

Cleaning remaining parts（SIM：30 kv, 15 nA）

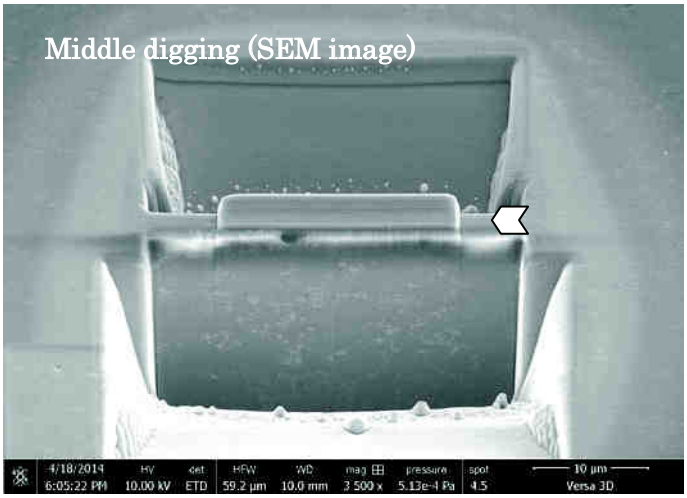

Middle digging（30 kv, 5 nA）

upside：Tilt 50 °

downside：Tilt 54 °

X：32 μm

Y：down 7 μm, up 5 μm

Z：5 μm

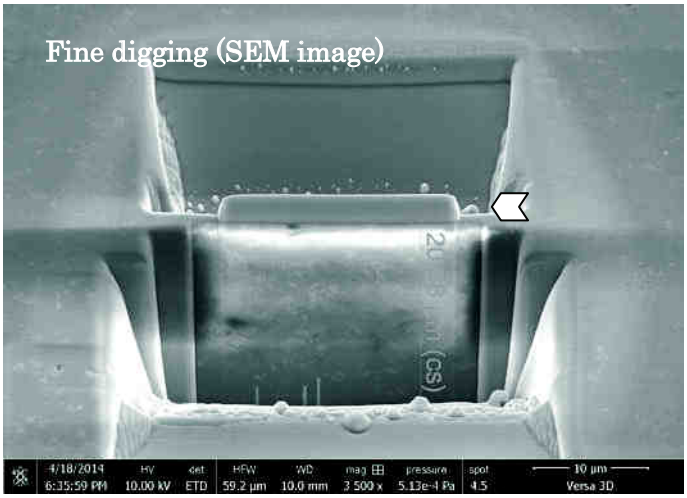

Fine digging（30 kv, 3 nA）

upside：Tilt 50 °

downside：Tilt 54 °

X：25 μm

Y：down 3.5 μm, up 2 μm

Z：5 μm

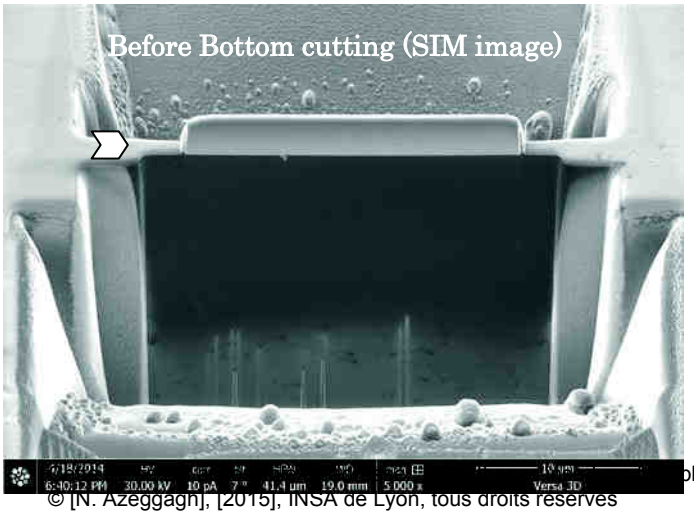

Tilt：7 °

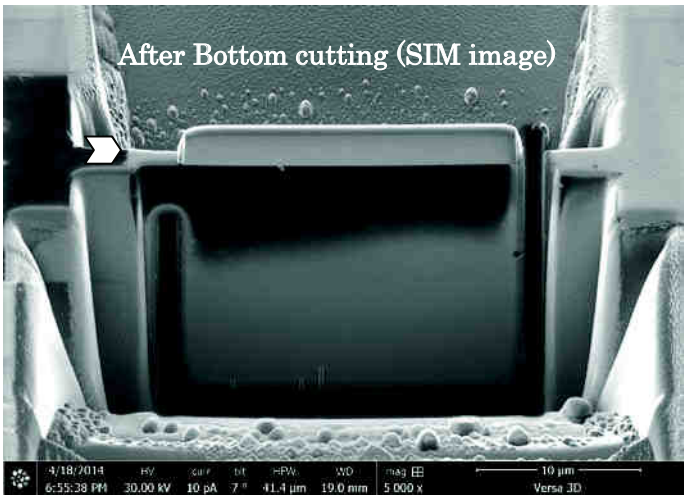

Bottom cutting（30 kv, 1 nA）

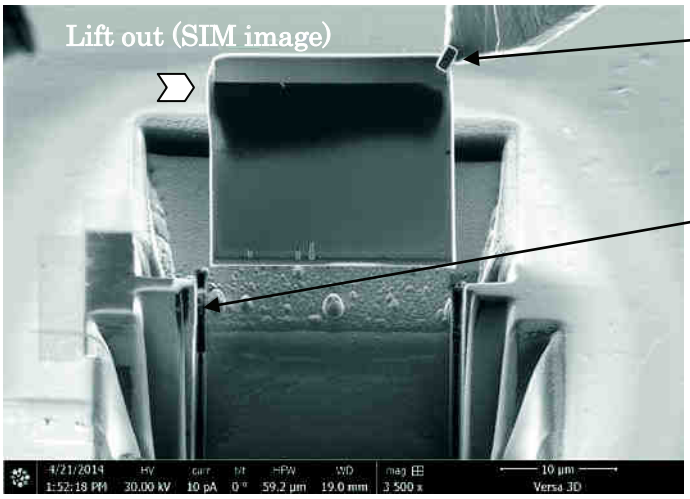

C dep —probe and specimen—
（30 kv, 0.1 nA）
Tilt：0°
↓
Cutting—left side of specimen—
（30 kv, 0.1 nA）
↓
Lift out

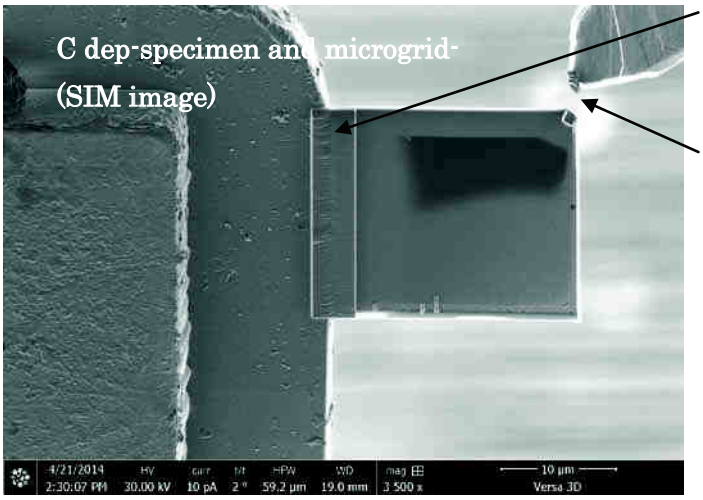

C dep —specimen and microgrid—
（30 kv, 0.1 nA）
↓
Cutting—probe and specimen—
（30 kv, 0.1 nA）

Rotate stage 180°, and conduct C dep in the back side.

Thinning

Tilt the specimen became vertically in SIM image. **Tilt：51.5°**

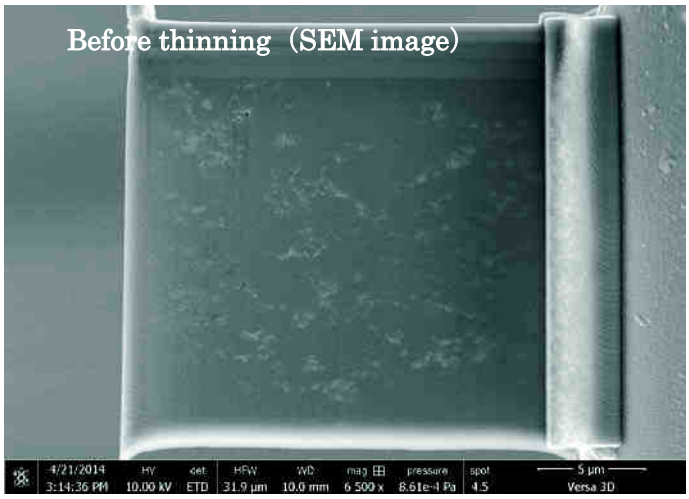

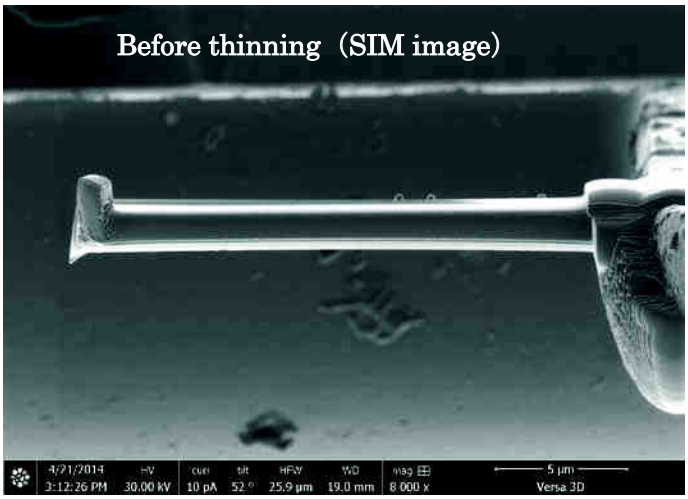

Coarse thinning（30 kv, 0.1 nA）

Incidence angle：±2°

Thinning was until 300 nm.

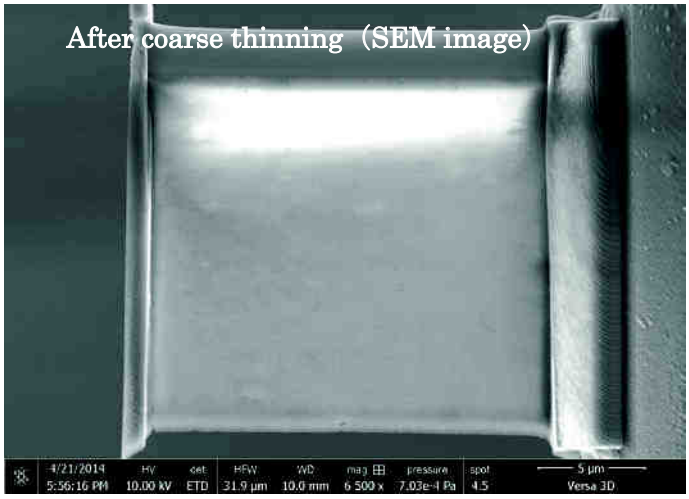

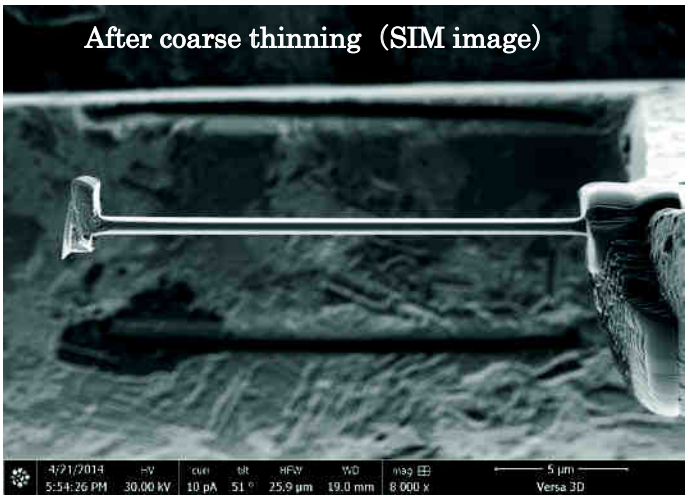

Fine thinning（8 kv, 25 pA）→（5 kv, 16 pA）

Incidence angle：±2°

Thinning was until about 100 nm.

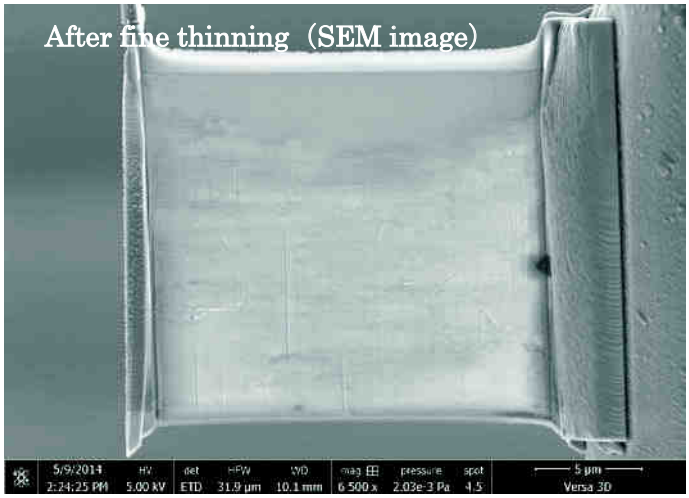

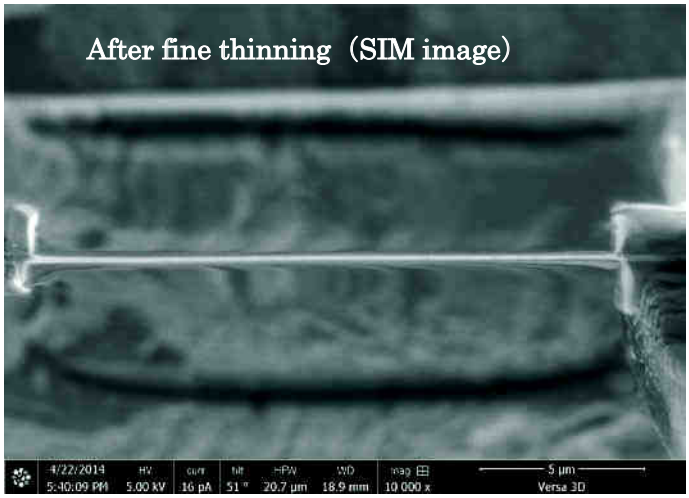

Biblography

[ACerS, 2014] ACerS (2014). http ://ceramics.org/learn-about-ceramics/history-of-ceramics.

[ASTM, 1981] ASTM (1981). *Annual book of ASTM standards*, chapter 17. American Society for Testing and Materials.

[Atkins and Tabor, 1965] Atkins, A. and Tabor, D. (1965). Plastic indentation in metals with cones. *Journal of the Mechanics and Physics of Solids*, 13(3) :149–164.

[Bal and Rahaman, 2012] Bal, B. and Rahaman, M. (2012). Orthopedic applications of silicon nitride ceramics. *Acta biomaterialia*, 8(8) :2889–2898.

[Belmonte et al., 2010] Belmonte, M., González-Julián, J., Miranzo, P., and Osendi, M. (2010). Spark plasma sintering : A powerful tool to develop new silicon nitride-based materials. *Journal of the European Ceramic Society*, 30(14) :2937–2946.

[Bonnefont et al., 2012] Bonnefont, G., Fantozzi, G., Trombert, S., and Bonneau, L. (2012). Fine-grained transparent mgal 2 o 4 spinel obtained by spark plasma sintering of commercially available nanopowders. *Ceramics International*, 38(1) :131–140.

[Bouville et al., 2014] Bouville, F., Maire, E., Meille, S., Van de Moortèle, B., Stevenson, A. J., and Deville, S. (2014). Strong, tough and stiff bioinspired ceramics from brittle constituents. *Nature materials*, 13(5) :508–514.

[Bowles and Witkin, 1979] Bowles, A. and Witkin, D. (1979). Hot isostatic pressing. In *High-Pressure Science and Technology*, pages 1718–1726. Springer.

[Bucaille et al., 2003] Bucaille, J.-L., Stauss, S., Felder, E., and Michler, J. (2003). Determination of plastic properties of metals by instrumented indentation using different sharp indenters. *Acta materialia*, 51(6) :1663–1678.

[Buckingham, 1914] Buckingham, E. (1914). On physically similar systems ; illustrations of the use of dimensional equations. *Physical Review*, 4(4) :345–376.

[Buljak and Maier, 2011] Buljak, V. and Maier, G. (2011). Proper orthogonal decomposition and radial basis functions in material characterization based on instrumented indentation. *Engineering Structures*, 33(2) :492–501.

[Calvié et al., 2014] Calvié, E., Réthoré, J., Joly-Pottuz, L., Meille, S., Chevalier, J., Garnier, V., Jorand, Y., Esnouf, C., Epicier, T., Quirk, J., et al. (2014). Mechanical behavior law of ceramic nanoparticles from transmission electron microscopy in situ nano-compression tests. *Materials Letters*, 119 :107–110.

[Cao and Lu, 2004] Cao, Y. P. and Lu, J. (2004). A new method to extract the plastic properties of metal materials from an instrumented spherical indentation loading curve. *Acta Materialia*, 52(13) :4023–4032.

[Ceramtec, 2015] Ceramtec (2015). https ://www.ceramtec.com/ceramic-materials/metal-matrix-composites/.

[Chaise and Nélias, 2011] Chaise, T. and Nélias, D. (2011). Contact pressure and residual strain in 3d elasto-plastic rolling contact for a circular or elliptical point contact. *Journal of Tribology*, 133(4) :041402.

[Chamberlain et al., 2006] Chamberlain, A. L., Fahrenholtz, W. G., and Hilmas, G. E. (2006). Pressureless sintering of zirconium diboride. *Journal of the American Ceramic Society*, 89(2) :450–456.

[Chen et al., 2007] Chen, X., Ogasawara, N., Zhao, M., and Chiba, N. (2007). On the uniqueness of measuring elastoplastic properties from indentation : the indistinguishable mystical materials. *Journal of the Mechanics and Physics of Solids*, 55(8) :1618–1660.

[Cheng and Cheng, 2004] Cheng, Y.-T. and Cheng, C.-M. (2004). Scaling, dimensional analysis, and indentation measurements. *Materials Science and Engineering : R : Reports*, 44(4) :91–149.

[Chevalier, 2006] Chevalier, J. (2006). What future for zirconia as a biomaterial ? *Biomaterials*, 27(4) :535–543.

[Chintapalli et al., 2012] Chintapalli, R., Jimenez-Pique, E., Marro, F., Yan, H., Reece, M., and Anglada, M. (2012). Spherical instrumented indentation of porous nanocrystalline zirconia. *Journal of the European Ceramic Society*, 32(1) :123–132.

[Chollacoop et al., 2003] Chollacoop, N., Dao, M., and Suresh, S. (2003). Depth-sensing instrumented indentation with dual sharp indenters. *Acta materialia*, 51(13) :3713–3729.

[Christman et al., 1989] Christman, T., Needleman, A., and Suresh, S. (1989). An experimental and numerical study of deformation in metal-ceramic composites. *Acta Metallurgica*, 37(11) :3029–3050.

[Clément et al., 2013] Clément, P., Meille, S., Chevalier, J., and Olagnon, C. (2013). Mechanical characterization of highly porous inorganic solids materials by instrumented micro-indentation. *Acta Materialia*, 61(18) :6649–6660.

[Constantinescu and Tardieu, 2001] Constantinescu, A. and Tardieu, N. (2001). On the identification of elastoviscoplastic constitutive laws from indentation tests. *Inverse Problems in Engineering*, 9(1) :19–44.

[Csanádi et al., 2015] Csanádi, T., Chinh, N. Q., Szommer, P., Dusza, J., Lenčés, Z., and Šajgalík, P. (2015). Deformation and fracture of beta-silicon nitride micropillars. *Journal of the American Ceramic Society*, 98(2) :374–377.

[Dao et al., 2001] Dao, M., Chollacoop, N., Van Vliet, K., Venkatesh, T., and Suresh, S. (2001). Computational modeling of the forward and reverse problems in instrumented sharp indentation. *Acta materialia*, 49(19) :3899–3918.

[De Aza et al., 2002] De Aza, A., Chevalier, J., Fantozzi, G., Schehl, M., and Torrecillas, R. (2002). Crack growth resistance of alumina, zirconia and zirconia toughened alumina ceramics for joint prostheses. *Biomaterials*, 23(3) :937–945.

[Dean and Lopez, 1983] Dean, E. and Lopez, J. (1983). Empirical dependence of elastic moduli on porosity for ceramic materials. *Journal of the American Ceramic Society*, 66(5) :366–370.

[Delalleau et al., 2008] Delalleau, A., Josse, G., Lagarde, J., Zahouani, H., and Bergheau, J. (2008). Characterization of the mechanical properties of skin by inverse analysis combined with an extensometry test. *Wear*, 264(5) :405–410.

[Delalleau et al., 2006] Delalleau, A., Josse, G., Lagarde, J.-M., Zahouani, H., and Bergheau, J.-M. (2006). Characterization of the mechanical properties of skin by inverse analysis combined with the indentation test. *Journal of biomechanics*, 39(9) :1603–1610.

[Diaz and Hampshire, 2004] Diaz, A. and Hampshire, S. (2004). Characterisation of porous silicon nitride materials produced with starch. *Journal of the European Ceramic Society*, 24(2) :413–419.

[Doerner and Nix, 1986] Doerner, M. F. and Nix, W. D. (1986). A method for interpreting the data from depth-sensing indentation instruments. *Journal of Materials Research*, 1(04) :601–609.

[Doerner and Nix, 1988] Doerner, M. F. and Nix, W. D. (1988). Stresses and deformation processes in thin films on substrates. *Critical Reviews in Solid State and Material Sciences*, 14(3) :225–268.

[Evans and Sharp, 1971] Evans, A. and Sharp, J. (1971). Microstructural studies on silicon nitride. *Journal of Materials Science*, 6(10) :1292–1302.

[Evans and Charles, 1976] Evans, A. G. and Charles, E. A. (1976). Fracture toughness determinations by indentation. *Journal of the American Ceramic society*, 59(7-8) :371–372.

[Fischer-Cripps and Lawn, 1996] Fischer-Cripps, A. C. and Lawn, B. R. (1996). Stress analysis of contact deformation in quasi-plastic ceramics. *Journal of the American Ceramic Society*, 79(10) :2609–2618.

[Fuchs et al., 2013] Fuchs, F., Soltamov, V., Väth, S., Baranov, P., Mokhov, E., Astakhov, G., and Dyakonov, V. (2013). Silicon carbide light-emitting diode as a prospective room temperature source for single photons. *Scientific reports*, 3.

[G.M Pharr, 1992] G.M Pharr, W. O. (1992). An impoved technique for determing hardness and elastic modulus using load and displacement sensing indentation experiments. *J. Mater.Res*, 7 :1564–1583.

[Goto and Thomas, 1995] Goto, Y. and Thomas, G. (1995). Microstructure of silicon nitride ceramics sintered with rare-earth oxides. *Acta Metallurgica et Materialia*, 43(3) :923–930.

[Gu et al., 2003] Gu, Y., Nakamura, T., Prchlik, L., Sampath, S., and Wallace, J. (2003). Micro-indentation and inverse analysis to characterize elastic–plastic graded materials. *Materials Science and Engineering : A*, 345(1) :223–233.

[Guiberteau et al., 1994] Guiberteau, F., Padture, N. P., and Lawn, B. R. (1994). Effect of grain size on hertzian contact damage in alumina. *Journal of the American Ceramic Society*, 77(7) :1825–1831.

[Guillon et al., 2014] Guillon, O., Gonzalez-Julian, J., Dargatz, B., Kessel, T., Schierning, G., Räthel, J., and Herrmann, M. (2014). Field-assisted sintering technology/spark plasma sintering : Mechanisms, materials, and technology developments. *Advanced Engineering Materials*, 16(7) :830–849.

[Hadfield, 1998] Hadfield, M. (1998). Failure of silicon nitride rolling elements with ring crack defects. *Ceramics international*, 24(5) :379–386.

[Hall, 1951] Hall, E. (1951). The deformation and ageing of mild steel : Iii discussion of results. *Proceedings of the Physical Society. Section B*, 64(9) :747.

[Hampshire, 2007] Hampshire, S. (2007). Silicon nitride ceramics–review of structure, processing and properties. *Journal of Achievements in Materials and Manufacturing Engineering*, 24(1) :43–50.

[Hampshire, 2009] Hampshire, S. (2009). Silicon nitride ceramics. In *Materials Science Forum*, volume 606, pages 27–41. Trans Tech Publ.

[Hay and Pharr, 2000] Hay, J. and Pharr, G. (2000). Instrumented indentation testing. *Materials Park, OH : ASM International, 2000.*, pages 232–243.

[Hertz, 1881] Hertz, H. (1881). On the contact of elastic solids. *J. reine angew. Math*, 92(156-171) :110.

[Heuer, 1987] Heuer, A. H. (1987). Transformation toughening in zro2-containing ceramics. *Journal of the American Ceramic Society*, 70(10) :689–698.

[Hirosaki et al., 1988] Hirosaki, N., Okada, A., and Matoba, K. (1988). Sintering of si3n4 with the addition of rare-earth oxides. *Journal of the American Ceramic Society*, 71(3) :C–144.

[Hu et al., 2008] Hu, N., Masuda, Z., Yamamoto, G., Fukunaga, H., Hashida, T., and Qiu, J. (2008). Effect of fabrication process on electrical properties of polymer/multi-wall carbon nanotube nanocomposites. *Composites Part A : Applied Science and Manufacturing*, 39(5) :893–903.

[Huber and Tsakmakis, 1999] Huber, N. and Tsakmakis, C. (1999). Determination of constitutive properties fromspherical indentation data using neural networks. part ii : plasticity with nonlinear isotropic and kinematichardening. *Journal of the Mechanics and Physics of Solids*, 47(7) :1589–1607.

[Hulbert et al., 2008] Hulbert, D. M., Anders, A., Dudina, D. V., Andersson, J., Jiang, D., Unuvar, C., Anselmi-Tamburini, U., Lavernia, E. J., and Mukherjee, A. K. (2008). The absence of plasma in Şspark plasma sinteringŤ. *Journal of Applied Physics*, 104(3) :033305.

[Humenik and Parikh, 1956] Humenik, M. and Parikh, N. M. (1956). Cermets : I, fundamental concepts related to micro-structure and physical properties of cermet systems. *Journal of the American Ceramic Society*, 39(2) :60–63.

[Hutchinson, 1989] Hutchinson, J. (1989). Mechanisms of toughening in ceramics. *Theoretical and applied mechanics*, pages 139–144.

[Inoue, 1966] Inoue, K. (1966). Apparatus for electrically sintering discrete bodies. US Patent 3,250,892.

[Issa et al., 2015] Issa, I., Amodeo, J., Réthoré, J., Joly-Pottuz, L., Esnouf, C., Morthomas, J., Perez, M., Chevalier, J., and Masenelli-Varlot, K. (2015). In situ investigation of mgo nanocube deformation at room temperature. *Acta Materialia*, 86 :295–304.

[Jacq et al., 2002] Jacq, C., Nelias, D., Lormand, G., and Girodin, D. (2002). Development of a three-dimensional semi-analytical elastic-plastic contact code. *Journal of tribology*, 124(4) :653–667.

[Johnson, 1987] Johnson, K. L. (1987). *Contact mechanics*. Cambridge university press.

[Kaczmar et al., 2000] Kaczmar, J., Pietrzak, K., and Włosiński, W. (2000). The production and application of metal matrix composite materials. *Journal of Materials Processing Technology*, 106(1) :58–67.

[Kang, 2004] Kang, S.-J. L. (2004). *Sintering : densification, grain growth and microstructure*. Butterworth-Heinemann.

[Kim et al., 1999] Kim, D., Jung, Y.-G., Peterson, I., and Lawn, B. (1999). Cyclic fatigue of intrinsically brittle ceramics in contact with spheres. *Acta materialia*, 47(18) :4711–4725.

[Kitayama et al., 2001] Kitayama, M., Hirao, K., Watari, K., Toriyama, M., and Kanzaki, S. (2001). Thermal conductivity of beta-si3n4 : Iii, effect of rare-earth (re= la, nd, gd, y, yb, and sc) oxide additives. *Journal of the American Ceramic Society*, 84(2) :353–58.

[Krstic and Krstic, 2012] Krstic, Z. and Krstic, V. D. (2012). Silicon nitride : the engineering material of the future. *Journal of Materials Science*, 47(2) :535–552.

[Latella et al., 1997] Latella, B. A., OConnor, B. H., Padture, N. P., and Lawn, B. R. (1997). Hertzian contact damage in porous alumina ceramics. *Journal of the American Ceramic Society*, 80(4) :1027–1031.

[Lawn et al., 1994] Lawn, B., Padture, N., Guiberteau, F., and Cai, H. (1994). A model for microcrack initiation and propagation beneath hertzian contacts in polycrystalline ceramics. *Acta metallurgica et materialia*, 42(5) :1683–1693.

[Lawn, 1998] Lawn, B. R. (1998). Indentation of ceramics with spheres : a century after hertz. *Journal of the American Ceramic Society*, 81(8) :1977–1994.

[Lawn et al., 1998] Lawn, B. R., Lee, S. K., Peterson, I. M., and Wuttiphan, S. (1998). Model of strength degradation from hertzian contact damage in tough ceramics. *Journal of the American Ceramic Society*, 81(6) :1509–1520.

[Lee et al., 2005] Lee, C. S., Lee, K. S., Lee, S. W., and Kim, D. K. (2005). Effect of grain boundary phase on contact damage resistance of silicon nitride ceramics. In *Key Engineering Materials*, volume 287, pages 421–426. Trans Tech Publ.

[Lee and Lawn, 1999] Lee, S. K. and Lawn, B. R. (1999). Contact fatigue in silicon nitride. *Journal of the American Ceramic Society*, 82(5) :1281–1288.

[Lee et al., 1997] Lee, S. K., Wuttiphan, S., and Lawn, B. R. (1997). Role of microstructure in hertzian contact damage in silicon nitride : I, mechanical characterization. *Journal of the American Ceramic Society*, 80(9) :2367–2381.

[Levenberg, 1944] Levenberg, K. (1944). A method for the solution of certain problems in least squares. *Quarterly of applied mathematics*, 2 :164–168.

[Luo and Stevens, 1999] Luo, J. and Stevens, R. (1999). Porosity-dependence of elastic moduli and hardness of 3y-tzp ceramics. *Ceramics International*, 25(3) :281–286.

[Luo et al., 2014] Luo, J., Zhao, Z., Shen, J., and Zhang, C. (2014). Elastic–plastic analysis of ultrafine-grained si< sub> 2</sub> n< sub> 2</sub> o–si< sub> 3</sub> n< sub> 4</sub> composites by nanoindentation and finite element simulation. *Ceramics International*, 40(5) :7073–7080.

[Maass et al., 2009] Maass, R., Van Petegem, S., Ma, D., Zimmermann, J., Grolimund, D., Roters, F., Van Swygenhoven, H., and Raabe, D. (2009). Smaller is stronger : The effect of strain hardening. *Acta Materialia*, 57(20) :5996–6005.

[Marquardt, 1963] Marquardt, D. W. (1963). An algorithm for least-squares estimation of nonlinear parameters. *Journal of the Society for Industrial & Applied Mathematics*, 11(2) :431–441.

[Mata and Alcala, 2003] Mata, M. and Alcala, J. (2003). Mechanical property evaluation through sharp indentations in elastoplastic and fully plastic contact regimes. *Journal of materials research*, 18(07) :1705–1709.

[Miyoshi, 1985] Miyoshi, T. (1985). A study on evaluation of kic for structural ceramics. *Transactions of the Japanese Society of Mechanical Engineering, Series A*, 51 :2489–2497.

[Mondalek et al., 2011] Mondalek, P., Silva, L., and Bellet, M. (2011). A numerical model for powder densification by sps technique. *Advanced Engineering Materials*, 13(7) :587–593.

[Nasa, 2000] Nasa (2000). http ://www.nasa.gov/centers/marshall/news/background/facts/ssme.html.

[Niihara, 1983] Niihara, K. (1983). A fracture mechanics analysis of indentation-induced palmqvist crack in ceramics. *Journal of materials science letters*, 2(5) :221–223.

[Östlund et al., 2011] Östlund, F., Howie, P. R., Ghisleni, R., Korte, S., Leifer, K., Clegg, W. J., and Michler, J. (2011). Ductile–brittle transition in micropillar compression of gaas at room temperature. *Philosophical Magazine*, 91(7-9) :1190–1199.

[Park et al., 1997] Park, H., Kim, H.-E., and Niihara, K. (1997). Microstructural evolution and mechanical properties of si3n4 with yb2o3 as a sintering additive. *Journal of the American Ceramic Society*, 80(3) :750–756.

[Phani and Niyogi, 1987a] Phani, K. and Niyogi, S. (1987a). Young's modulus of porous brittle solids. *Journal of materials science*, 22(1) :257–263.

[Phani and Niyogi, 1987b] Phani, K. K. and Niyogi, S. (1987b). Elastic modulus-porosity relationship for si3n4. *Journal of materials science letters*, 6(5) :511–515.

[Quinn and Bradt, 2007] Quinn, G. D. and Bradt, R. C. (2007). On the vickers indentation fracture toughness test. *Journal of the American Ceramic Society*, 90(3) :673–680.

[Rhee et al., 2001] Rhee, Y.-W., Kim, H.-W., Deng, Y., and Lawn, B. R. (2001). Brittle fracture versus quasi plasticity in ceramics : a simple predictive index. *Journal of the American Ceramic Society*, 84(3) :561–565.

[Rice, 1998] Rice, R. W. (1998). *Porosity of Ceramics : Properties and Applications*. CRC Press.

[Richard, 1999] Richard, F. (1999). *Identification du comportement et évaluation de la fiabilité des composites stratifiés*. PhD thesis, Thèse de doctorat, Université de Franche Comté.

[Riedel and Chen, 2011] Riedel, R. and Chen, I.-W. (2011). *Ceramics Science and Technology, Materials and Properties*, volume 2. John Wiley & Sons.

[Riley, 2000] Riley, F. L. (2000). Silicon nitride and related materials. *Journal of the American Ceramic Society*, 83(2) :245–265.

[Rouxel et al., 2008] Rouxel, T., Ji, H., Hammouda, T., and Moréac, A. (2008). PoissonŠs ratio and the densification of glass under high pressure. *Physical review letters*, 100(22) :225501.

[Sammis and Ashby, 1986] Sammis, C. and Ashby, M. (1986). The failure of brittle porous solids under compressive stress states. *Acta Metallurgica*, 34(3) :511–526.

[Satet and Hoffmann, 2005] Satet, R. L. and Hoffmann, M. J. (2005). Influence of the rare-earth element on the mechanical properties of re–mg-bearing silicon nitride. *Journal of the American Ceramic Society*, 88(9) :2485–2490.

[Schlesinger and Paunovic, 2011] Schlesinger, M. and Paunovic, M. (2011). *Modern electroplating*, volume 55. John Wiley & Sons.

[She et al., 2003] She, J., Yang, J.-F., Beppu, Y., and Ohji, T. (2003). Hertzian contact damage in a highly porous silicon nitride ceramic. *Journal of the European Ceramic Society*, 23(8) :1193–1197.

[Simulia, 2011] Simulia, D. (2011). Abaqus 6.11 analysis user's manual. *Abaqus 6.11 Documentation*, pages 22–2.

[Somiya, 2013] Somiya, S. (2013). *Handbook of Advanced Ceramics : Materials, Applications, Processing, and Properties*. Academic Press.

[Spriggs, 1961] Spriggs, R. (1961). Expression for effect of porosity on elastic modulus of polycrystalline refractory materials, particularly aluminum oxide. *Journal of the American Ceramic Society*, 44(12) :628–629.

[Steinbrech, 1992] Steinbrech, R. (1992). Toughening mechanisms for ceramic materials. *Journal of the European Ceramic Society*, 10(3) :131–142.

[Strecker et al., 2005] Strecker, K., Ribeiro, S., and Hoffmann, M.-J. (2005). Fracture toughness measurements of lps-sic : a comparison of the indentation technique and the sevnb method. *Materials Research*, 8(2) :121–124.

[Suarez et al., 2013] Suarez, M., Fernandez, A., Kessel, H., Hennicke, J., Menendez, J., Kirchner, R., Torrecillas, R., and Kessel, T. (2013). *Challenges and opportunities for spark plasma sintering : a key technology for a new generation of materials*. INTECH Open Access Publisher.

[Swain and Hagan, 1976] Swain, M. and Hagan, J. (1976). Indentation plasticity and the ensuing fracture of glass. *Journal of Physics D : Applied Physics*, 9(15) :2201.

[Tabor, 1951] Tabor, D. (1951). *The hardness of metals*, volume 10. ClarendonP.

[Tabor, 1996] Tabor, D. (1996). Indentation hardness : fifty years on a personal view. *Philosophical Magazine A*, 74(5) :1207–1212.

[Taylor, 1933] Taylor, G. (1933). Apparatus for making hard metal compositions. US Patent 1,896,854.

[Terwilliger and Lange, 1975] Terwilliger, G. and Lange, F. (1975). Pressureless sintering of si3n4. *Journal of Materials Science*, 10(7) :1169–1174.

[Tiwari et al., 2009] Tiwari, D., Basu, B., and Biswas, K. (2009). Simulation of thermal and electric field evolution during spark plasma sintering. *Ceramics International*, 35(2) :699–708.

[Trunec, 2008] Trunec, M. (2008). Effect of grain size on mechanical properties of 3y-tzp ceramics. *Ceram. Silik*, 52(3) :165–171.

[Tsuge et al., 1975] Tsuge, A., Nishida, K., and Komatsu, M. (1975). Effect of crystallizing the grain-boundary glass phase on the high-temperature strength of hot-pressed si3n4 containing y2o3. *Journal of the American Ceramic Society*, 58(7-8) :323–326.

[Tunvisut et al., 2002] Tunvisut, K., Busso, E., O'dowd, N., and Brantner, H. (2002). Determination of the mechanical properties of metallic thin films and substrates from indentation tests. *Philosophical Magazine A*, 82(10) :2013–2029.

[Tyulyukovskiy and Huber, 2006] Tyulyukovskiy, E. and Huber, N. (2006). Identification of viscoplastic material parameters from spherical indentation data : Part i. neural networks. *Journal of materials research*, 21(03) :664–676.

[Uchic et al., 2007] Uchic, M. D., Holzer, L., Inkson, B. J., Principe, E. L., and Munroe, P. (2007). Three-dimensional microstructural characterization using focused ion beam tomography. *MRS bulletin*, 32(05) :408–416.

[Vandiver et al., 1989] Vandiver, P. B., Soffer, O., Klima, B., and Svoboda, J. (1989). The origins of ceramic technology at dolní věstonice, czechoslovakia. *Science*, 246(4933) :1002–1008.

[Vanmeensel et al., 2005] Vanmeensel, K., Laptev, A., Hennicke, J., Vleugels, J., and Van der Biest, O. (2005). Modelling of the temperature distribution during field assisted sintering. *Acta Materialia*, 53(16) :4379–4388.

[Wang et al., 2015] Wang, W., Yamamoto, G., Shirasu, K., Nozaka, Y., and Hashida, T. (2015). Effects of processing conditions on microstructure, electrical conductivity and mechanical properties of mwcnt/alumina composites prepared by flocculation. *Journal of the European Ceramic Society*.

[Wang et al., 2014] Wang, Z.-H., Bai, B., and Ning, X.-S. (2014). Effect of rare earth additives on properties of silicon nitride ceramics. *Advances in Applied Ceramics*, 113(3) :173–177.

[Warren, 1978] Warren, R. (1978). Measurement of the fracture properties of brittle solids by hertzian indentation. *Acta Metallurgica*, 26(11) :1759–1769.

[Watari et al., 2004] Watari, F., Yokoyama, A., Omori, M., Hirai, T., Kondo, H., Uo, M., and Kawasaki, T. (2004). Biocompatibility of materials and development to functionally graded implant for bio-medical application. *Composites Science and Technology*, 64(6) :893–908.

[Willander et al., 2006] Willander, M., Friesel, M., Wahab, Q.-u., and Straumal, B. (2006). Silicon carbide and diamond for high temperature device applications. *Journal of Materials Science : Materials in Electronics*, 17(1) :1–25.

[Wu et al., 2006] Wu, C.-H., Zorman, C., Mehregany, M., et al. (2006). Fabrication and testing of bulk micromachined silicon carbide piezoresistive pressure sensors for high temperature applications. *Sensors Journal, IEEE*, 6(2) :316–324.

[Xu et al., 1995] Xu, H. H., Wei, L., Padture, N. P., Lawn, B., and Yeckley, R. (1995). Effect of microstructural coarsening on hertzian contact damage in silicon nitride. *Journal of materials science*, 30(4) :869–878.

[Yamamoto et al., 2008] Yamamoto, G., Omori, M., Hashida, T., and Kimura, H. (2008). A novel structure for carbon nanotube reinforced alumina composites with improved mechanical properties. *Nanotechnology*, 19(31) :315708.

[Yang et al., 2003] Yang, J.-F., Deng, Z.-Y., and Ohji, T. (2003). Fabrication and characterisation of porous silicon nitride ceramics using yb2o3 as sintering additive. *Journal of the European Ceramic Society*, 23(2) :371–378.

[Yeheskel and Gefen, 1985] Yeheskel, O. and Gefen, Y. (1985). The effect of the alpha phase on the elastic properties of si 3 n 4. *Materials science and engineering*, 71 :95–99.

[Zaefferer et al., 2008] Zaefferer, S., Wright, S., and Raabe, D. (2008). Three-dimensional orientation microscopy in a focused ion beam–scanning electron microscope : A new dimension of microstructure characterization. *Metallurgical and Materials Transactions A*, 39(2) :374–389.

[Zerr et al., 1999] Zerr, A., Miehe, G., Serghiou, G., Schwarz, M., Kroke, E., Riedel, R., Fueß, H., Kroll, P., and Boehler, R. (1999). Synthesis of cubic silicon nitride. *Nature*, 400(6742) :340–342.

FOLIO ADMINISTRATIF

THÈSE SOUTENUE DEVANT L'INSTITUT NATIONAL DES SCIENCES APPLIQUÉES DE LYON

NOM : AZEGGAGH DATE de SOUTENANCE : 10 Septembre 2015

Prénom : Nacer

TITRE : Mécanismes d'endommagement des nitrures de silicium sous un chargement de contact

NATURE : Doctorat Numéro d'ordre : 2006-ISAL-0075

École doctorale : MATÉRIAUX DE LYON

Spécialité : Matériaux

Cote B.I.U. - Lyon : T 50/210/19 / et bis CLASSE :

RÉSUMÉ :

Ces travaux de thèse portent sur la détermination des propriétés mécaniques à différentes échelles ainsi que les mécanismes d'endommagement sous un chargement de contact des nitrures de silicium denses ou avec une porosités résiduelle. Ces céramiques techniques présentent des propriétés mécaniques fortement intéressantes : une faible densité, une dureté élevée, une bonne résistance à la corrosion et un faible coefficient de dilatation thermique. Elles sont notamment utilisés dans la fabrication des billes de roulement pour des applications dans les industries automobiles et aéronautiques. La caractérisation du comportement local sous un chargement de contact est donc un enjeu majeur pour garantir le bon fonctionnement des roulements.

Les matériaux étudiés ont été obtenus par frittage flash d'une poudre de Nitrure de Silicium avec différents pourcentages d'oxide d'yttrium comme additif. Le contrôle de la température et de la pression de frittage a permis d'obtenir des matériaux denses avec différentes tailles de grain mais aussi avec une porosité résiduelle variable. La première partie de ce travail consistait à caractériser l'influence des conditions d'élaboration (température, pression, pourcentage d'additif) sur la microstructure (taille des grains, compositions ...) et les propriétés mécaniques à l'échelle macroscopique (paramètres élastiques, dureté Vickers, résistance à la flexion ...) des matériaux frittés.

Des essais de contact de Hertz ont été ensuite réalisés afin identifier les mécanismes d'endommagement surfaciques ainsi que sous les indents. L'utilisation de sphères de différents rayons a mis en évidence un important effet d'échelle : des fissures circonférentielles à échelle macroscopique et des déformations plastique localisées à l'échelle mesoscopique avec des micro fissures distribuées aléatoirement. Les tests de nanoindentation permettent de solliciter localement les échantillons pour obtenir les propriétés élastiques des courbes force-déplacement. Des méthodes d'identification inverses permettent aussi d'extraire les paramètres plastiques. Le comportement non linéaire des céramiques a été modélisé en utilisant une loi bilinéaire où σ_y est la limite d'élasticité et K un paramètre d'écrouissage. Afin d'identifier ces deux paramètres, un modèle éléments finis axisymétrique avec une pointe sphérique déformable a été construit sous Abaqus. Le modèle a été couplé à un module d'identification inverse basé sur l'algorithme de Levemberg-Marquart pour minimiser l'écart (au sens des moindres carrés) entre les courbes expérimentales et numériques. Les simulations avec le code Isaac développé au sein du laboratoire LaMCoS ont permis de suivre d'évolution de la zone plastique lors d'un chargement de roulement.

MOTS-CLÉS : Microstructure, porosité, contact, identification inverse

Laboratoire(s) de recherche :
Laboratoire de Mécanique des Contacts et des Solides — UMR CNRS 5514 - INSA de Lyon
MATEriaux : Ingénierie et Sciences — UMR CNRS 5510 - INSA de Lyon
20, avenue Albert Einstein
69621 Villeurbanne Cedex FRANCE

Directeur de thèse : Professeur Jérôme Chevalier

Président du jury : Professeur Koshi Adachi

Composition du jury : Prof Koshi Adachi, Prof Jérôme Chevalier, Prof. Toshiyuki Hashida, Dr. Lucile Joly-Pottuz, Prof. Tanguy Rouxel, Prof. Tatsuya Kawada, Prof. Daniel Nélias, Mr. Bruno Druez